

This gives the number of modes around one k -value. The $D(\omega)$ around this k -value can then be given as

$$D(\omega) = \frac{V}{2\pi^2} \cdot k^2 \left(\frac{dk}{d\omega} \right) \quad (14.71)$$

since it is a measure of the number of modes per frequency interval.

It can be shown that for a single polarization the dispersion relation for a cubic lattice in the limit of low frequencies is similar to (14.66). Deriving the values of k^2 and $dk/d\omega$ from (14.66) and substituting them in (14.71), we obtain

$$D(\omega) = \frac{V}{4\pi^2} \left(\frac{\hbar}{2J_{\text{ex}} Sa^2} \right)^{3/2} \omega^{1/2} \quad (14.72)$$

At very low temperatures the limits of the integration may be placed at 0 and ∞ because as $\omega \rightarrow \infty$, $\langle n(\omega) \rangle \rightarrow 0$ exponentially.

We rewrite (14.69) to express the total number of magnons as

$$\begin{aligned} \sum_k n_k &= \frac{V}{4\pi^2} \left(\frac{k_B T}{2J_{\text{ex}} Sa^2} \right)^{3/2} \int_0^\infty \frac{x^{1/2}}{\exp(x) - 1} \quad \text{with } x = \frac{\hbar\omega}{k_B T} \\ &= (0.0587) \frac{V}{a^3} \left(\frac{k_B T}{2J_{\text{ex}} S} \right)^{3/2} \end{aligned} \quad (14.73)$$

For a cubic crystal with N magnetic ions per unit cell, the contribution of a single spin to the saturation magnetization $M(0)$ is

$$\frac{M(0)}{(N/a^3) S} = \frac{M(0) a^3}{NS} \quad (14.74)$$

Since the total spin is reduced from its saturation value NS by one unit per magnon, the change in magnetization is given by

$$\Delta M = \frac{\sum n_k}{V} \times \frac{M(0) a^3}{NS} = \frac{0.0587}{NS} \left(\frac{k_B T}{2J_{\text{ex}} S} \right)^{3/2} \cdot M(0) \quad (14.75)$$

Therefore, the fractional change of magnetization is written as

$$\frac{\Delta M}{M(0)} = \frac{0.0587}{NS} \left(\frac{k_B T}{2J_{\text{ex}} S} \right)^{3/2} \quad (14.76)$$

The above relation is famous as the Bloch $T^{3/2}$ law and has been verified by experiments. The heat capacity contributed by thermal excitation of magnons at low temperatures also varies as $T^{3/2}$.

14.7.3 Magnons in Antiferromagnets

Consider a one-dimensional antiferromagnet in which the spins with even indices $2n$ are on sublattice A with $S_{2n}^z = S$ and the spins with odd indices $(2n + 1)$ are on sublattice B with $S_{2n+1}^z = -S$. As for one-dimensional ferromagnets, we use

$$\begin{aligned}\mathbf{S}_{2n} &= \mathbf{S} + \boldsymbol{\sigma}_{2n} \\ \mathbf{S}_{2n+1} &= -\mathbf{S} + \boldsymbol{\sigma}_{2n+1}\end{aligned}\quad (14.77)$$

to linearize the equations of motion for \mathbf{S}_{2n} and \mathbf{S}_{2n+1} . The small spin vectors $\boldsymbol{\sigma}_{2n}$ and $\boldsymbol{\sigma}_{2n+1}$ lie in the xy -plane. Following the treatment of Section 14.7.1, the equations of motion for spins in the two sublattices are written as

$$\frac{d\sigma_{2n}^+}{dt} = \left(\frac{2iJ_{\text{ex}}S}{\hbar} \right) (2\sigma_{2n}^+ + \sigma_{2n+1}^+ + \sigma_{2n-1}^+) \quad (14.78)$$

$$\frac{d\sigma_{2n+1}^+}{dt} = - \left(\frac{2iJ_{\text{ex}}S}{\hbar} \right) (2\sigma_{2n+1}^+ + \sigma_{2n}^+ + \sigma_{2n+2}^+) \quad (14.79)$$

with $\sigma^+ = \sigma_x + i\sigma_y$.

Taking travelling wave solutions

$$\sigma_{2n}^+ = A \exp i[2nka - \omega t]; \quad \sigma_{2n+1}^+ = B \exp i[(2n+1)ka - \omega t] \quad (14.80)$$

and substituting them in (14.78) and (14.79), we get

$$\omega A = - \left(\frac{2J_{\text{ex}}S}{\hbar} \right) \{2A + B[\exp(ika) + \exp(-ika)]\} \quad (14.81a)$$

$$-\omega B = - \left(\frac{2J_{\text{ex}}S}{\hbar} \right) \{2B + A[\exp(ika) + \exp(-ika)]\} \quad (14.81b)$$

These equations have a solution, if

$$\begin{vmatrix} \left(-\frac{4J_{\text{ex}}S}{\hbar} \right) - \omega & \left(-\frac{4J_{\text{ex}}S}{\hbar} \right) \cos ka \\ \left(-\frac{4J_{\text{ex}}S}{\hbar} \right) \cos ka & \left(-\frac{4J_{\text{ex}}S}{\hbar} \right) + \omega \end{vmatrix} = 0 \quad (14.82)$$

which gives

$$\omega^2 = \left(\frac{4J_{\text{ex}}S}{\hbar} \right)^2 (1 - \cos^2 ka)$$

or

$$\omega = \frac{4J_{\text{ex}}S}{\hbar} \sin ka \quad (14.83)$$

In the long wavelength limit, (14.83) reduces to

$$\omega \approx \frac{4J_{\text{ex}}S}{\hbar} |ka| \quad (14.84)$$

since $|ka| \ll 1$ in this limit.

This is the dispersion relation for magnons in an antiferromagnet. The relation is different from that for a ferromagnet. For an antiferromagnet, ω is proportional to k and not to k^2 in the limit of low frequencies as given by (14.66) for a ferromagnet. The magnon dispersion is measured by inelastic neutron scattering experiments. The experimental magnon dispersion of RbMnF_3 crystal is traced in Fig. 14.22, showing a fairly large linear portion in the low frequency limit. The thermal excitation of magnons at low temperatures contributes a term in T^3 to the heat capacity. This term is in addition to the Debye T^3 term for phonons.

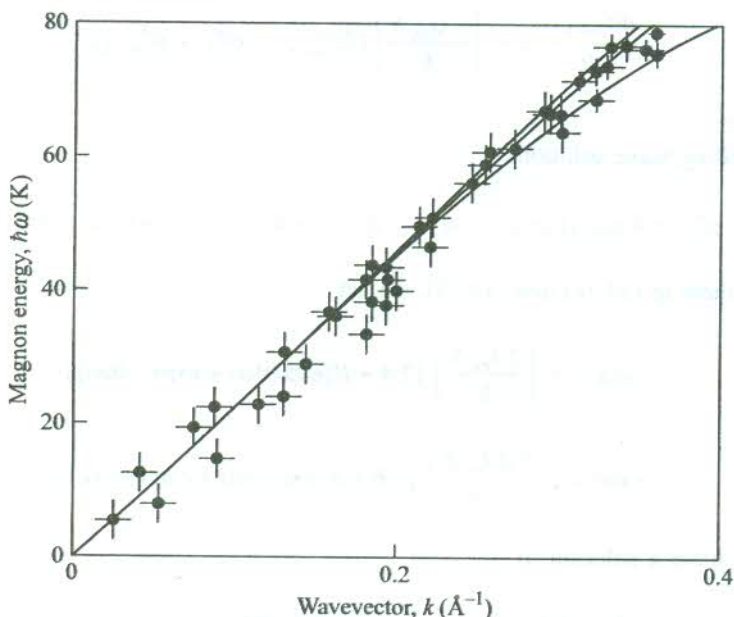


FIG. 14.22 Spectrum of magnon energy versus wavevector in the antiferromagnet RbMnF_3 as measured with an inelastic neutron scattering experiment at 4.2 K. [After C.G. Windsor and R.W.H. Stevenson, *Proc. Phys. Soc. (London)* **87**, 501 (1966).]

14.8 DETERMINATION OF MAGNETICALLY ORDERED STRUCTURES

Crystal structures are more often determined by the x-ray diffraction method. But the use of a slow neutron[†] (low energy) beam has certain distinct advantages, especially while dealing with the

[†] By virtue of being slow, the magnetic moment of a neutron gets sufficient time for interacting with the atomic moments of the system and thus gets scattered with the maximum possible information in its scattering cross-section.

magnetically ordered materials. The diffracted x-ray photons provide details about the spatial distribution of electronic charge, but carry no information about the atomic magnetic moment vectors in a magnetically ordered structure. On the other hand, a beam of slow neutrons serves as an excellent probe of local moments since the neutron itself has a magnetic moment which couples to the spin of elementary moments in a magnetic crystal. As a result of this coupling there appear peaks in the diffraction pattern in addition to those belonging to the non-magnetic Bragg reflection of neutrons by the atomic nuclei.

The additional lines get weaker in intensity as the temperature rises to the critical temperature at which the magnetic ordering vanishes and the lines disappear. These features easily distinguish them from other lines.

The gains of using a neutron beam are best appreciated in antiferromagnetic solids. The antiparallel ordering of moments within each domain results in zero macroscopic magnetic field which usually reveals the magnetic ordering in solids with a spontaneous magnetization. Therefore, a more subtle method is required to probe the ordering in such materials. As an example, we show the neutron diffraction pattern of MnO below and above the Néel temperature (120 K) in Fig. 14.23. Several lines in the pattern recorded at 80 K are not observed at 293 K, simply because the corresponding Bragg reflections originate from the magnetic ordering which exists no more above 120 K. Nuclear magnetic resonance offers another way to investigate the microscopic spin structure. For determining the size of a unit cell of a crystal having magnetic ordering it becomes imperative to take into consideration not only the equivalence of the sites but also the equivalence of the magnetic moment vectors located

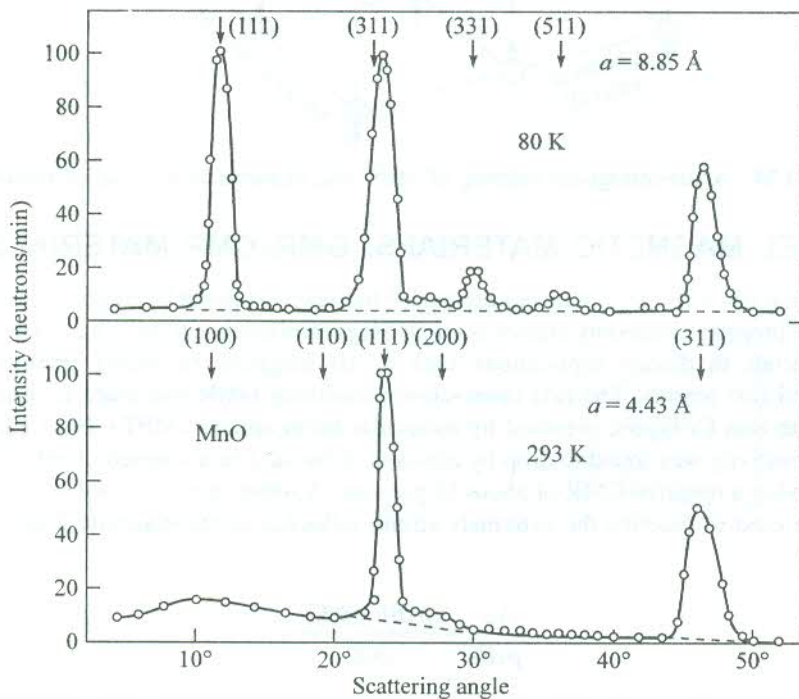


FIG. 14.23 Neutron diffraction patterns for an antiferromagnetic solid (MnO) below and above the Néel temperature (120 K). Reflection indices in the ordered and the disordered phases relate to the unit cells of different lattice constants 8.85 \AA and 4.43 \AA , respectively. The lines attributed to the ordering of spin moments are missing from the pattern recorded at 293 K since no ordered structure exists at this temperature. [After C.G. Shull, W.A. Strauser, and E.O. Wollan, *Phys. Rev.*, **83**, 333 (1951).]

at those sites. The size of a unit cell for an antiferromagnetic crystal as obtained by the x-ray diffraction is just half the size given by the neutron diffraction. The unit cells determined by the two techniques are referred to as *chemical unit cell* and *magnetic unit cell*, respectively. This point is clarified in Fig. 14.24 with the help of the ordering of moments of Mn^{2+} ions in the unit cell of $RbMnF_3$ ($T_N = 54.5$ K).

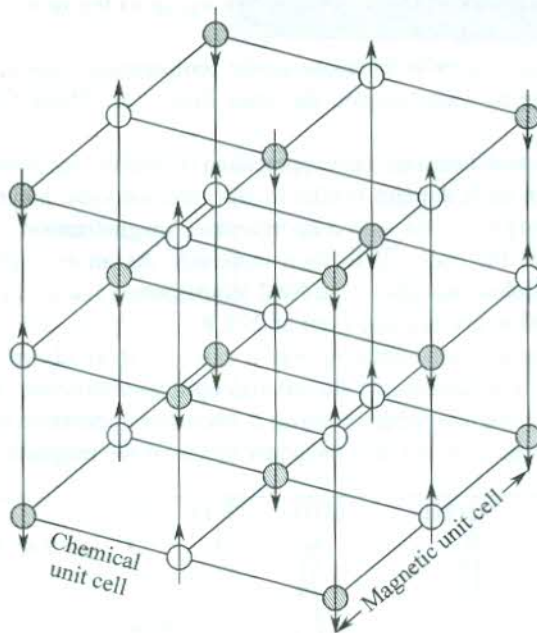


FIG. 14.24 Antiferromagnetic ordering of Mn^{2+} spin moments in a crystal of $RbMnF_3$.

14.9 NOVEL MAGNETIC MATERIALS: GMR–CMR MATERIALS

Recently, an extraordinarily large magnetoresistance* has been exhibited by some magnetic materials. This spectacular property commonly known as *Giant Magnetoresistance* (GMR) has found applications for these materials in device applications such as (i) magnetic recording (memory storage), (ii) actuators and (iii) sensors. The first observation concerning GMR was made in respect of Fe/Cr multilayers[†] with thin Cr layers, prepared by molecular beam epitaxy (MBE). For Cr layers of 9 Å thickness the resistivity was found to drop by almost a factor of 2 in a magnetic field of 2 T at 4.2 K (Fig. 14.25), giving a negative GMR of about 50 per cent. Another term *Colossal Magnetoresistance* (CMR) is often used to describe the extremely strong influence of the magnetic field. The CMR is defined as

$$\frac{\Delta \rho}{\rho(B)} = \frac{\rho(B) - \rho(0)}{\rho(B)} \quad (14.85)$$

The GMR–CMR effect is observed generally at low temperatures in the presence of large

* For definition refer to relation (9.65).

† M.N. Baibich, et al., *Phys. Rev. Lett.*, **61**, 2472 (1988).

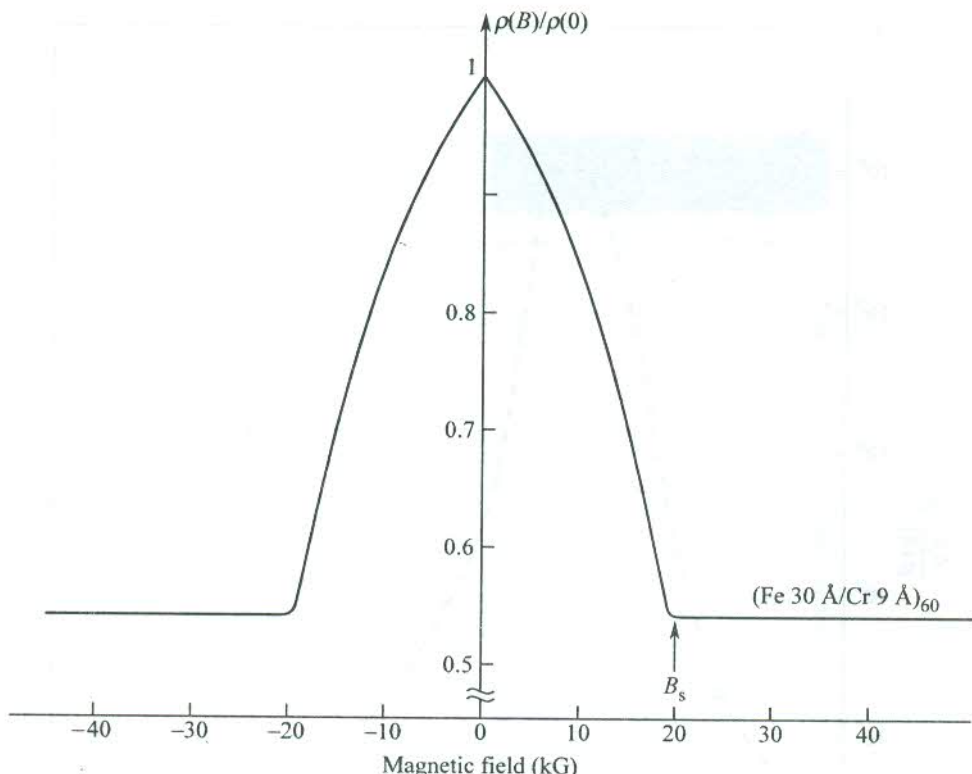


FIG. 14.25 Variation of resistivity of multilayers [(001) Fe 30 Å/(001) Cr 9 Å]₆₀ as a function of the magnetic field at 4.2 K. The specimen is a superlattice of 60 bilayers in which the current flows along the [110] direction and the magnetic field is applied in the layer plane (001) along the current direction. At the magnetic field B_s (in the saturated state; $B_s = 2$ T) the resistivity drops to almost half its zero-field value. [After M.N. Beibich et al., *Phys. Rev. Lett.*, **61**, 2472 (1988).]

magnetic fields (\sim a few tesla). But we require to exploit this property ideally near room temperature and at low fields for enhancing the technological viability of GMR–CMR materials. Hence, ever since the discovery of GMR and CMR a relentless activity has been on to develop such materials. Recently, a promising class of magnetic materials with composition $R_{1-x}A_x\text{MnO}_3$ ($R = \text{La, Nd, Gd, Y}$; $A = \text{Ca, Sr, Ba, Pb}$) has been identified. These manganites having perovskite structure have the unique distinction of being paramagnetic and semiconducting at high temperatures. They make a transition to the ferromagnetic and metallic state at low temperatures. This is unusual of metal–insulator systems because they are generally metallic at high temperatures. In the metallic state the resistivity is unexpectedly high.

The spin-off during search for ideal GMR–CMR materials occurred with the work of McCormack et al.* In epitaxially grown thin films of La–Ca–Mn–O, MR is found to depend strongly on film thickness and temperature. The CMR reaches its maximum (in excess of 10⁶ per cent) at 110 K with the magnetic field at 6 T (Fig. 14.26). The peak occurs just below the Curie temperature. For films thicker than ~ 2000 Å, the MR is reduced by orders of magnitude. The presence of grain boundaries

* M. McCormack, et al., *Appl. Phys. Lett.*, (USA) **64**, 3045 (1994).

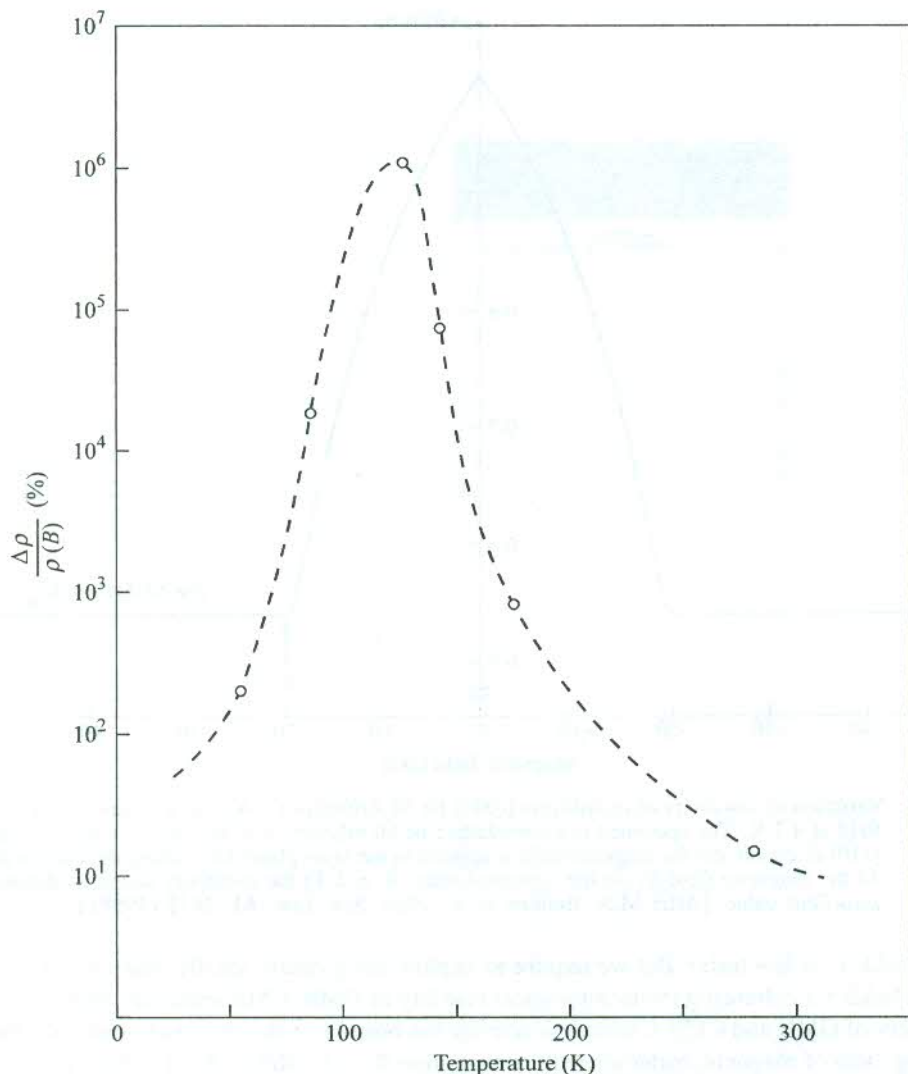


FIG. 14.26 Variation of magnetoresistance of a thin film of La-Ca-Mn-O as a function of temperature. The MR peaks at 110 K in a magnetic field of 6 T. [After S. Jin et al., *Appl. Phys. Lett.*, **67**, 557 (1995).]

leading to lattice strain is detrimental to achieving large MR. The MR improves further on heat treatment.

Several theoretical approaches have been advanced to understand ferromagnetism and the GMR effect in manganites. The ferromagnetism is interpreted in terms of the coupling between charge carriers and the coupling between localized spin moments of Mn ions. The picture of the GMR effect is, however, too complex to be described here. The details fall outside the scope of the present book and, therefore, dispensed with. Nevertheless, we must bring to focus the two most striking features of the GMR-CMR effect in manganites. Firstly, the MR peak can be shifted to occur at room temperature by adjusting the processing parameters. Secondly, the resistivity can be

manipulated by magnetic field to change by orders of magnitude. These keep the material scientists motivated to search tirelessly for ideal GMR–CMR materials and hold the realization of their dream in good stead.

SUMMARY

1. The total magnetic induction inside a ferromagnetic solid is $\mu_0(\mathbf{H} + \lambda\mathbf{M})$, where \mathbf{H} is the intensity of the applied field and λ the Weiss coefficient.
2. The susceptibility of a ferromagnet above the Curie temperature T_c is given by the Curie law

$$\chi = \frac{C}{T - T_c}, \text{ where } T_c = \lambda C$$

3. The interaction energy because of the exchange coupling between spins \mathbf{S}_1 and \mathbf{S}_2 is equal to

$$-2J_{ex}\mathbf{S}_1 \cdot \mathbf{S}_2$$

where J_{ex} is the exchange integral. The J_{ex} is positive for a ferromagnet and negative for an antiferromagnet.

4. The wall separating the domains magnetized in different directions is called the *Bloch wall*. The energy of the Bloch wall per unit area is $2\pi\left(\frac{KJ_{ex}S^2}{a}\right)^{1/2}$, where K is the anisotropy constant and a the lattice constant.
5. In an antiferromagnet, the susceptibility above the Néel temperature varies with temperature according to

$$\chi = \frac{C}{T + \theta}$$

where the ratio θ/T_N is usually greater than one.

6. The observed temperature variation of heat capacity of solids with magnetic ordering near T_c takes place according to

$$C_V \propto \log |T - T_c|$$

where T_c is the critical temperature.

7. The magnon dispersion relation for a one-dimensional monatomic ferromagnet in the limit of low frequencies is

$$\hbar\omega \approx (2J_{ex}Sa^2) \cdot k^2$$

8. The contributions of thermally excited magnons in ferromagnets at low temperatures to the heat capacity and to the fractional magnetization change are both proportional to $T^{3/2}$.

9. The magnon dispersion relation for a one-dimensional monatomic antiferromagnet in the long wavelength limit is

$$\hbar\omega \approx (4J_{\text{ex}}Sa) \cdot k$$

10. The heat capacity contributed by thermally excited magnons in an antiferromagnet varies with temperature as T^3 . This term is in addition to the Debye T^3 term from phonons.
11. An antiferromagnetic crystal possesses no magnetic moment because of the antiparallel alignment of magnetic moments of equal value. The neutron diffraction study furnishes the size of the magnetic unit cell that is different from the chemical unit cell detected by XRD.

PROBLEMS

- 14.1 Show that the magnon dispersion relation for a ferromagnetic cubic lattice with nearest neighbour interactions is

$$\hbar\omega = 2J_{\text{ex}}S \left[z - \sum_{\delta} \cos(\mathbf{k} \cdot \boldsymbol{\delta}) \right]$$

where the summation is over the z vectors denoted by δ that connect the central atom to its nearest neighbours.

- 14.2 If the effective fields on the two sublattices of an antiferromagnet are written as

$$\mathbf{H}_A = (-\gamma \mathbf{M}_B - \eta \mathbf{M}_A); \quad \mathbf{H}_B = (-\gamma \mathbf{M}_A - \eta \mathbf{M}_B)$$

show that

$$\frac{\theta}{T_N} = \frac{\gamma + \eta}{\gamma - \eta}$$

- 14.3 Apply the formalism of the two-sublattice model to a ferrimagnetic solid if the magnetic moments on the two sublattices are of differing strengths.
- 14.4 The Brillouin function $B_J(x)$ is of the form $(Ax - Bx^3)$ for small x , where A and B are positive. Use the mean-field approximation to show that the spontaneous magnetization of a ferromagnet vanishes as $(T_c - T)^{1/2}$ as T_c is approached from below.
- 14.5 Use the mean field theory to derive the following relation for the exchange integral, considering only the nearest neighbour interactions:

$$J_{\text{ex}} = \frac{3k_B T_c}{2zS(S+1)}$$

where z is the number of nearest neighbours.

- 14.6 Assuming that iron in its metallic form has a magnetic moment of 2 Bohr magneton per atom, calculate (a) the Curie constant, (b) the Weiss constant, (c) the saturation magnetization, and (d) the magnitude of the internal field (lattice constant = 2.86 Å; $T_c = 1043$ K).

SUGGESTED FURTHER READING

- Ashcroft, N.W. and N.D. Mermin, *Solid State Physics* (Saunders College, 1988).
- Kittel, C., *Introduction to Solid State Physics*, 7th ed. (John Wiley, 1996).
- Mattis, D.C., *Theory of Magnetism* (Springer, 1985).
- Morrish, A.H., *Physical Principles of Magnetism* (John Wiley, 1966).
- Rado, G.T. and H. Suhl (Eds.), *Magnetism* (Academic Press, 1963).
- Sinha, K.P. and N. Kumar, *Interactions in Magnetically Ordered Solids* (Oxford, 1980).
- Smart, J.S., *Effective Field Theories of Magnetism* (Saunders College, 1966).
- White, R.M., *Quantum Theory of Magnetism*, 2nd ed. (Springer, 1983).

Superconductivity

In the year 1911, Kamerlingh Onnes* observed that the DC resistance of mercury dropped suddenly to an immeasurably small value when cooled to below 4.2 K. The resistance abruptly dropped from 0.084 ohms at 4.3 K to below 3×10^{-6} ohms at 3 K which is ten-millionth of the value at 0°C. The specimen may, therefore, be regarded to have practically lost its DC resistance. The phenomenon showing complete disappearance of the DC resistance below a critical temperature T_c is known as superconductivity. Cooling below T_c is considered to cause a phase transition in the specimen from a state of normal resistivity to a superconducting state.

Several metallic elements (see Table 15.1) and alloys show superconductivity. Semiconductors like Si, Ge, Se and Te become superconductors under high pressure at low temperatures. All but one

Table 15.1 Periodic table showing superconducting elements (light shaded). The dark shaded elements show superconductivity only under pressure. The numerical figures give T_c in K

H																			He
Li* 2.4	Be 0.03																		
Na	Mg* 5.5																		
K	Ca* 4.3	Sc 0.3	Ti 0.39	V 5.3	Cr	Mn	Fe* 0.3	Co	Ni	Cu	Zn 0.9	Ga 1.09	Ge 5.4	As 0.5	Se 6.9	Br	Kr		
Rb	Sr* 3.6	Y 05.27	Zr 0.55	Nb 9.2	Mo 0.92	Tc 7.8	Ru 0.5	Rh 325 μ	Pd* 3.2	Ag	Cd 0.55	In 3.4	Sn 3.7;5.3	Sb 3.6	Te 4.5	I	Xe 7.0		
Cs 1.5	Ba 1.8;5.1	La 4.8;5.9	Hf 0.13	Ta 4.4	W 0.01	Re 1.7	Os 0.65	Ir 0.14	Pt* 0.1	Au	Hg 4.15 3.95	Tl 2.39 1.45	Pb 7.2	Bi 3.9 7.2;8.5	Po	At	Rn		
Fr	Ra	Ac																	
	Co 1.3	Pr* 5.0	Nd* 4.6	Pm	Sm	Eu* 3.4	Gd	Tb	Dy	Ho	Er	Tm	Yb* 2.9	Lu 0.1;0.7					
	Tb 1.37	Pa 1.3	U 0.2	Np	Pu	Am 0.6	Cm	Bk	Cf	Es	Fm	Md	No	Lw					

* Thin film

† Disordered film

Fine powders

* H. Kamerlingh Onnes, *Akad. van Westenschappen* (Amsterdam), **14**, 113, 818 (1911).

allotropic forms of Bi are superconducting with different transition temperatures. This suggests that superconductivity may depend on the crystal structure. This should not be surprising since the electronic band structure varies with the crystal structure. Significantly, none of the ferromagnetic materials (e.g. Fe, Co, Ni) displays superconductivity. The strong molecular magnetic field inside these materials is believed to be the cause, as strong magnetic fields are known to suppress superconductivity as discussed later in the chapter.

The compound superconductors generally show higher transition temperatures, a list of some selected compound superconductors is given in Table 15.2. Superconductors that have transition temperatures around 20 K or below are called conventional or low T_c superconductors and their properties are well explained by the microscopic theory of Bardeen, Cooper and Schrieffer* (famous as the BCS theory). There is a unique and extremely fascinating class of superconductors belonging to the ceramic class like $\text{YBa}_2\text{Cu}_3\text{O}_{7-x}$. These materials are distinguished by relatively much high transition temperatures (around or even more than 100 K), and are, as such, commonly known as high T_c superconductors. They form the subject of modern research in superconductivity. The theoretical scene in this case is, however, uncertain because it is plagued by difficulties of formulating a general theory to deal with widely different characteristics of these materials.

Table 15.2 Some selected compound superconductors with their transition temperatures T_c

Compound	T_c (K)	Compound	T_c (K)
$(\text{ET})_2\text{I}_3^*$	1.4	Nb_3Al	17.5
MO_2BC	7	Nb_3Sn	18.05
La_3In	10.4	Nb_3Ge	23.2
LuRh_4B_4	11.7	$\text{Rb}_2\text{CsC}_{60}$	31.3
NbN	16	$\text{YBa}_2\text{Cu}_3\text{O}_7$	90
V_3Si	17.1	$\text{Tl}_2\text{Ca}_2\text{Ba}_2\text{Cu}_3\text{O}_{10}$	125

*ET = bis-ethylenedithiotetraphiafulvalene.

Like ferromagnetism, superconductivity too is a quantum phenomenon interpreted as a quantum mechanical consequence of the electron-electron interaction. Still, some of the aspects of superconductivity can be understood by making a simple assumption that electrons contributing to superconductivity are different in behaviour from those of an ideal Fermi gas. We organize the plan of this chapter broadly on the following lines:

1. Description of phenomena in which the actual quantization conditions are macroscopically not observable.
2. Energy gap.
3. Description of properties dependent on energy gap.
4. Theoretical basis (isotope effect) for BCS theory: qualitative discussion of the theory and its quantitative predictions.
5. Basic principles of Ginzburg–Landau theory: description of phenomena effectively explained by this theory.
6. A survey of development and properties of high T_c superconductors.

* J. Bardeen, L.N. Cooper and J.R. Schrieffer, *Phys. Rev.*, **108**, 1175 (1957).

15.1 PHENOMENA WITHOUT OBSERVABLE QUANTIZATION

15.1.1 Zero Resistance and Persistent Currents

The disappearance of DC resistance at temperatures below the transition temperature is the foremost dramatic property of superconductors. This is in contrast with the behaviour of normal metallic resistivity that decreases with fall in temperature and approaches a residual value at $T = 0$ K [Fig. 15.1(a)]. The residual resistivity is attributed to the electron scattering from impurities and static imperfections (see Section 6.7).

A schematic of the fall of the DC resistivity of a superconductor is shown in Fig. 15.1(b). In pure materials, the transition at $T = T_c$ takes place very abruptly and the width of the transition region may be less than 10^{-3} K, indicating to a certain cooperative effect involving many electrons that act together. The presence of impurities results in the broadening of the transition width [Fig. 15.1(b)].

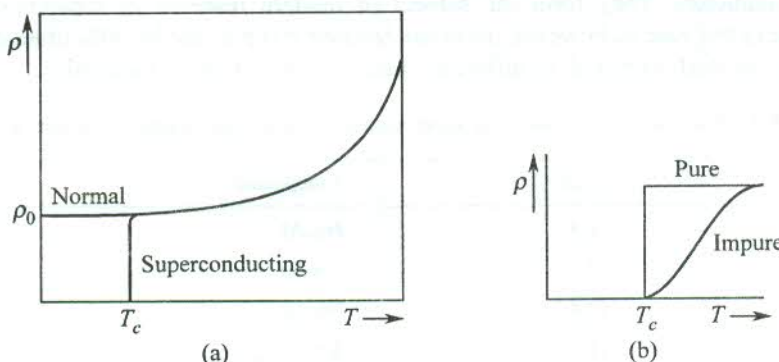


FIG. 15.1 (a) The dc resistivity ρ of a superconductor vanishes abruptly at $T = T_c$. In a normal metal, the resistivity becomes almost constant and levels off at ρ_0 , the value at $T = 0$. The ρ_0 arises purely because of electron scattering from static defects. The normal state below T_c is produced by applying a magnetic field greater than a critical value. The reader must bear this in mind for other measurements to follow. (b) The superconducting transition in a pure and an impure sample is shown. In a pure specimen it is very sharp and the transition width is $\sim 10^{-3}$ K whereas it is appreciably broadened in impure specimens.

Even with today's much improved methods of measurements it is impossible to test whether the resistance is zero; only an upper limit to the value can be set. Onnes determined the small resistances that occur below T_c by measuring the decrease in the value of current in a conducting ring. In this method, a magnetic flux is created through the ring with a magnet and the ring is then cooled below T_c , so that it goes to the superconducting state. With the withdrawal of the magnetic field, a current is induced in the ring as a result of the change in magnetic flux. Should the superconducting ring of inductance L have a finite resistance R , the current flowing in it would decline in accordance with

$$I(t) = I_0 \exp\left(-\frac{R}{L}t\right) \quad (15.1)$$

The measurements indicate that the resistance of a metal decreases by at least 14 orders of magnitude when transformed into a superconductor. Because the DC resistance of a superconductor is practically zero, there must be flowing a very large current. But the supercurrent never exceeds a critical value (the critical current) above which the superconductivity is destroyed. The size of the

critical current is typically of the order of 100 A in a 1 mm wire. This supercurrent is expected to persist forever without any need for a driving electromotive force. S.C. Collins[†] is credited with watching these persistent currents for a record period of $2\frac{1}{2}$ years. Experimentalists have concluded that the decay-time of supercurrents is certainly more than 10^5 years.

At $T = 0$ K, a superconductor responds without dissipation (zero resistance) even to an ac electric field up to a limited frequency. But, at a finite temperature below T_c , there is a small ac loss at all frequencies.

15.1.2 Perfect Diamagnetism: Meissner Effect

Meissner and Ochsenfeld (1933) discovered that a bulk superconductor behaves as a perfect diamagnet in a weak magnetic field by the way of showing zero induction ($\mathbf{B} = 0$) in its interior. Placing $\mathbf{B} = 0$ in relation (13.2), we obtain the value of magnetic susceptibility ($\chi = \mathbf{M}/\mathbf{H}$) as -1 (SI), characterizing a perfect diamagnet. When a superconductor is placed in a weak magnetic field, the magnetic lines of force do not penetrate the specimen but rather go round the specimen as shown in Fig. 15.2 for a superconducting sphere. The exclusion of magnetic field is nearly perfect. The penetration occurs over hardly 10^{-6} to 10^{-5} cm from the surface. This phenomenon is, however, not the true representation of the Meissner–Ochsenfeld effect (commonly known as the Meissner effect). In their original experiment, Meissner and Ochsenfeld placed a single crystal of tin in a weak magnetic field at room temperature. The magnetic field penetrated the specimen at this temperature. When they cooled the crystal to its superconducting transition temperature T_c , they detected an abrupt change in the strength of the magnetic field outside the specimen. This amounts to the magnetic field being pushed out from the interior of the specimen on attaining the superconducting state. Hence, the expulsion and not the screening of magnetic field from the interior of a superconductor is genuinely the Meissner effect.

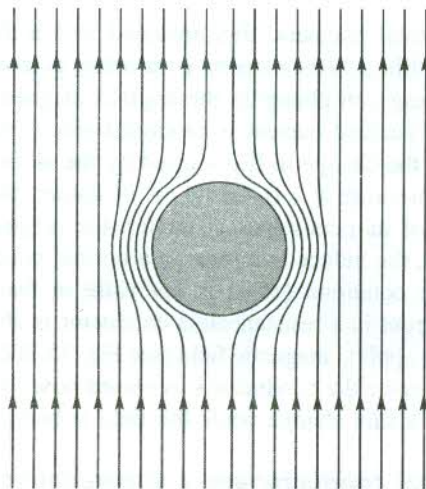


FIG. 15.2 The magnetic flux completely pushed out of the interior of a superconductor (Meissner effect). The material behaves as a perfect diamagnet.

If the magnetic field is increased, maintaining $T < T_c$, to a certain critical value of the field B_c , the superconductor reverts to its normal conducting state and the magnetic field penetrates the specimen. For magnetic field $B \geq B_c$, the specimen shows the normal conducting behaviour.

[†] Quoted in E.A. Lynton, *Superconductivity* (John Wiley, 1969).

Resistanceless conductor

The study of the behaviour of a resistanceless conductor in a uniform magnetic field is crucial to distinguishing between the screening of a magnetic field and the Meissner effect. Suppose a metal cylinder is placed in a magnetic field of uniform flux density (B) [see Fig. 15.3B(a)]. The total magnetic flux (Φ) enclosed within the cylinder is equal to $(B \times S)$, where S is the area of the circular cross-section of the cylinder. If we change the magnetic field, a current will be induced, circulating on the curved surface in a direction so as to create a magnetic flux inside the cylinder that, in accordance with the Lenz's law, opposes the flux change caused by the change in the applied magnetic field. The e.m.f. induced in a normal resistive circuit, while the magnetic field is changing, is expressed as

$$-\frac{d\Phi}{dt} = -S \frac{dB}{dt} = Ri + L \frac{di}{dt}$$

where i is the induced current, and R and L are the resistance and the inductance of the circuit.

When we cool our metal cylinder in the presence of the magnetic field below a certain temperature (T_c) where it practically loses resistance completely, we observe that the flux remains penetrated in the cylinder [see Fig. 15.3B(b)]. The cylinder thus becomes a resistanceless conductor ($R = 0$) and the induced e.m.f. is written as

$$-S \frac{dB}{dt} = L \frac{di}{dt}$$

which, when integrated over the closed current path gives

$$Li + B \cdot S = \text{constant} \quad (15.2)$$

Relation (15.2) gives the total magnetic flux enclosed within the cylinder. It emphasizes that the magnetic flux enclosed within a resistanceless conductor, placed in a uniform magnetic field, is constant and it does not change on changing the applied magnetic field. Due to any change in the applied magnetic field, an induced current is produced whose magnitude is such that the flux generated by it exactly cancels the change in flux caused by the altering applied magnetic field. The induced current flows forever because $R = 0$. Based on its nature, the current is commonly known as persistent current. In view of its persistence character, the original value of flux is maintained indefinitely. On the other hand, the induced currents in a normal conductor quickly die away due to heat dissipation and hence the condition (15.2) is not valid in that case.

The induced persistent current in a resistanceless conductor is able to maintain the internal flux even after the withdrawal of the applied magnetic field [see Fig. 15.3B(c)]. But it is important to notice that the direction of the field outside the conductor is reversed now. It is again explained by applying Lenz's law as there will occur a flux change while the field is being switched off.

Distinction between an ideal conductor and a superconductor

Consider a conductor having been first cooled in the absence of a magnetic field to become an *ideal conductor* below T_c and then a small magnetic field B_a switched on in the region. Before the field is switched on, the ideal conductor ($T \leq T_c$) has no flux inside or outside its body. Therefore, in accordance with relation (15.2), the flux remains zero in its interior even after applying the field. During the short period of steadyng up the magnetic field, the variation of flux induces eddy currents on the surface of the conductor. The magnetic field produced by these currents opposes the applied

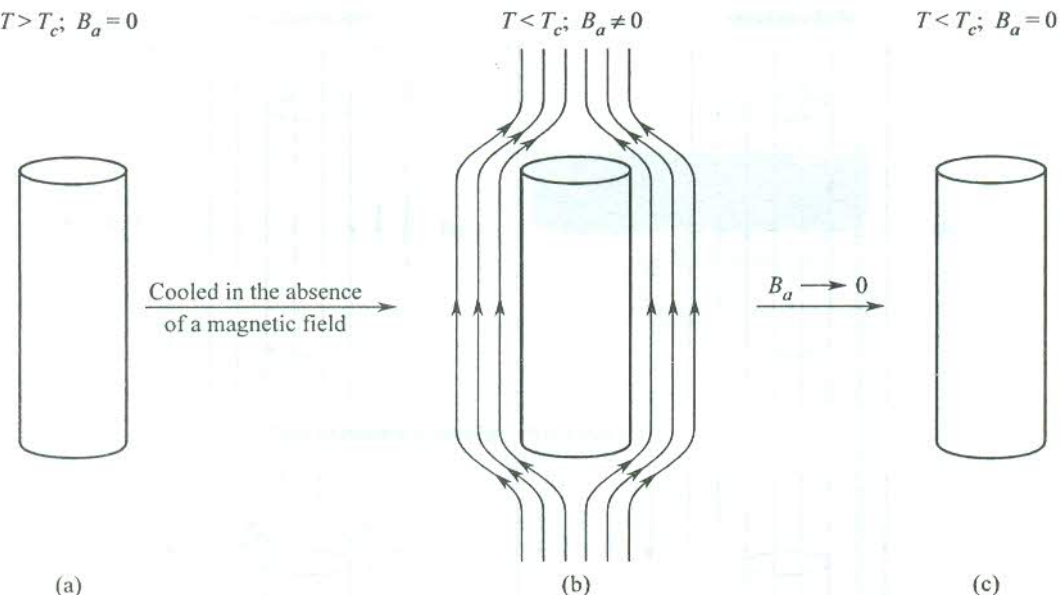


FIG. 15.3A Specimen of an ideal conductor ($R = 0$) or a superconductor cooled in the absence of a magnetic field (specimens of an ideal conductor and a superconductor behave identically under these conditions): (a) The specimen at $T > T_c$ in the absence of the field. (b) The state of the specimen in the presence of a weak magnetic field which is switched on after cooling the specimen through T_c ($T < T_c$). The magnetic flux inside the specimen is zero. (c) The state of the specimen after the magnetic field is switched off. Notice that the flux inside the specimen remains unchanged (zero) in all the states described by (a), (b) and (c).

field inside the conductor and reinforces it outside. This results in zero magnetic induction in the interior of the conductor and the lines of force do not penetrate the conductor. The condition stays on because the eddy currents do not die out and persist almost forever because of the resistanceless nature of the conductor. These persistent currents are commonly known as *screening currents*.

When the specimen of a *superconducting* material is taken through the above process, its response is identical to that of an ideal conductor [Fig. 15.3A(b)]. The eddy screening currents again account for this behaviour. This property is often exploited to shield enclosures from external magnetic fields, by using hollow superconducting cylinders.

Next, consider both the specimens to have been first placed in the region of a weak magnetic field and then cooled through T_c . At temperatures $T > T_c$, the magnetic lines of force penetrate both the types of specimens. But as the temperature decreases to $T < T_c$, the flux remains penetrated only in the specimen of the ideal conductor [see Fig. 15.3B(b)]. On cooling the specimen of the superconductor through T_c , the flux is expelled from its interior (the Meissner effect). While the requirement for the constancy of flux in an ideal conductor explains the observed behaviour in that case, there is no clue to the response of superconductors [Fig. 15.3B(e)]. There is no possibility of even screening currents as the intensity of the magnetic field is held constant throughout.

Another way to distinguish between an ideal conductor and a superconductor is to observe their response to the withdrawal of the magnetic field at temperatures $T < T_c$. If the field is turned on after the cooling, the response is identical and there is no field inside or outside of either of the specimens [see Fig. 15.3A(c)]. But, if the specimens are cooled in the presence of the field, one observes a magnetic field in and around the ideal conductor [Fig. 15.3B(c)], produced by the induced persistent

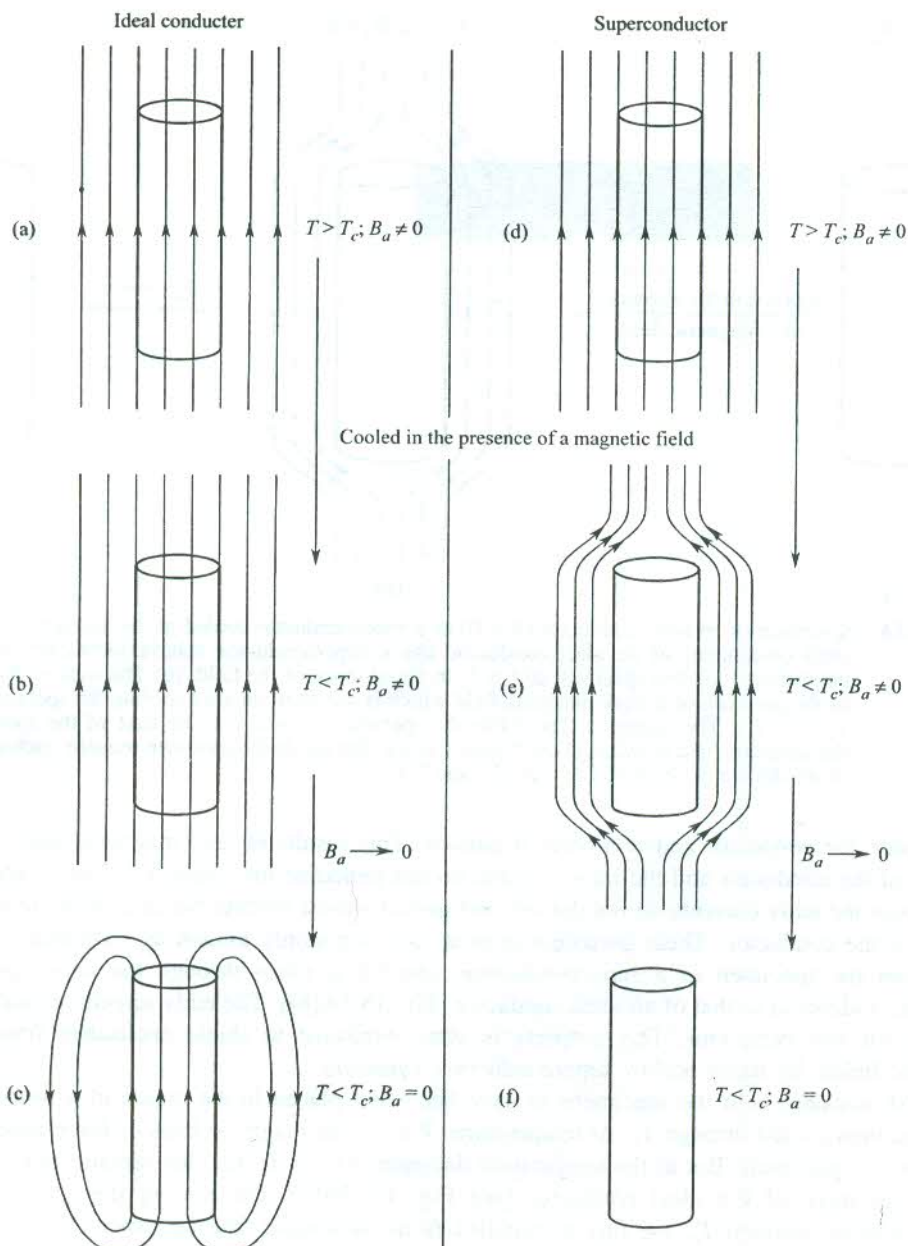


FIG. 15.3B Specimens of an ideal conductor and a superconductor cooled in the presence of a weak magnetic field: (a) The specimen of the ideal conductor at $T > T_c$. (b) The specimen of the ideal conductor when cooled through T_c ($T < T_c$). The flux penetration continues. (c) The state of the specimen of the ideal conductor after the magnetic field is switched off. The net flux inside the specimen remains the same as in (a) and (b). But the direction of the field outside the specimen is reversed. Notice that this state is different from the corresponding state A(c) where the cooling is produced in the absence of the field. (d) The specimen of the superconductor at $T > T_c$. (e) The specimen of the superconductor when cooled through T_c ($T < T_c$). The magnetic flux is expelled from the interior of the specimen (Meissner effect) on reaching T_c . (f) The specimen of the superconductor after the magnetic field is withdrawn. Notice that this state is identical to the corresponding state A(c) where the specimen is cooled in the absence of the field.

currents. Lenz's law demands that the magnetic field produced by these persistent currents support the dying applied field within the body of the ideal conductor. As a consequence the direction of the field produced outside the specimen becomes opposite to the direction of the withdrawn field. It is interesting to find the superconductor in a state identical to the one it acquired when the operations of switching on and switching off the magnetic field followed the operation of cooling through T_c [see Figs. 15.3A(c) and Fig. 15.3B(f)].

The distinction between an ideal conductor and a superconductor as brought out above and sketched in Figs. 15.3A and B clearly shows that the state of an ideal conductor after the withdrawal of the external magnetic field depends on whether the cooling through T_c is carried out in the presence or the absence of the magnetic field. On the other hand, the corresponding state of a superconductor is independent of this aspect. These discussions make it obligatory to regard the Meissner effect as an essential magnetic property of superconductors. In other words, the exhibition of perfect diamagnetism by a resistanceless material which has become resistanceless on cooling in the presence of a magnetic field is taken as the signature of superconductivity. The condition of zero resistance alone does not define superconductivity in complete sense.

15.1.3 London Equations

The zero resistance of the superconductor requires the Maxwell equation for $\text{curl } \mathbf{E}$ to change to

$\text{curl } \mathbf{E} = 0 = - \frac{\partial \mathbf{B}}{\partial t}$ (since, $\mathbf{E} = \rho \mathbf{j}$). It gives the condition,

$$\mathbf{B} = \text{constant} \quad (15.3)$$

leading to the Meissner effect only when the constant is zero.

A phenomenological description of the Meissner effect was first given by F. London and H. London (1935). This description requires a modification of the conventional equations of electrodynamics. Their first attempt was to examine in a quantitative way the expulsion of magnetic flux from the interior of a metal in its superconducting state. Adopting the two-fluid model of Gorter and Casimir (1934) they assumed that at temperatures $T < T_c$, only a fraction n_s/n of the total number of conduction electrons carry the supercurrent. Here n_s denotes the density of the superconducting electrons (the superconducting fluid) and n is the full electron density. The remaining electrons with density $(n - n_s)$ form a 'normal fluid' through which no current can flow without dissipation. The normal current and supercurrent flow in parallel. The current should in fact be entirely the supercurrent because the resistance offered to the flow of supercurrent is zero. Normal electrons are, therefore, ignored in the present discussion.

The equation of motion of superconducting electrons accelerated by a transitory electric field \mathbf{E} is

$$m \frac{d\mathbf{v}_s}{dt} = -e\mathbf{E} \quad (15.4)$$

where \mathbf{v}_s is the mean velocity of electrons.

The current density of superconducting electrons is

$$\mathbf{j}_s = -n_s e \mathbf{v}_s \quad (15.5)$$

Therefore,

$$\frac{d\mathbf{j}_s}{dt} = \frac{n_s e^2}{m} \cdot \mathbf{E} \quad (15.6)$$

which is known as the first London equation.

Taking curl of (15.6), we have

$$\text{curl } \mathbf{E} = \frac{m}{n_s e^2} \frac{d}{dt} (\text{curl } \mathbf{j}_s) \quad (15.7)$$

Using this relation with the Maxwell equation $\text{curl } \mathbf{E} = - \frac{\partial \mathbf{B}}{\partial t}$, we obtain

$$\frac{\partial}{\partial t} \left(\frac{m}{n_s e^2} \text{curl } \mathbf{j}_s + \mathbf{B} \right) = 0 \quad (15.8)$$

The magnetic fields and current densities that can exist in an ideal conductor ($\rho = 0$) are determined by the above equation together with the Maxwell equation

$$\text{curl } \mathbf{B} = \mu_0 \mathbf{j}_s \quad (15.9)$$

assuming that the rate of time variation is so slow that the displacement current can be neglected. The static magnetic field and the static current density are related to each other through (15.9). Any time-independent \mathbf{B} and \mathbf{j}_s could be trivial solutions of (15.8) and, therefore, relations (15.8) and (15.9) are consistent with an arbitrary static magnetic field. This describes the behaviour of an ideal conductor but not the perfect diamagnetism (i.e. the expulsion of a magnetic field) associated with the Meissner effect. If we integrate (15.8) and equate the constant of integration to zero, we get the second London equation:

$$\text{curl } \mathbf{j}_s = - \frac{n_s e^2}{m} \mathbf{B} \quad (15.10)$$

Taking the curl of (15.9), we get

$$\text{curl curl } \mathbf{B} = \mu_0 \text{curl } \mathbf{j}_s \quad (15.11)$$

Then, using the Maxwell equation, $\text{div } \mathbf{B} = 0$ in the identity

$$\text{curl curl } \mathbf{B} = \text{grad div } \mathbf{B} - \nabla^2 \mathbf{B}$$

we get

$$-\nabla^2 \mathbf{B} = \mu_0 \text{curl } \mathbf{j}_s \quad (15.12)$$

Substituting $\text{curl } \mathbf{j}_s$ from (15.10) into (15.12), we have

$$\begin{aligned} \nabla^2 \mathbf{B} &= \frac{\mu_0 n_s e^2}{m} \mathbf{B} \\ &= \frac{1}{\lambda_L^2} \mathbf{B} \end{aligned} \quad (15.13)$$

with

$$\lambda_L = \left(\frac{m}{\mu_0 n_s e^2} \right)^{1/2} \quad (15.14)$$

known as the London penetration depth.

The solution of (15.13) is not uniform in space. It predicts that the magnetic field \mathbf{B} can be present only within a layer of λ_L of the surface. At the same time, the condition (15.3) requires \mathbf{B} to be a constant. Therefore, a constant \mathbf{B} can be a solution of (15.13) only if \mathbf{B} is equal to zero. The Meissner effect is thus predicted by (15.13), as obtained from the second London equation (15.10), which proves to be more restrictive than (15.8). It is, however, vital to emphasize that the above derivation of the second London equation is based on two assumptions:

- (i) The superconductor is resistanceless in the presence of an applied magnetic field.
- (ii) The constant of integration emerging from the integration of (15.8) is zero.

Consider, for example, a semi-infinite superconductor occupying the space on the positive side of the x -axis. Then, relation (15.13) implies that the magnetic field in the superconductor decays exponentially:

$$B(x) = B(0) \exp\left(-\frac{x}{\lambda_L}\right) \quad (15.15)$$

The magnetic field decays exponentially over a surface thickness, equalling the penetration depth, λ_L (Fig. 15.4). It is not the mere smallness of the penetrating field, but this exponential dependence, which is characteristic of the Meissner effect. Experiments on thin films as thin as or thinner than λ_L confirm that the penetration is not complete. Since the value of λ_L is found to be very small (10^{-6} to 10^{-5} cm) in most of the superconductors, the penetration law (15.15) amounts to an almost complete expulsion of the magnetic field from a superconductor of ordinary size.

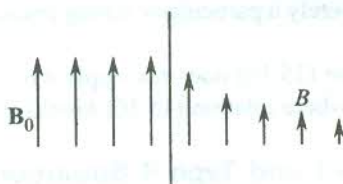


FIG. 15.4 Penetration of the external magnetic flux into a semi-infinite superconductor decreases exponentially with distance from the surface of the superconductor. The distance over which the field drops to $1/e$ of its value outside the superconductor is defined as the penetration depth λ .

For estimating the order of magnitude of the London penetration depth[†], we put in (15.14) m equal to the electron mass and take n_s as the atomic density (i.e. we assume that each atom contributes one superconducting electron). For example, the estimate gives $\lambda_L = 260 \text{ \AA}$ for Sn. The value of λ_L can be considerably greater near T_c where n_s approaches zero.

Diamagnetism of a new kind

The description of the static magnetic properties of most of the normal magnetic materials is based on the following relations, introduced in Chapter 13:

$$\mathbf{B} = \mu_0(\mathbf{H} + \mathbf{M}) \quad [\text{see Eq. (13.2)}]$$

$$\mathbf{B}_0 = \mu_0\mathbf{H} \quad [\text{see Eq. (13.3)}]$$

[†] Relation (15.14) does not describe λ_L precisely, since the London equations are oversimplified. According to the BCS theory the supercurrent is carried by pairs of electrons (Cooper pairs) and not by single electrons. This alters the values of m , n_s and e in (15.14).

$$\chi = \frac{\mu_0 \mathbf{M}}{B_0} = \frac{\mathbf{M}}{\mathbf{H}} \quad [\text{see Eq. (13.5)}]$$

From these, we obtain

$$\mathbf{M} = K \mathbf{B} \quad (15.16)$$

with $K = \frac{\chi}{\mu_0(1 + \chi)}$: a material constant

The persistent current \mathbf{j}_s in a superconductor, placed in magnetic field, is thought to arise from a spatially non-uniform magnetization $\mathbf{M}(r)$ over the penetration depth. The current density \mathbf{j}_s is related to the effective magnetization \mathbf{M} by the following equation*:

$$\mathbf{j}_s = \text{curl } \mathbf{M} \quad (15.17)$$

or

$$\text{curl } \mathbf{j}_s = \text{curl curl } \mathbf{M} \quad (15.18)$$

Using (15.18) in the second London equation (15.10), we obtain

$$\text{curl curl } \mathbf{M} = - \left(\frac{1}{\mu_0 \lambda_L^2} \right) \mathbf{B} \quad (15.19)$$

It is very significant to notice that relation (15.19) gives a different dependence of \mathbf{M} on \mathbf{B} than that represented by relation (15.16), which is true for a normal magnetic material. This underlines the fact that superconductivity is not merely a particularly strong diamagnetism but rather a diamagnetism of a quite new kind.

It may be recalled that relation (15.16) does not apply even to ferromagnets. Superconductors are identified as another example where relation (15.16) breaks down.

15.1.4 Critical Field: Type I and Type II Superconductors

Let us consider a superconductor at a temperature $T < T_c$ in a magnetic field. As the magnetic field is increased to a certain critical value B_c , the superconducting state is destroyed. The critical field limits the amount of current that can flow in a superconductor. As soon as the field owing to the current exceeds B_c , the specimen reverts back to normal state since it is no more free of the magnetic flux. The change of state, in fact, is also advantageous on energy consideration. The value of $B_c(T)$ determines the minimum strength of the magnetic field that destroys superconductivity at a temperature $T < T_c$. It is known as the *critical field*. The value decreases as T_c is approached from below T_c and finally drops to zero at T_c (see Fig. 15.5).

On reducing the field below B_c , the specimen transforms back into the superconducting phase. Annealed samples when tested show only a negligible hysteresis, showing the reversible nature of the superconducting transition. For long thin cylindrical specimens, with the magnetic field applied along their long axis, there are two distinct types of flux penetration:

* M. Abraham and R. Becker, *The Classical Theory of Electricity and Magnetism*, 2nd. ed., I, 4, 6 (Hafner, 1949). In view of the usual relationship, $\mathbf{H} = \mathbf{B}/\mu_0 - \mathbf{M}$, relation (15.17) would require the Maxwell relation $\text{curl } \mathbf{B} = \mu_0 \mathbf{j}_s$ to be replaced by $\text{curl } \mathbf{H} = 0$.

Type I. There is a certain minimum value of the magnetic field $B_c(T)$ below which there is a complete expulsion of the magnetic flux. At this value, the flux abruptly penetrates perfectly into the entire specimen, reverting the specimen to its normal state. The superconducting materials that show this behaviour are called ‘Type I Superconductors’. A schematic of the temperature variation of the critical field $B_c(T)$ is shown in Fig. 15.5. The curve represents a phase boundary between the normal and superconducting states. The parabolic curve is reasonably well represented by the empirical relation:

$$B_c(T) = B_c(0) \left[1 - \left(\frac{T}{T_c} \right)^2 \right] \quad (15.20)$$

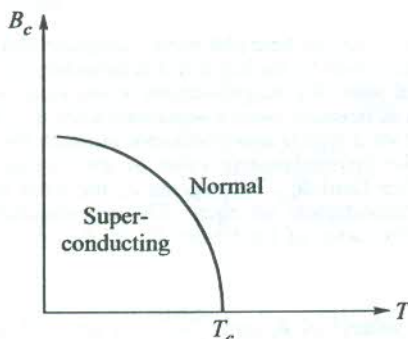


FIG. 15.5 Schematic of the variation of critical magnetic field as a function of temperature. The break near the field axis simply signifies that absolute zero cannot be approached.

The magnetization of these superconductors is illustrated in Fig. 15.6(a).

Type II. There is no penetration of the magnetic field below a certain lower critical field $B_{c1}(T)$ and the penetration begins at this value, and grows further till an upper critical field $B_{c2}(T)$ is reached and the penetration is complete. In the region of the partial penetration from $B_{c1}(T)$ to $B_{c2}(T)$, the specimen assumes a complicated mixed structure of the normal and superconducting states. The specimen is said to be in a *mixed state*, commonly known as a *vortex state* [see Fig. 15.6(b)]. Superconductors with these features are called ‘Type II Superconductors’.

The values of B_c for type I superconductors are typically of the order of 10^2 gauss. These values are too low for any useful application as coils of superconducting magnets. But the so-called *hard* or type II superconductors show high values of B_{c2} . For example, a value of 41 tesla for an alloy of Nb, Al and Ge at 4.2 K and 54 tesla for PbMo_6S_8 are reported in literature* (see also Table 15.3). The hard or type II superconductors have been used as solenoids in superconducting magnets that are capable of producing steady fields of over 200 kG. With these magnets it is possible to carry out the magnetic resonance imaging (MRI), an important application in medical diagnosis.

15.1.5 Thermodynamic Properties

The reversible nature of the superconducting transition enables us to apply thermodynamics for its study. If we neglect the volume changes and consider only the magnetic work term, the Gibbs free energy can be written as

* C. Kittel, *Introduction to Solid State Physics*, 7th ed., p. 340 (John Wiley, 1996).

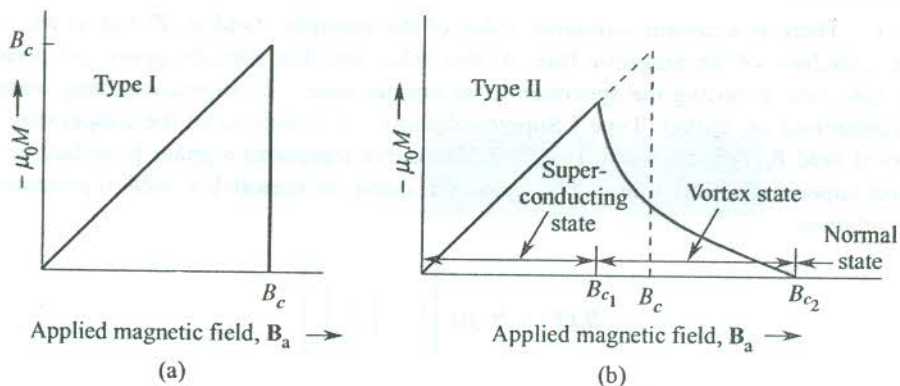


FIG. 15.6 (a) Magnetization versus magnetic field plot shows complete Meissner effect (perfect diamagnetism) for a bulk superconductor which on the basis of this behaviour is labelled as a type I superconductor. Above B_c in the normal state, the magnetization is too small to be measured on this scale. The magnetization is shown as negative since a superconductor is in the diamagnetic state. (b) It shows the magnetization curve for a type II superconductor in which the flux penetration begins at magnetic field B_{c_1} , lower than the thermodynamic value of the critical field B_c . The flux penetration is complete at much higher field B_{c_2} . For a given B_c the areas under the magnetization curves for type I and type II superconductors are equal. The superconductor is said to be in a vortex state (mixed state) between the range of field from B_{c_1} to B_{c_2} .

Table 15.3 Measured values* of B_c and $\frac{\Delta(0)}{k_B T_c}$ for some elemental superconductors

Element	B_c (gauss)	$\Delta(0)/k_B T_c$
Al	99	1.7
Cd	30	1.6
Hg(α)	411	2.3
In	293	1.8
Nb	1980	1.9
Pb	803	2.15
Sn	305	1.75
Ta	830	1.8
Tl	171	1.8
V	1020	1.7
Zn	53	1.6

* Sources as mentioned on pages 729 and 745 of Ref. No. 1 listed for further reading.

$$G = U - TS - \mathbf{M} \cdot \mathbf{B}_a \quad (15.21)$$

and any small change in the free energy owing to a small change in applied field \mathbf{B}_a at a constant temperature is

$$dG = -\mathbf{M} \cdot d\mathbf{B}_a \quad (15.22)$$

where all extensive quantities are defined for a unit volume.

Integrating (15.22), we get

$$\int_{T,0}^{T,B_a} dG = \int_0^{B_a} \left(\frac{\mathbf{B}_a}{\mu_0} \right) \cdot d\mathbf{B}_a$$

$$\left(\text{since for a superconductor, } \mathbf{M} = - \frac{\mathbf{B}_a}{\mu_0} \right)$$

or

$$G_s(\mathbf{B}_a, T) = G_s(0, T) + \frac{B_a^2}{2\mu_0} \quad (15.23)$$

At the critical field B_c , where the normal and superconducting states are in equilibrium:

$$G_n(T) = G_s(B_c, T) \quad (15.24)$$

Here, we ignore any weak magnetism in the normal state and assume that the free energy G_n is independent of field. Then, from (15.23)

$$G_n(T) - G_s(0, T) = \frac{B_c^2}{2\mu_0} \quad (15.25)$$

The above relation shows that in zero field the superconducting state is lower in free energy by $B_c^2/2\mu_0$ per unit volume. For a typical field of $0.1 - 1.0$ kG, this is 10^3 J m^{-3} . In the presence of weak fields below T_c , the specimen has to choose between gaining in energy by forcing all the magnetic flux out (retaining superconductivity) and gaining in energy by letting the flux in (going to the normal state). The superconducting state is found to be energetically favoured for small fields, but not for large fields. The experimental behaviour of free energy as a function of temperature in the two states is shown in Fig. 15.7. Making use of (15.25), we can estimate the critical field $B_c(T)$ from this graph.

The difference of entropies is determined from (15.25) with entropy S defined as $S = -(\partial G/\partial T)$:

$$S_n - S_s = - \frac{B_c}{\mu_0} \frac{dB_c}{dT} \quad (15.26)$$

Since the slope dB_c/dT of the critical field curve (Fig. 15.5) is negative, $S_n \geq S_s$, revealing that the superconducting state is a ‘more ordered state’ than the normal state. Also, the slope dB_c/dT approaches zero at absolute zero, leading to the result $S_n \rightarrow S_s$ as $T \rightarrow 0$, which is consistent with the requirement of the third law of thermodynamics. Figure 15.8 presents a view of the variation of entropy in the two states.

If U_n and U_s denote the internal energy in the normal and superconducting states respectively, then

$$U_n - U_s = T(S_n - S_s) \quad (15.27)$$

This gives the difference in heat capacities for a unit volume as

$$\begin{aligned} C_s - C_n &= T \frac{d}{dT} (S_s - S_n) \\ &= \frac{T B_c}{\mu_0} \cdot \frac{d^2 B_c}{dT^2} + \frac{T}{\mu_0} \left(\frac{dB_c}{dT} \right)^2 \end{aligned} \quad (15.28)$$

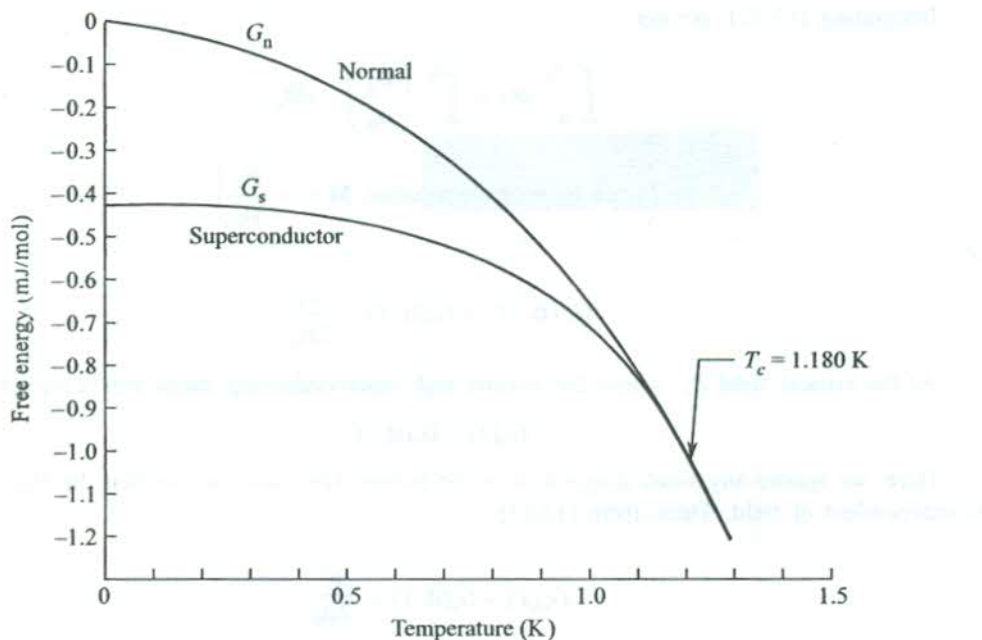


FIG. 15.7 Behaviour of Gibbs energy as a function of temperature in the superconducting and normal states of aluminium. Below the transition temperature, $T_c = 1.180\text{ K}$, the free energy is lower in the superconducting phase. The energies of the two phases merge at T_c . [After N.E. Phillips, *Phys. Rev.*, **114**, 676 (1959).]

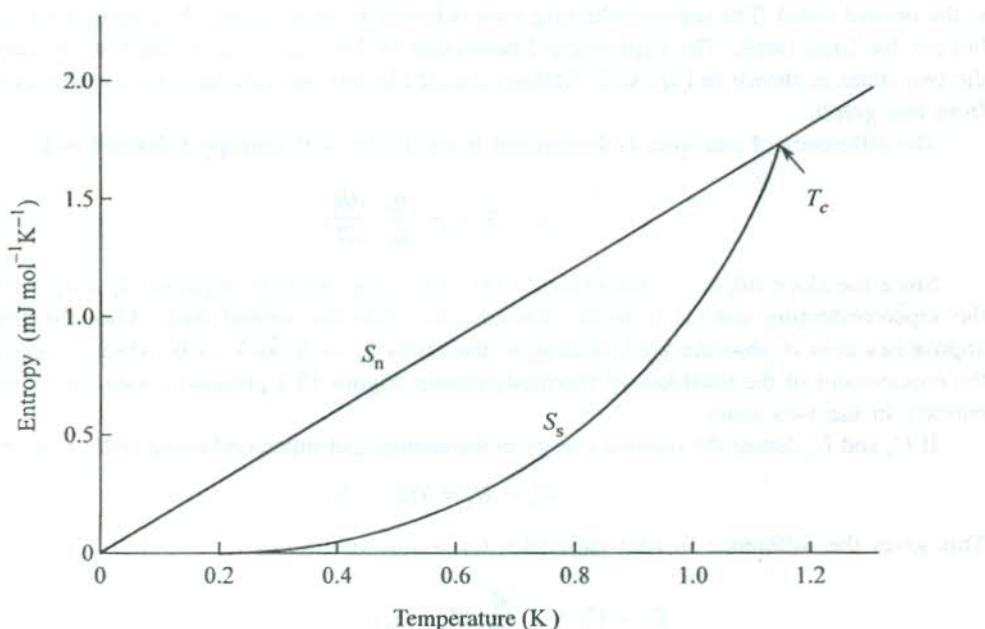


FIG. 15.8 Entropy of aluminium in the normal and superconducting states as a function of temperature. The ordering of electrons lowers the entropy of the superconducting state. [Derived from N.E. Phillips, *Phys. Rev.*, **114**, 676 (1959).]

At $T = T_c$, $B_c = 0$, and then the above relation reduces to

$$C_s - C_n = \frac{T_c}{\mu_0} \left(\frac{dB_c}{dT} \right)_{T=T_c}^2 \quad (15.29)$$

This relation is known as the Ringers formula. Estimates from this formula together with the critical field curve (Fig. 15.5) agree reasonably well with the experimental data.

15.2 ENERGY GAP

The observed temperature dependence of electronic heat capacity below T_c gave evidence for a forbidden energy gap between the normal and superconducting states. At temperatures $T < T_c$, the normal state is created by applying a magnetic field that is equal to or greater than the critical field $B_c(T)$. The measured electronic contribution to the heat capacity at very low temperatures in the

superconducting state is represented by a term of the form $\exp\left(-\frac{\Delta}{k_B T}\right)$ (see Fig. 15.9). This is the characteristic thermal behaviour of a system whose excited levels are separated from the ground state by an energy 2Δ . Figure 15.10(a) shows the conduction band in the normal state while Fig. 15.10(b) shows an energy gap of width 2Δ centred about the Fermi level in the set of allowed one-electron levels in the superconducting state. Electrons in the excited states above the gap behave as normal electrons. The energy gap, however, is not a universal feature of superconductivity. Under a variety of conditions superconductivity occurs even without a gap. For example, the presence of a suitable concentration of magnetic ions causes gapless superconductivity.

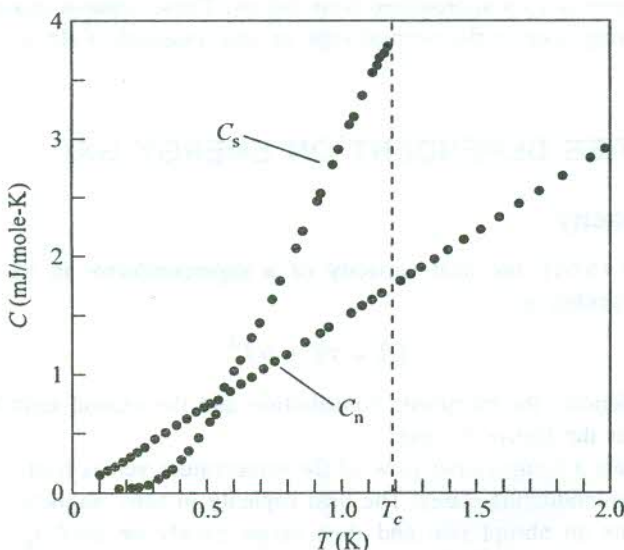


FIG. 15.9 Temperature variation of heat capacity of aluminium in its normal and superconducting states. The Debye temperature for aluminium is quite high. Therefore, electron contribution dominates in the low temperature range shown. At temperatures well below T_c , C_s falls far below C_n which indicates the existence of an energy gap. [After N.E. Phillips, *Phys. Rev.*, **114**, 676 (1959).]

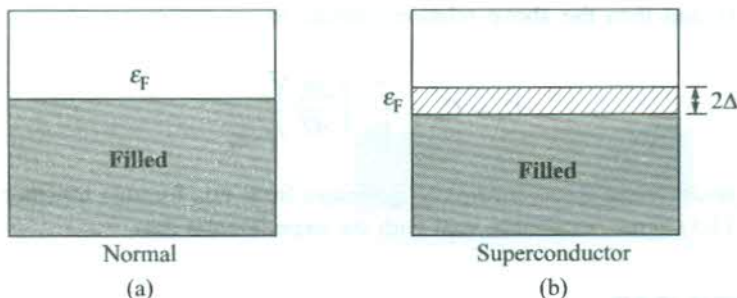


FIG. 15.10 (a) Filled Fermi sea of non-interacting normal electrons. (b) Energy gap (2Δ) centred at the Fermi level ϵ_F in the superconducting state. Electrons occupying excited states above the gap behave as normal electrons at radio frequency fields and a non-zero resistance occurs. Under the action of dc fields, the superconducting electrons eliminate the effect of normal electrons by current along a parallel resistanceless path.

The theoretical analysis reveals that the energy gap in a superconductor occurs due to the electron-electron interaction that orders the electrons in the k -space with respect to the Fermi gas of electrons. This energy gap is entirely of different origin and nature than the gap in insulators where it is caused by the electron-lattice interaction that ties the electrons to the lattice. Theory and experiment both suggest that the energy gap is of the order of $k_B T_c$. Nevertheless, it is found to be a function of temperature such that its size $2\Delta(T)$ increases with the fall of temperature, levelling off to a maximum value $2\Delta(0)$ ($\sim 10^{-4}$ eV) at very low temperatures. This behaviour can be verified from the plot of the reduced gap $\Delta(T)/\Delta(0)$ versus the reduced temperature T/T_c in Fig. 15.11.

The transition from the superconducting state to the normal state does not incur latent heat but gives a discontinuity in the heat capacity (Fig. 15.9). The energy gap (regarded as an order-parameter) falls continuously to zero as T_c is approached from below. These features characterize the transition from the superconducting state to the normal state in zero magnetic field as a second-order phase transition.

15.3 PROPERTIES DEPENDENT ON ENERGY GAP

15.3.1 Heat Capacity

According to relation (6.65), the heat capacity of a superconductor in its normal state at low temperatures may be written as

$$C_V^n = \gamma T + \alpha T^3 \quad (15.30)$$

where the first term denotes the electronic contribution and the second term represents the lattice contribution, famous as the Debye T^3 term.

Figure 15.9 presents a comparative view of the temperature versus heat capacity of aluminium in its normal and superconducting states. The heat capacity in zero magnetic field at the transition temperature T_c exhibits an abrupt rise and then drops slowly on cooling further. At very low temperatures the values fall even below the normal state values, obtained in the presence of a suitable field. A comparison of values observed in the two states in this temperature range shows that the electronic contribution approaches zero much more rapidly in the superconducting state

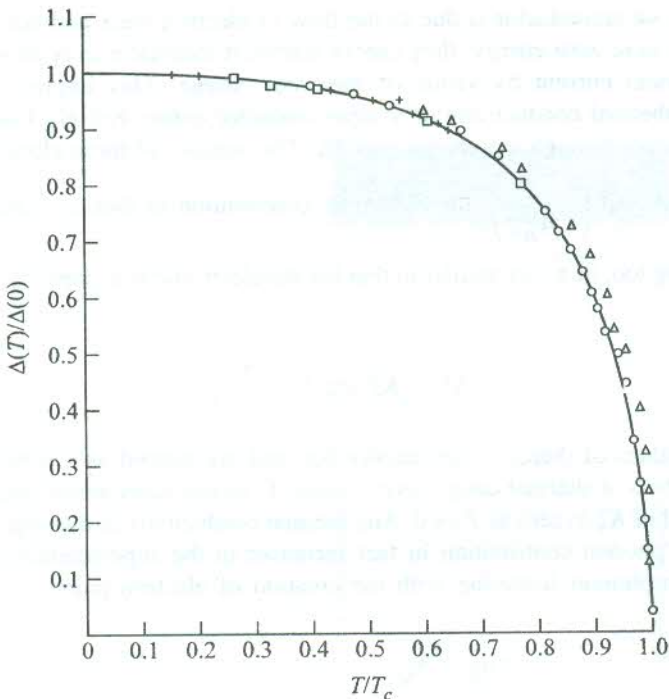


FIG. 15.11 Plot of reduced energy gap $\Delta(T)/\Delta(0)$ versus reduced temperature T/T_c , obtained from tunnelling experiments. The curve represents the BCS prediction. Experimental points: Δ for tin, \circ for tantalum, + for lead and \square for niobium. Estimates of $2\Delta/k_B T_c$ from experimental data on these metals are 3.5, 3.6, 4.3 and 3.8 taken in that order. [After P. Townsend and J. Sutton, *Phys. Rev.*, **128**, 591 (1962).]

than in the normal state where the drop is linear. The drop can be fitted by an exponential term, entailing the expression in the superconducting state to be of the form

$$C_V^s = A \exp \left(-\frac{\Delta}{k_B T} \right) + \alpha T^3 \quad (15.31)$$

where A is a constant and 2Δ is the energy gap.

The electronic contribution represented by the first term in (15.31) depends only on the number of normal electrons. The paired electrons, considered as basis for superconductivity in the BCS model, have zero energy in the ground state and, therefore, do not contribute to the heat capacity.

15.3.2 Thermal Conductivity

Poor thermal conductivity of superconductors is yet another proof of the fact that the one-electron approximation (or the independent-electron approximation) is not applicable to superconductors. As a consequence of this approximation, good conductors of electricity should also be good conductors of heat which is really true with normal conductors. But superconductors contrast the behaviour of normal conductors by exhibiting low values of thermal conductivity, notwithstanding their excellent electrical conductivity. The interpretation to this behaviour is again found in the philosophy that the

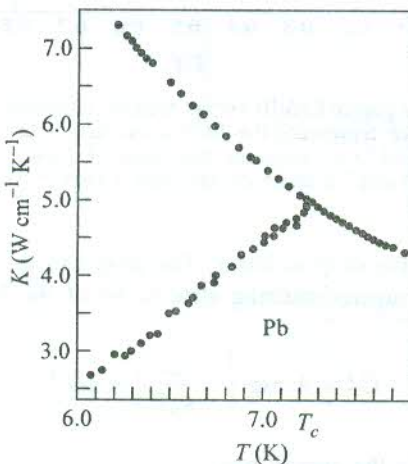
electric current in a superconductor is due to the flow of electron pairs and not of single electrons. Since electron pairs have zero energy, they cannot transport thermal energy though their flow does constitute an electrical current by virtue of their net charge. This implies that the electronic contribution to the thermal conductivity of a superconductor comes entirely from normal electrons whose excitation occurs through the energy gap 2Δ . The number of these electrons being given by

the Boltzmann factor $\exp\left(-\frac{\Delta}{k_B T}\right)$, the electronic contribution to thermal conductivity K_e^s in the

superconducting state too, in a way similar to that for the electronic heat capacity, has an exponential dependence:

$$K_e^s \approx K_e^n \exp\left(-\frac{\Delta}{k_B T}\right) \quad (15.32)$$

Experimental values of thermal conductivity for lead are plotted as a function of temperature in Fig. 15.12. The drop of thermal conductivity below T_c in the superconducting state is due to the rapid exponential fall of K_e^s to zero as $T \rightarrow 0$. Any thermal conductivity in this region is predominantly from phonons. The phonon contribution in fact increases in the superconducting state because of the reduced electron-phonon scattering with the creation of electron pairs.



zero. But photons of energy higher than 2Δ cause excitation to the unoccupied normal energy states above the gap and the resistance approaches its normal state value. The resistance in the superconducting and normal states is essentially the same in this case. With rise in temperature in the superconducting state, the resistance no more remains zero for $\hbar\omega < 2\Delta$, though it is still zero at zero frequency, i.e. in a dc field. The inductive component caused by the inertia of superconducting electrons at finite frequencies does not let them screen the photon electric field completely. This allows the electric field to interact with thermally excited normal electrons, leading to the absorption of incident electromagnetic radiation.

In addition to the inductive component caused by the inertia of superconducting electrons, there is also in general a resistive component of the surface impedance. This causes the power absorption to set in near absolute zero itself in the microwave region where the threshold frequency ($2\Delta/\hbar$) happens to occur. The superconducting transition becomes finally undetectable in the infrared region, as shown in Fig. 15.13 for aluminium.

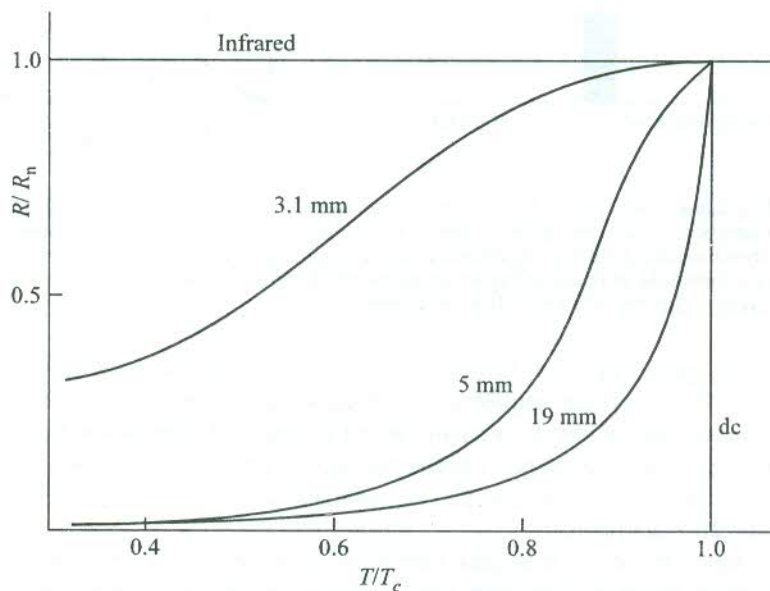


FIG. 15.13 Ratio of the resistance in the superconducting state to that in the normal state as a function of the reduced temperature T/T_c for aluminium in the microwave region. In the infrared region, the superconducting and normal states are not distinguishable ($R/R_n = 1$). [After M.A. Biondi and M.P. Garfunkel, *Phys. Rev. Lett.*, **2**, 143 (1959).]

15.3.4 Normal Tunnelling

The idea of electron tunnelling was introduced in Section 9.10.1 where it was shown as the basis for working of a tunnel diode. A similar tunnelling is known to take place between two metals closely separated by a thin insulating layer ($< 10\text{--}20 \text{ \AA}$) which the electrons can cross by quantum mechanical tunnelling. On applying a difference of potential, the chemical potential of one metal is raised with respect to the other and more electrons tunnel through the insulating film, such that the voltage-current characteristics obey Ohm's law [Fig. 15.14(a)]. Giaever (1962) observed that on replacing one of the metals by a superconductor well below its transition temperature, the voltage-

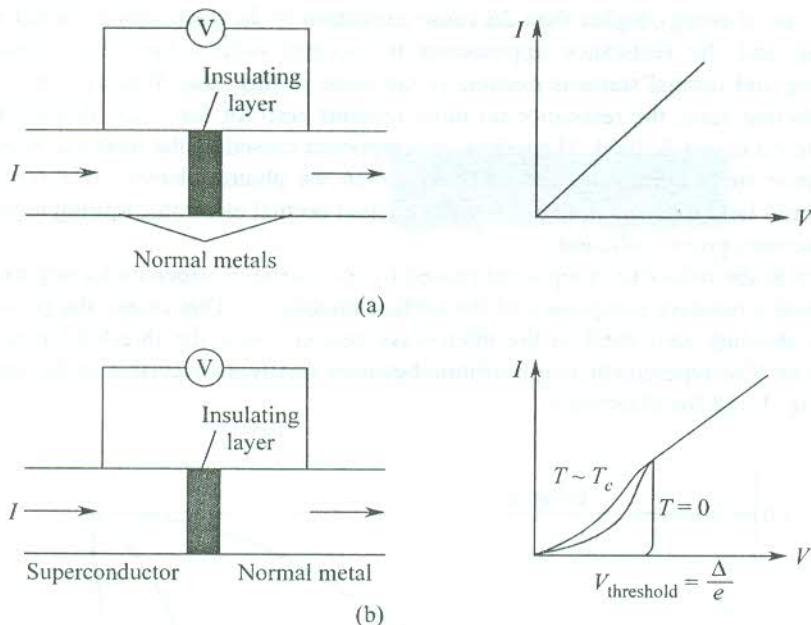


FIG. 15.14 (a) V - I characteristic curve for electron tunnelling from one metal through a thin insulating barrier into another metal. For small voltages, the behaviour is linear. (b) V - I characteristic curve for electron tunnelling from a superconductor through a thin insulating barrier into a metal. It shows a sharp threshold at $T = 0$; at higher temperatures because of thermal excitation of electrons across the energy gap, the blurring effect is evident.

current characteristic appears not as a straight line but as a curve shown in Fig. 15.14(b). At absolute zero no current can flow until the applied potential difference reaches a threshold value $V = 2\Delta/2e = \Delta/e$. At finite temperatures below T_c , a small current is observed even below this voltage because of electrons in the superconductor getting excited through the energy gap. It is an easier experimental method to determine the energy gap. The gap is essentially a measure of the excitation energy that is needed to break an electron-pair.

Josephson's discovery of electron-pair tunnelling between two superconductors sandwiching a thin insulating layer added an altogether new dimension to the applications of superconductors. It is, however, appropriate to defer its description at this stage for developing the theoretical ideas that would enable us to conduct a complete discussion of properties without any repetition. The BCS theory enjoys the status of a successful theory with regard to the interpretation of the properties of liquid helium superconductors. An account of the salient features of this theory follows the description of isotopic effect that gave clue to the basic tenet of the theory.

15.4 ISOTOPE EFFECT

Realizing that solids in which the normal conductivity is not large are more prone to become superconductors, Fröhlich (1950) proposed a model for superconductivity based on electron-phonon interaction. The model assumes that an electron while moving through a crystal lattice continuously emits and reabsorbs virtual phonons. By analogy with his work on polarons (introduced in Section 10.10), Fröhlich pleaded that an electron deforms the lattice in its surrounding

neighbourhood, causing it to oscillate. The electron is then considered to interact with the lattice through an electron-phonon interaction that might produce a ground state of energy lower than the completely filled Fermi sea of non-interacting electrons. The lower ground state, identified with the superconducting state, would then be separated from the normal conducting state by an energy gap. Though Fröhlich's efforts to treat the electron-phonon interactions by perturbation theory failed to make any headway, he was able to suggest on the basis of these interactions that the transition temperature T_c should be proportional to the Debye characteristic temperature θ_D for the isotopes of a given element. The suggestion implies that $T_c \propto M^{-1/2}$, where M is the isotopic mass. This phenomenon, known as the *isotope effect*, serves as an invaluable link in the theory of superconductivity.

Two independent experimental studies*† on isotopes of mercury, about which Fröhlich was unaware, supported his contention. The T_c in mercury changes from 4.185 to 4.146 K for a variation in the average mass M from 199.5 to 203.4 amu. The isotope effect in its generalized form that fits experimental data (see Fig. 15.15) is expressed by

$$T_c M^\alpha = \text{constant} \quad (15.33)$$

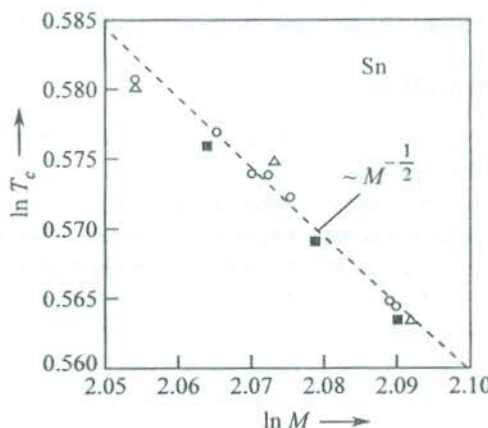


FIG. 15.15 Isotope effect for tin as observed by several workers: Maxwell (○); Lock, Pippard, Schoenberg (■); Serin, Reynolds and Lohman (Δ). [After E. Maxwell, *Phys. Rev.*, **86**, 235 (1952); B. Serin, C.A. Reynolds, C. Lohman, *Phys. Rev.*, **86**, 162 (1952); J.M. Lock, A.B. Pippard, D. Schoenberg, *Proc. Cambridge Phil. Soc.*, **47**, 811, (1951).]

Mostly, the experimental value of α is about (1/2) with Nb_3Sn ($\alpha = 0.08 \pm 0.02$) and Os ($\alpha = 0.15 \pm 0.05$) as the extreme cases. With Coulomb interaction between electrons not taken into consideration, the BCS theory too predicts a value of (1/2). The case of tin is an example in which the BCS- $M^{1/2}$ dependence of T_c is in fine agreement with experiment. The isotope effect is, however, not a universal feature of superconductors. Even some of the liquid helium superconductors (Ru, Zr) to which the BCS is properly applicable do not show isotope effect. The absence of isotope effect in these cases is explained on the basis of their electron band structure.

The isotope effect revealed that electron-phonon interactions are deeply involved in superconductivity. It gave the basic clue to the modelling of the BCS theory.

* E. Maxwell, *Phys. Rev.*, **78**, 477 (1950).

† C.A. Reynolds et al., *Phys. Rev.*, **78**, 487 (1950).

15.5 BCS THEORY: A QUALITATIVE APPROACH

The microscopic theory of superconductivity, famous as the BCS theory, is attributable to Bardeen, Cooper and Schrieffer.*

In this section, we describe the basic principles of this theory in a qualitative way. The all important clue to this theory came from the isotope effect which indicated that the vibrational motion of heavy nuclei must play an essential role in the mechanism of superconductivity. The missing link was established by Cooper. He remodelled Fröhlich's ideas on electron–phonon interaction into the philosophy of an electron–phonon–electron interaction which is now confirmed as the cause of superconductivity in liquid helium superconductors. Cooper demonstrated that with the creation of a condition favourable for a net attractive interaction between two electrons in a conductor, the conductor is transformed from its normal conducting state to its superconducting state. The current in a superconductor is attributed to the flow of the band electron pairs, called *Cooper pairs*. At finite temperatures below the transition temperature, the Cooper pairs find themselves immersed in the Fermi sea of non-interacting electrons. At absolute zero all the electrons in states near the Fermi surface are bound into Cooper pairs and are in the ground state. The existence of Cooper pairs is strongly implied by the experimental evidence of flux quantization [see Section 15.7.1(a)].

15.5.1 Cooper Pair Formation

The theory of superconductivity requires a net attractive interaction between electrons near the Fermi surface. Cooper showed that the ionic motion can overscreen the Coulomb repulsion between two electrons to produce a net attraction if the difference in energies of the two electrons is of the order of $\hbar\omega_D$, where ω_D is the Debye characteristic frequency. Cooper explained the formation of bound electron pairs on the basis of an electron–phonon–electron interaction which materializes through a sequence of events. An electron deforms the lattice in its vicinity, exciting a phonon that travels through the crystal. This phonon is absorbed by a second electron, getting thus coupled to the first electron. Let \mathbf{k}_1 and \mathbf{k}'_1 denote the initial and final wavevectors of the first electron, and \mathbf{k}_2 and \mathbf{k}'_2 denote the initial and final wavevectors of the second electron. Then, the momentum conservation requires,

$$\mathbf{k}_1 - \mathbf{k}'_1 = \mathbf{k}_2 - \mathbf{k}'_2 = \mathbf{k}_{ph} \quad (15.34)$$

where \mathbf{k}_{ph} is the wavevector of the phonon involved in the process.

It must be, however, observed that the condition of energy conservation is met for the crystal on the whole and not for the electron pair because the phonon involved in the exchange is a virtual phonon.

It is easy to show that pairs with zero momentum are most likely to be formed. Consider two electrons with wavevectors \mathbf{k}_1 and \mathbf{k}_2 on the Fermi sphere (Fig. 15.16) so that $k_1 = k_2 = k_F$. The total momentum of the pair is $\mathbf{K} = \mathbf{k}_1 + \mathbf{k}_2$. When $\mathbf{K} \neq 0$, its magnitude is equal to $2k_F \cos \theta$ and only those electrons that lie on the ring shown in the figure can form pairs. On the other hand, for $\mathbf{K} = 0$, i.e. $\mathbf{k}_1 = -\mathbf{k}_2$, all electrons on the Fermi surface can be paired because of the finite phonon

energy $\sim \frac{\hbar^2 k_F \Delta k}{m}$. These electrons are confined in the thickness Δk of the shell on the Fermi sphere. But this does not affect the inference that pairs with $\mathbf{K} = 0$ have the maximum chance of formation.

* J. Bardeen, L.N. Cooper and J.R. Schrieffer, *Phys. Rev.*, **108**, 1175 (1957).

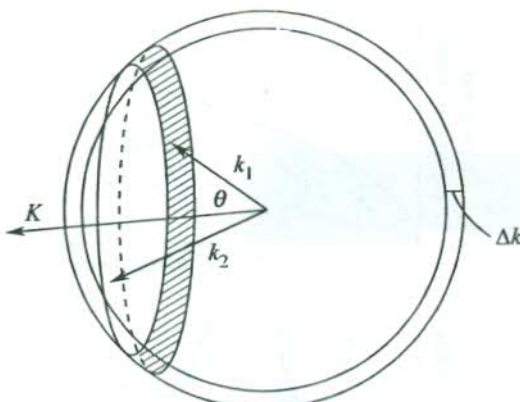


FIG. 15.16 A pair of electron states \mathbf{k}_1 and \mathbf{k}_2 on a shell of a spherical Fermi surface. When $\mathbf{K} = \mathbf{k}_1 + \mathbf{k}_2 = 0$, all states can be paired.

Capitalizing on Cooper's ideas, Bardeen, Cooper and Schrieffer developed a complete microscopic theory according to which favourable conditions for a condensation into bound pairs can exist between electrons having exactly opposing values of wavevectors and opposing spins, i.e. $\mathbf{k}\uparrow$ and $-\mathbf{k}\downarrow$, which is consistent with the condition $\mathbf{K} = 0$.

We find it rather difficult to appreciate that the attractive interaction between any two electrons differing in energy roughly by $\hbar\omega_D$ would be strong enough to cause pairing, especially when the electrons were in isolation. Cooper was able to demonstrate that in the presence of Fermi sphere of additional electrons, the Pauli exclusion principle significantly modified the two-electron problem so that the net attraction need not have a minimum strength to bind a pair. He could also justify very low superconducting transition temperatures compared to other characteristic temperatures of solids. His calculations showing that the binding energy is too small in comparison with the potential energy of attraction, when the attraction is weak, form the basis of these observations.

15.5.2 BCS Ground State

A Fermi gas of non-interacting electrons in its ground state is entirely confined within the Fermi sphere. For exciting the ground state electrons, little energy is required as they need be raised just above the Fermi surface determining the highest populated level. Bardeen, Cooper and Schrieffer extended Cooper's theory to hypothesize a ground state in which all electrons form bound pairs. With an appropriate attractive interaction, this ground state is preferred to correspond to the superconducting state which is separated from its lowest excited state by a finite energy 2Δ .

Figure 15.17 presents a simple visualization of the normal state at $T = 0$, and that of the superconducting state at $T = 0$ and at temperatures in the range $0 < T < T_c$. It is, however, not an exact depiction of the BCS ground state because the illustration has been derived from the Fermi-Dirac representation of density of states which is not applicable to electron pairs behaving statistically as bosons by virtue of their spin value. Nevertheless, this approximate picturization is very helpful in appreciating how in some experiments (e.g. Giaever tunnelling) the density of states are scanned with respect to energy. Figure 15.17(b) shows a zero density of states within an energy range 2Δ centred at the Fermi level ϵ_F and a piling of the displaced states on either side of the gap. It must be noticed that all electrons form Cooper pairs at $T = 0$ because of zero electron occupancy above

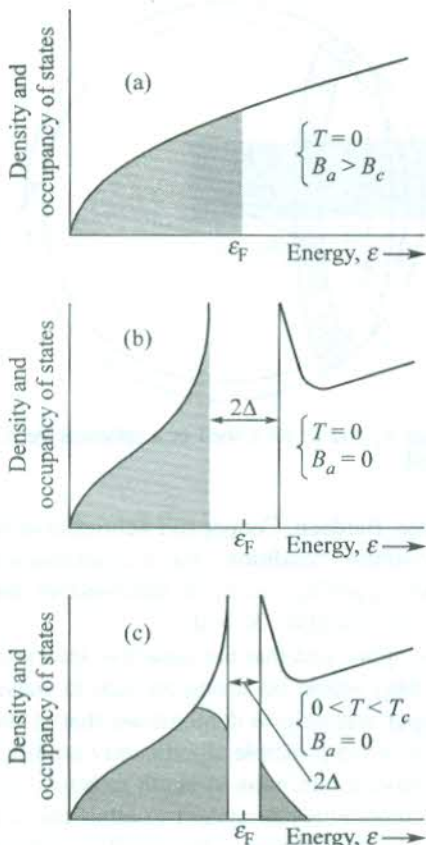


FIG. 15.17 A comparative view of the density of states for a normal conductor (a) and a superconductor [(b), (c)]. In (c), for $0 < T < T_c$ some Cooper pairs break. The released electrons cross the reduced gap.

the gap. At finite temperatures below T_c , the gap decreases [Fig. 15.17(c)] and the Cooper pairs coexist with the non-interacting electrons released by Cooper pairs that break up because of the thermal excitation across the gap.

The knowledge of the ground state wavefunction is of central importance in making theoretical predictions. It is approximated in a manner described below. In a system of N electrons, the electrons are grouped into $N/2$ bound pairs with the state of each pair being described by a wavefunction $\psi(\mathbf{r} s, \mathbf{r}' s')$, where \mathbf{r} is the electronic position and s is the spin quantum number. The product of these $N/2$ identical two-electron wavefunctions may be used to describe the N -electron wavefunction:

$$\phi(\mathbf{r}_1 s_1, \mathbf{r}_2 s_2, \dots, \mathbf{r}_N s_N) = \psi(\mathbf{r}_1 s_1, \mathbf{r}_2 s_2) \dots, \psi(\mathbf{r}_{N-1} s_{N-1}, \mathbf{r}_N s_N) \quad (15.35)$$

This represents a state in which all electrons are present as identical bound electron-pairs. Since the wavefunction ϕ as expressed by (15.35) lacks the symmetry required by the Pauli principle, we must antisymmetrize it so that with the interchange of the space and spin coordinates of any two electrons the antisymmetrized wavefunction changes its sign. Such a wavefunction represents the BCS ground state:

$$\phi_{\text{BCS}} = \mathbf{a}\phi \quad (15.36)$$

where \mathbf{a} is the antisymmetrizer.

The wavefunction ϕ_{BCS} satisfies the Pauli principle, though it is constructed from identical pair function ψ . In contrast to the case of single-electron states, the requirement of antisymmetry does not imply any restriction on the occupancy of two-electron levels in states which are antisymmetrized products of two-electron levels. It shows why it is possible for a pair of fermions to behave statistically like a boson, thus allowing all electron-pairs to condense coherently into a single quantum state.

15.6 IMPORTANT PREDICTIONS OF THE BCS THEORY AND COMPARISON WITH EXPERIMENT

In a quick display of success of the BCS theory, the actual net electron–phonon–electron interaction near the Fermi surface is grossly simplified to a translationally invariant effective interaction U , with conduction electrons being treated in the free-electron approximation. The matrix element of U between two-electron states $\psi(\mathbf{k}_1, \mathbf{k}_2)$ and $\psi(\mathbf{k}_3, \mathbf{k}_4)$ over a volume V is expressed as

$$\langle \psi(\mathbf{k}_1, \mathbf{k}_2) | U | \psi(\mathbf{k}_3, \mathbf{k}_4) \rangle = -\frac{U_0}{V} \quad (15.37)$$

with

$$\mathbf{k}_1 + \mathbf{k}_2 = \mathbf{k}_3 + \mathbf{k}_4$$

and

$$|\varepsilon(\mathbf{k}_i) - \varepsilon_F| < \hbar\omega_D; \quad i = 1, 2, 3, 4.$$

The matrix element vanishes if these conditions of energy and momentum are not met. For a net attraction, therefore, all the four electron energies are required to have values within an amount $\hbar\omega_D$ of the Fermi energy. This puts a restriction on the values of wavevectors involved in a translationally invariant potential.

The most striking feature of the BCS theory is that it yields certain relations in which its two phenomenological parameters U_0 and ω_D do not figure. Barring a few, such as lead and mercury, to all other liquid helium superconductors these relations apply reasonably well. The exceptions mark their identity with a special class known as ‘strong coupling superconductors’. The theory explains the properties of even these superconductors, when applied more rigorously by doing away with the simplifications inherent in (15.37) and using an improved version of phonon effects. We discuss below some of the main quantitative predictions of the theory.

Coherence of the BCS state also follows from the fact that a large number of Cooper pairs are found to be interlocked over the spatial extent of the BCS wavefunction. It is only in the energy range from $(\varepsilon_F - 2\Delta)$ to $(\varepsilon_F + 2\Delta)$ that one-particle occupation in the superconductor is modified compared to that of a normal conductor. The one-particle wavefunctions that constitute the identical two-particle wavefunctions, therefore, originate from this region. This concept helps us in making a crude estimate of the spatial extension of ϕ_{BCS} in the following way.

If we take the energy uncertainty for electrons in Cooper pairs as $2(2\Delta)$,

$$2(2\Delta) \sim \delta \left(\frac{p^2}{2m} \right) \approx \frac{p_F}{m} \delta p$$

where δp denotes the momentum uncertainty.

Using the uncertainty relation, the spatial extension of ϕ_{BCS} is obtained as

$$\begin{aligned}\xi_0 \sim \delta x \sim \frac{\hbar}{\delta p} &\approx \frac{\hbar p_F}{m \cdot 2(2\Delta)} \\ &= \frac{\hbar^2 k_F}{2m \cdot (2\Delta)} \\ &= \frac{1}{k_F} \left(\frac{\varepsilon_F}{2\Delta} \right)\end{aligned}$$

Since $\varepsilon_F/2\Delta$ is typically of the order of 10^3 or 10^4 and $k_F \sim 10^8 \text{ cm}^{-1}$, $\xi_0 \approx 10^3$ to 10^4 \AA .

This magnitude turns out to be of the order of the Cooper pair size, interpreted as the intrinsic coherence length. With $\varepsilon_F/2\Delta \approx 10^4$, we can assume that out of 10^{23} electrons per cm^3 about 10^{19} form Cooper pairs. Therefore, within the space occupied by a single Cooper pair ($\sim 10^{-12} \text{ cm}^3$), there lie centres of gravity of about 10^6 to 10^7 other Cooper pairs. It is thus highly misleading to view Cooper pairs as independent bosons. They are in fact spatially anchored to one another in a very intricate manner. This leads to high coherence and stability of the many-body BCS state, analogical to the photon coherence in a laser beam. Coherence of the BCS state makes it possible for some of the quantum mechanical effects (e.g. flux quantization) to become macroscopically observable.

15.6.1 Critical Temperature

We discussed the superconducting transition more often in terms of the transition temperature which as per the terminology of phase transition should have been mentioned as the critical temperature T_c . On heating a superconductor to its critical temperature, the superconductivity is destroyed; the energy gap vanishes and the conductor reverts back to its normal conducting state. For $\Delta = 0$ and $U_0 D(\varepsilon_F) \ll 1$, the BCS calculations give

$$k_B T_c = 1.14 \hbar \omega_D \exp \left(-\frac{1}{U_0 D(\varepsilon_F)} \right) \quad (15.38)$$

where $D(\varepsilon_F)$ denotes the density of electronic levels of a single spin population at the Fermi energy in the normal conducting state. The interaction parameter U_0 is usually estimated from the electrical resistivity which at room temperature is essentially a measure of the electron-phonon interaction. Relation (15.38) most interestingly reveals that the higher the resistivity (amounting to the higher U_0), the higher is the likelihood for the concerned metal or alloy to become a superconductor on cooling.

The exponential dependence in (15.38) accounts for the observed very low T_c values that are typically one to three orders of magnitude below the Debye characteristic temperature θ_D . It implies that no matter how weak the coupling U_0 , the theory predicts a finite T_c , though it may be even unobservably low in the event of U_0 being very small. The T_c values estimated from (15.38) by and large agree with those observed experimentally. When the T_c value is known, it is possible to evaluate $U_0 D(\varepsilon_F)$ which is regarded as the superconducting coupling constant.

15.6.2 Energy Gap

The BCS theory confirms the existence of an energy gap (2Δ) in the excitation spectrum of a superconductor. As discussed earlier in Section 15.3, it forms the basis for numerous features of superconductors. The experimental methods based on electron tunnelling and optical absorption are usually employed to measure the energy gap.

An expression for the gap at absolute zero, similar to (15.38), is predicted by the theory as

$$\Delta(0) = 2 \hbar \omega_D \exp \left(- \frac{1}{U_0 D(\epsilon_F)} \right) \quad (15.39)$$

with $U_0 D(\epsilon_F) \ll 1$.

Dividing (15.39) by (15.38), we obtain a basic relation from which the phenomenological parameters ω_D and U_0 are absent:

$$\frac{\Delta(0)}{k_B T_c} = 1.76 \quad (15.40)$$

Data in Table 15.3 indicate that this estimate is valid in respect of most of the superconducting elements within about 10 per cent. Large deviations in the case of lead and mercury (~ 30 per cent) should be viewed together with disagreements on other predictions of the simple theory for strong coupling superconductors in general. By abandoning the gross oversimplifications in the interaction Hamiltonian (15.37) and using a more elaborate analysis, the deviations are substantially reduced and the scope of the BCS theory widened. The properties of even strong coupling superconductors are well interpreted in the framework of this broad-based theory.

The simplified BCS theory yields another universal law, describing the temperature dependence of the energy gap near T_c in zero magnetic field:

$$\frac{\Delta(T)}{\Delta(0)} = 1.74 \left(1 - \frac{T}{T_c} \right)^{1/2}, \quad T \approx T_c \quad (15.41)$$

The BCS plot of the above relation together with the experimental points for certain elemental superconductors is shown in Fig. 15.11. The success of the simplified theory in accounting for the continuous drop of the gap to zero at T_c is very much in evidence.

15.6.3 Critical Field

We refer to relation (15.25) which shows that the difference between the free energies per unit volume of the normal and superconducting states is equal to $B_c^2(T)/2\mu_0$, where $B_c(T)$ is the critical magnetic field that destroys superconductivity at a temperature T (of course below T_c). This difference in energy arises since, on the formation of a gap, there occurs a change of energy by 2Δ for a number $\Delta D(\epsilon_F)$ of electrons. Using (15.25), the calculation for a type I superconductor gives

$$\frac{B_c^2(T)}{2\mu_0} = \frac{1}{2} D(\epsilon_F) \Delta^2 \quad (15.42)$$

Fetching the value of $D(\varepsilon_F)$ from the expression for the electron heat capacity[†] and then eliminating the Boltzmann constant with the use of (15.40), we find that near absolute zero

$$\frac{B_c^2(T)}{\mu_0 T_c^2} \approx \frac{1}{2} \gamma \quad (15.43)$$

where γ is the Sommerfeld constant defined as the ratio of the electron heat capacity to the temperature of measurement ($= C_{el}/T$). It may be checked that γ is a function of $D(\varepsilon_F)$ which might differ from metal to metal.

The BCS result (15.43) holds good for a large number of superconductors whose T_c values are spread over a fairly wide range. The simple BCS prediction on $B_c(T)$ is often tested in terms of deviation from the empirical law (15.20), which we rewrite below:

$$\frac{B_c(T)}{B_c(0)} = 1 - \left(\frac{T}{T_c} \right)^2$$

The deviation

$$\frac{B_c(T)}{B_c(0)} - \left[1 - \left(\frac{T}{T_c} \right)^2 \right]$$

from the above law is plotted in Fig. 15.18 along with the corresponding quantity as predicted by the BCS theory for a number of superconductors. The limitation of a simplified BCS theory to deal with the strong coupling superconductors is reflected by the large deviations appearing for lead and mercury.

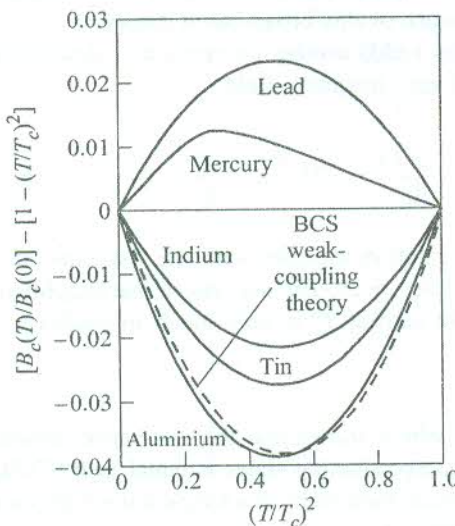


FIG. 15.18 Comparison between experiment and theory (BCS) on the measure of quantity $\left[\frac{B_c(T)}{B_c(0)} - \left(1 - \frac{T^2}{T_c^2} \right) \right]$, representing deviation from the crude empirical relation (15.20) in several metals.

† From (6.62) and (6.65) $C_{el} = \frac{\pi^2}{3} D(\varepsilon_F) k_B^2 T = \gamma T$.

15.6.4 Heat Capacity

The relation for heat capacity as obtained in the framework of the elementary BCS theory supports the observed discontinuity at the critical temperature in zero magnetic field. It can be cast in a form independent of the phenomenological parameters of the interaction Hamiltonian (15.37):

$$\left. \frac{C_s - C_n}{C_n} \right|_{T = T_c} = 1.43 \quad (15.44)$$

This estimated ratio is in good agreement with the measured value for a great number of superconductors. Similar to other predictions, for this one also there is an appreciable departure in the case of strong coupling superconductors (e.g. the measured values of the ratio for mercury and lead are 2.4 and 2.7, respectively).

The simple BCS theory also predicts the exponential drop of the electron heat capacity at low temperature as actually revealed by experiments. The parameter independent form of the prediction is

$$\frac{C_{el}}{\gamma T_c} = 1.34 \left(\frac{\Delta(0)}{T} \right)^{3/2} \exp \left(- \frac{\Delta(0)}{T} \right) \quad (15.45)$$

15.6.5 Acoustic Attenuation

The propagation of a sound wave in a metal causes displacement of ions as a consequence of which microscopic electric fields are produced. These fields are capable of exciting electrons near the Fermi level. The energy is thus removed from the sound wave, resulting in its attenuation. But the attenuation of a sound wave is drastically reduced in the superconducting state because the energy carried by the wave is less than the energy required for the promotion of electrons to their lowest excited state (i.e. $\hbar\omega < 2\Delta$). The BCS theory predicts a reduction in the attenuation coefficient, α , of acoustic waves. The ratio of the coefficients in the superconducting and normal states is expressed as

$$\frac{\alpha_s}{\alpha_n} = \frac{2}{1 + \exp \left(\frac{\Delta}{k_B T} \right)} \quad (15.46)$$

At low temperatures, the above ratio reduces to

$$\frac{\alpha_s}{\alpha_n} = 2 \exp \left(- \frac{\Delta}{k_B T} \right) \quad (15.47)$$

This ratio for elemental superconductors is plotted as a function of temperature in Fig. 15.19. It can be observed that the experimental plots compare reasonably well with the BCS curve.

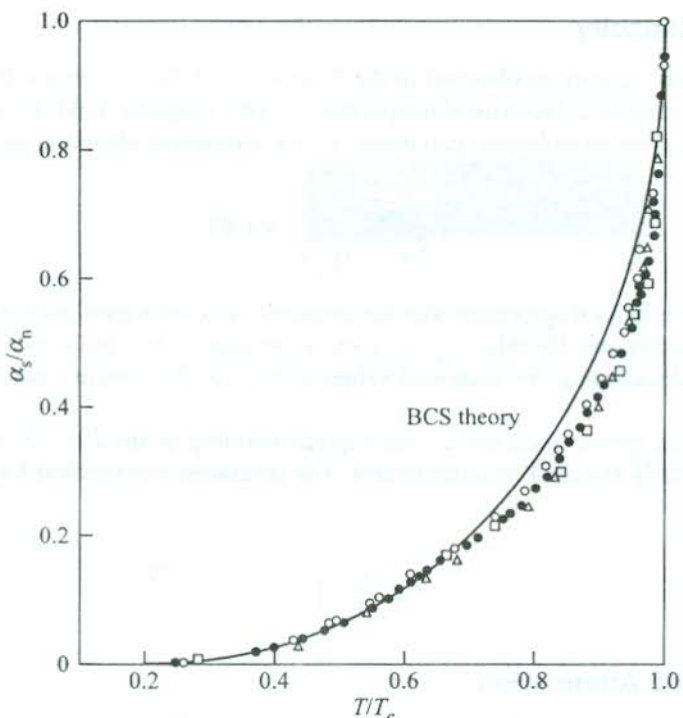


FIG. 15.19 Ratio of attenuation coefficients for acoustic waves in superconducting and normal states as a function of the reduced temperature for tin (\circ at 33.5 MHz; \bullet at 54.0 MHz) and indium (\square at 28.5 MHz; Δ at 35.2 MHz). The curve represents the BCS result. [After R.W. Morse and H.V. Bohm, *Phys. Rev.*, **108**, 1094 (1957).]

15.7 GINZBURG-LANDAU THEORY

Our descriptions of various superconducting phenomena have thus far been conducted under two theoretical approaches: (i) a phenomenological theory effective through the London relations and (ii) the microscopic theory (the BCS theory). But the comprehensive theoretical picture remains incomplete without identifying the impact and consequences of another theory known as the Ginzburg-Landau theory* that had been proposed seven years earlier than the BCS theory. Using the Landau's idea that an ordered thermodynamic phase is characterized by a non-zero order parameter, the theory describes the superconducting state in terms of a complex order parameter $\psi(\mathbf{r})$ that vanishes at T_c . The magnitude of $\psi(\mathbf{r})$ gives a measure of the degree of order at position \mathbf{r} at temperatures below T_c . The theory is accorded a semi-phenomenological status.

The order parameter $\psi(\mathbf{r})$ is viewed as a single-particle wavefunction describing the position of the centre of mass of a Cooper pair in the BCS picture. In a rare exhibition of intuitive skill, Ginzburg and Landau correctly guessed a quantum mechanical equation satisfied by $\psi(\mathbf{r})$. This turned out to be a direct and comprehensive way of describing the characteristics of superconducting phenomena such as the Meissner effect, zero resistivity, flux quantization, type II superconductivity and Josephson tunnelling.

* V.L. Ginzberg and L.D. Landau, *Zh. Eksp. Teor. Fiz.*, **20**, 1064 (1950).

The order parameter is a constant in the ground state of a superconductor where each Cooper pair occupies a translationally invariant state which is independent of the centre of mass coordinate. An applied field or a flow of current would, however, change the order parameter. The Ginzburg–Landau fundamental equation expressing the current density \mathbf{j}_s as a function of the order parameter $\psi(\mathbf{r})$ in a superconductor placed in a magnetic field of vector potential $\mathbf{A}(\mathbf{r})$ is

$$\mathbf{j}_s = -\frac{e}{2m} \left[\psi^* \left\{ \left(\frac{\hbar}{i} \nabla + 2e\mathbf{A} \right) \psi \right\} + \left\{ \left(\frac{\hbar}{i} \nabla + 2e\mathbf{A} \right) \psi \right\}^* \psi \right] \quad (15.48)$$

Here, the current is attributed to the flow of Cooper pairs, i.e. particles of mass $2m$ and bearing a charge $-2e$. If we express the order parameter as $\psi = |\psi| \exp[i\theta(\mathbf{r})]$, assuming that its magnitude $|\psi|$ remains constant and its significant spatial variation occurs entirely through the phase $\theta(\mathbf{r})$, it is straightforward to show that the London equation (15.10) follows from (15.48). A constant value of $|\psi|$ means that the degree of order remains unaffected. This in turn implies that only such disturbances which do not change the Cooper pair density much from its uniform value at thermal equilibrium should be taken into consideration. It is a valid assumption in all those phenomena in which Cooper pairs are in flow but do not accumulate or break up. The flow of current being such an example, relation (15.48) reduces to the form

$$\mathbf{j}_s = - \left[\frac{2e^2}{m} \mathbf{A} + \frac{e\hbar}{m} \nabla \theta(\mathbf{r}) \right] |\psi|^2 \quad (15.49)$$

or

$$\text{curl } \mathbf{j}_s = - \frac{2|\psi|^2 e^2}{m} \mathbf{B} \quad (15.50)$$

(because $\text{curl } \nabla \theta(\mathbf{r}) = 0$ and $\text{curl } \mathbf{A} = \mathbf{B}$)

On identifying the superfluid density n_s with $2|\psi|^2$, relation (15.50) becomes the London equation (15.10). Since ψ represents the wavefunction of particles carrying the charge $2e$, the identity of n_s with $2|\psi|^2$ sounds perfectly logical.

We describe below other features of superconductors whose interpretations are based essentially on the principles of the Ginzburg–Landau theory.

15.7.1 Magnetic Flux Quantization

Consider a superconducting ring placed in a magnetic field \mathbf{B} of vector potential \mathbf{A} (Fig. 15.20). Imagine a closed loop C deep inside the ring. The magnetic field is zero near this loop and so is the supercurrent because any appreciable current can flow only near the surface. Putting $\mathbf{j} = 0$ and replacing $2e$ by q in (15.49), we have

$$\nabla \theta(\mathbf{r}) = \frac{q}{\hbar} \mathbf{A}(\mathbf{r}) \quad (15.51)$$

The order parameter has a unique value at each point which must be such as to minimize the energy. On going round the closed path C once entirely within the ring, the phase $\theta(\mathbf{r})$ can change at most by 2π . Therefore, taking the line integral of (15.51), we get

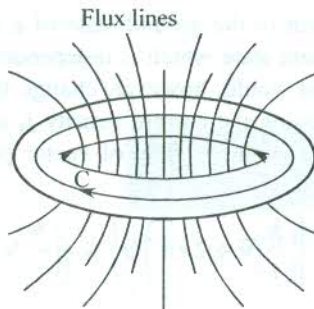


FIG. 15.20 A superconducting ring in a static magnetic field. The total magnetic flux $\Phi (= \phi_{\text{ext}} + \phi_{\text{SC}})$ is quantized; ϕ_{SC} adjusts itself to meet this condition because there exists no quantization condition for the external flux ϕ_{ext} .

$$\frac{q}{\hbar} \oint \mathbf{A} \cdot d\mathbf{l} = \oint \nabla \theta(\mathbf{r}) \cdot d\mathbf{l} = 2n\pi \quad (15.52)$$

Applying the Stokes theorem, we have

$$\oint \mathbf{A} \cdot d\mathbf{l} = \int_c \text{curl } \mathbf{A} \cdot d\mathbf{S} = \int_c \mathbf{B} \cdot d\mathbf{S} = \Phi \quad (15.53)$$

where Φ is the total magnetic flux.

Combining (15.52) and (15.53), we obtain

$$\Phi = n \left(\frac{2\pi\hbar}{q} \right) = n\Phi_0 \quad (15.54)$$

with

$$\Phi_0 = \frac{2\pi\hbar}{q} \quad (15.55)$$

The measured values of the magnetic flux show that $q = 2e$, putting the formation of Cooper pairs in the superconducting state on a firm footing. The fact that the order parameter is single-valued, thus produces the flux quantization in units of $2\pi\hbar/2e$. This unit is called a *fluxoid* or *fluxon*, measuring about 2.0678×10^{-15} tesla m².

15.7.2 Coherence Length

The concept of coherence length is deeply involved in the interpretation of some features of superconductivity such as type II superconductivity, introduced in Section 15.1.4. It was shown in Section 15.1.3 that in a pure semi-infinite superconductor the magnetic field is exponentially damped as one moved from its external surface to its interior. The field decays over a length, the so-called London penetration depth.

Suppose we have a thin superconductor that occupies space on both sides of the x -axis. In this case the magnetic field, applied parallel to the external surface of the superconductor and perpendicular to the x -axis, would not vanish at any point within the superconductor. Instead, the field will have

a minimum at $x = 0$ if the superconductor is placed symmetrically with respect to the origin. This picture is useful in accounting for the behaviour of type II superconductors in a magnetic field. A massive type II superconductor when placed in a magnetic field is considered as a collection of filaments (parallel to the magnetic field) of a normal conductor and a superconductor in an alternating pattern. Whereas energy considerations favour the expenditure of energy for the creation of interfaces between the normal and superconducting regions in type II superconductors, the same is not favourable in type I materials. In this model, the distance from the interface between a normal conductor and a superconductor over which the density of Cooper pairs rises from zero to its maximum value is termed *coherence length*.

Although the coherence length is best introduced into the theory through the Ginzburg–Landau equations which follow also from the BCS theory, its idea was first given by Pippard independently. Pippard defined an intrinsic coherence length ξ_0 as the size of the Cooper pair, i.e. the characteristic distance over which there must exist a correlation of the phases of the paired electrons. He measured the penetration of spatially varying magnetic fields in superconducting tin alloys as a function of alloying and suggested the modification of the London equations. Consider a cylindrical flux tube associated with the supercurrent j_s . The current density j_s , in particular, is found to depend on the value of A in a region of volume and not simply on the value at the same point in space as demanded by the London equation (15.10). These studies required the London equation (the second) to be replaced by a non-local equation

$$j_s(\mathbf{r}) = \int f(\mathbf{r} - \mathbf{r}') A(\mathbf{r}') d\mathbf{r}' \quad (15.56)$$

Equation (15.56) states that the supercurrent at the point \mathbf{r} is contributed by electrons from different points \mathbf{r}' within a volume, approximately ξ_0^3 , where ξ_0 is a measure of the range $f(\mathbf{r} - \mathbf{r}')$. It is also regarded as a measure of the natural scale length over which the spatial variation of the order parameter (i.e. the wavefunction) requires a certain amount of kinetic energy. The increase in kinetic energy must not be more than the energy gap (2Δ) in order to preserve the superconducting state.

The natural scale length (ξ_0) is one of the fundamental lengths (such as the size of the Cooper pair), characterizing a superconductor, all of which are indiscriminately referred to as the coherence length. Well below T_c all such coherence lengths are equal in pure materials. But near T_c or in impure specimens where the mean free paths are small, these coherence lengths may be at variance in different contexts. The value of ξ_0 for pure metals can be as large as a few thousand angstroms at temperatures well below T_c (16,000 Å for aluminium at $T = 0$ K). On alloying, ξ_0 decreases rapidly and is of the order of 100 Å in disordered alloys.

The distance over which the electrons can behave in a coherent manner cannot be larger than their mean free path l . On alloying or adding impurity the mean free path decreases, resulting in the reduction of the effective volume of coherence. The broadening of the superconducting transition in an impure sample (see Fig. 15.1) may be viewed as a consequence of this fact. Both the coherence length ξ and the actual penetration depth λ depend on the mean free path l of electrons measured in the normal state. The effective coherence length in very impure superconductors, where $l \ll \xi_0$, may be expressed by

$$\xi = (\xi_0 l)^{1/2} \quad (15.57)$$

15.7.3 Type II Superconductivity

We refer to Section 15.1.4 where type I and type II superconductors were introduced and it was demonstrated that they show a different Meissner effect [see Fig. 15.6(b)]. It is very much in order to observe that the two types of materials have the same mechanism of superconductivity and differ only in the form of Meissner effect they exhibit. Let us now examine if it is energetically favourable for magnetic fields to partially penetrate a superconductor as is really observed in type II superconductors. Ginzburg, Landau, Abrikosov, and Gorkov have contributed significantly to the theoretical aspects of type II superconductivity. Abrikosov realized that it is the sign of the normal-superconducting interface energy that decides the partial penetration of the magnetic flux. He developed the concept of an interface between a region in the superconducting state and a region in the normal state. He went on to show that the interface energy is negative in type II superconductors above a certain value of the applied magnetic field and that the magnetic field penetrates in the form of quantized flux tubes.

Consider a flux tube with which only one quantum of flux ($\Phi_0 = h/2e$) may be associated. Let it be a cylinder with its axis along the field direction. The field is maximum along the tube axis and decreases to zero along the radius in a distance of the order of the penetration depth λ [see Fig. 15.21(b)]. The order parameter is shown [see Fig. 15.21(a)] to vanish at the axis and acquire its equilibrium value in a radial distance ξ . Figure 15.21(c) shows that the supercurrent density grows to the maximum value over the same distance. When a region of volume $\pi\xi^2$ per unit tube length goes

to the normal state, there is a loss of superconductivity energy $\left(\frac{B_c^2}{2\mu_0}\pi\xi^2\right)$. But there is a gain in the magnetic field energy $\left(\frac{B_a^2}{2\mu_0}\pi\lambda^2\right)$ when the magnetic field penetrates a region of volume $\pi\lambda^2$

per unit tube length. Therefore, the interface energy or the energy of the flux tube per unit tube length may be written as

$$\varepsilon \equiv \frac{B_c^2}{2\mu_0} \cdot \pi\xi^2 - \frac{B_a^2}{2\mu_0} \cdot \pi\lambda^2 \quad (15.58)$$

where B_c is the thermodynamic critical field, B_a is the applied field and $B_c^2/2\mu_0$ represents the stabilization energy density of the superconducting state.

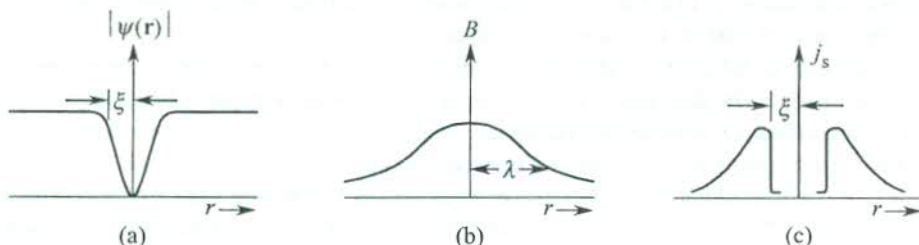


FIG. 15.21 (a) Variation of the order parameter $|\psi(r)|$ as a function of the radial distance from the axis of a cylindrical flux tube. (b) Variation of the magnetic field within a superconductor as a function of the radial distance from the axis of a cylindrical flux tube. (c) Variation of the supercurrent density as a function of the radial distance. It grows to its maximum value (so does the Cooper pair density) over a distance equalling coherence length.

The energy ε is always positive for $B_a < B_c$ if $\xi > \lambda$. It refers to the case of type I superconductors. The energy can be negative, for $\xi < \lambda$ if

$$B_a > B_{c_1} \equiv B_c \left(\frac{\xi}{\lambda} \right) < B_c \quad (15.59)$$

The above condition describes the state of condition in a type II superconductor when it is energetically favourable for the magnetic flux to partially penetrate the superconductor. It is quite reasonable to regard the normal core of radius ξ as a hole in the superconductor and exploit the concept of flux quantization in a superconducting ring. At the interface the field would extend out from the normal core to a distance λ into the superconducting region. Thus the field associated with a tube of radius λ is $\pi\lambda^2 \cdot B_{c_1}$, which must equal the flux quantum Φ_0 , yielding

$$B_{c_1} \approx \frac{\Phi_0}{\pi\lambda^2} \quad (15.60)$$

On raising the field to this value in a type II superconductor, a single fluxoid is nucleated. At a much higher magnetic field B_{c_2} , the flux tubes are packed to the maximum possible density in the superconducting state as may be permitted by the coherence length ξ . With a small fluctuation on the scale of this flux tube order, the field penetrates the superconductor almost uniformly and the superconductivity is destroyed. In some conventional superconductors (liquid helium superconductors), for example in Nb₃Sn wires, large supercurrents have been observed up to fields in the range of 10 tesla. Since each flux tube bears a flux approximately equal to $\pi\xi^2 \cdot B_{c_2}$, we have

$$\pi\xi^2 \cdot B_{c_2} \approx \Phi_0$$

or

$$B_{c_2} \approx \frac{\Phi_0}{\pi\xi^2} \quad (15.61)$$

From relations (15.60) and (15.61), we get

$$B_{c_2} \approx B_{c_1} \left(\frac{\lambda}{\xi} \right)^2 \quad (15.62)$$

It is now possible to relate B_{c_2} with the thermodynamic critical field B_c [see Fig. 15.6(b)], which is crucial to the evaluation of the stabilizing energy per unit volume of the superconductor. Placing the value of B_{c_1} from (15.59) in (15.62), we get

$$B_{c_2} \approx \left(\frac{\lambda}{\xi} \right) B_c \approx \kappa B_c \quad (15.63)$$

where κ is a parameter $\left(= \frac{\lambda}{\xi} \right)$, introduced by Ginzburg and Landau.

The lower critical field B_{c_1} can then be rewritten as

$$B_{c_1} \approx \frac{B_c}{\kappa} \quad (15.64)$$

and from (15.63) and (15.64), we have

$$(B_{c_1} B_{c_2})^{1/2} \approx B_c \quad (15.65)$$

The Ginzburg–Landau parameter κ is small for type I superconductors ($<1/\sqrt{2}$); for example 0.03 for aluminium and 0.15 for indium. It is much larger for the type II superconductors where the coherence length is small because of the characteristic short mean free path.

As shown in Fig. 15.6(b), a type II superconductor is said to be in the vortex state when $B_{c_1} < B_a < B_{c_2}$. The flux tubes are also addressed as ‘vortices’ on account of a vortex-like pattern of supercurrent associated with each tube. The vortex state can have zero resistivity if the vortices do not move under the action of an applied electric field. But if the vortices move, their normal core regions too undergo a displacement which is crudely equivalent to the flow of electrons of a normal metal under the influence of an electric field. Since such a current is dissipative, the system in this condition will be endowed with a non-zero electrical resistance. The movement of the flux tubes is effectively prevented in a system with plenty of such regions in which the presence of the flux tubes may be energetically favourable. For example, a cold-worked metal has a large density of dislocation lines. It may be energetically favourable for the flux tubes to be along or near these lines which can act as pinning centres. This is known as *flux pinning* since it prevents the vortices from moving. There can occur a large current density if there is effective pinning in the superconductor. The maximum current density that can be sustained in a superconductor without making it resistive is called the *critical current*. As the current tends to exceed this value, the superconductivity is destroyed (Silsbee effect). A critical current density of the order of 10^{10} A m^{-2} is possible in good quality films or crystals of some type II materials. The wires of these materials are used in superconducting magnets, producing large fields (~ 10 tesla).

15.7.4 Josephson Tunnelling

Earlier in Section 15.3.4 we discussed Giaever tunnelling that demonstrates single-electron tunnelling from a metal through a thin insulating layer into a superconductor. In 1962, Josephson theoretically showed that an electron pair (the Cooper pair) can also tunnel from one superconductor through a fine insulating layer into another superconductor as shown in Fig. 15.22(a). This is known as *Josephson tunnelling*. The coupling between the two superconductors provided by their insulating barrier must be very weak so that there is a very low probability of finding a Cooper pair in the insulating region. In practice, this is achieved by restricting the barrier thickness to about $10\text{--}20 \text{ \AA}$. An arrangement such as that shown in Fig. 15.22(a) is referred to as a *Josephson junction*. The significant phenomena associated with Cooper pair tunnelling in a Josephson junction are identified as: (i) Josephson Effect and (ii) Supercurrent Quantum Interference.

Josephson effect

We present a basic theoretical description of Josephson effect for an experimental geometry given by Fig. 15.22(b). The interpretation of general expressions reveals two types of effects: the dc Josephson effect and the ac Josephson effect. We will dwell on them at the proper stage of the theoretical development.

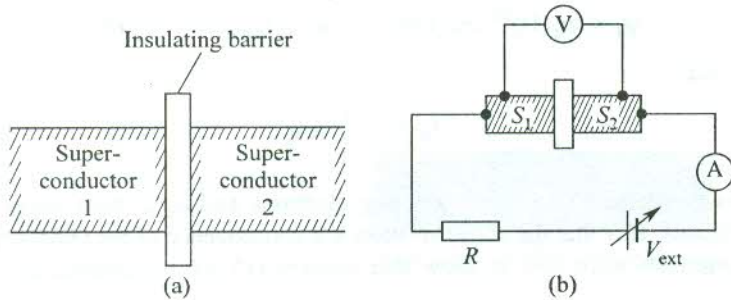


FIG. 15.22 (a) Combination of two superconductors so as to show Josephson tunnelling. (b) Circuit for studying Josephson effect.

For simplicity, we assume that the superconductors \$S_1\$ and \$S_2\$ in our model are of the same material. The temperature being so low, we need to consider the electrons only in their superconducting ground state. The magnetic field near the junction must be screened completely because the highly coherent Cooper pair states are strongly influenced by magnetic fields. Even the magnetic field due to earth may be sufficient to completely obscure the Josephson effect. Let \$\psi_1\$ and \$\psi_2\$ denote the many-particle wavefunctions of the Cooper pair states in the two superconductors and \$\mathcal{H}_1\$ and \$\mathcal{H}_2\$ be the hamiltonians of the respective isolated superconductors. Then, the time-dependent Schrödinger equation of the system gives

$$i\hbar \frac{\partial \psi_1}{\partial t} = \mathcal{H}_1 \psi_1 + T\psi_2 \quad (15.66a)$$

$$i\hbar \frac{\partial \psi_2}{\partial t} = \mathcal{H}_2 \psi_2 + T\psi_1 \quad (15.66b)$$

where \$T\$ is the characteristic coupling constant for the junction and the energy contributions \$T\psi_1\$ and \$T\psi_2\$ simply signify that the many particle wavefunction \$\psi_1\$ or \$\psi_2\$ of one superconductor does not completely vanish in the other. If the junction is characterized with an impenetrable barrier, relations (15.66) reduce to two uncoupled equations for the isolated superconductors because, then, \$T = 0\$.

The circuit in Fig. 15.22(b) shows that when an external difference of potential \$V_{\text{ext}}\$ is impressed, a difference of potential \$V\$ appears across the tunnel junction. When the two superconductors \$S_1\$ and \$S_2\$ are of the same material, as assumed for simplicity, following the perturbation approach, \$\psi_1\$ can be regarded as an approximate solution with respect to \$\mathcal{H}_1\$. This allows us to replace \$\mathcal{H}_1\$ by the energy of the superconducting state. The voltage \$V\$ that appears across the junction creates a relative shift of (2 eV) in the energies of the superconductors \$S_1\$ and \$S_2\$. With zero of the energy scale taken at the midlevel of the energies of \$S_1\$ and \$S_2\$, relations (15.66) transform to:

$$i\hbar \frac{\partial \psi_1}{\partial t} = eV\psi_1 + T\psi_2 \quad (15.67a)$$

$$i\hbar \frac{\partial \psi_2}{\partial t} = -eV\psi_2 + T\psi_1 \quad (15.67b)$$

The wavefunctions \$\psi_1\$ and \$\psi_2\$ are usually regarded as the order parameters in the two superconductors:

$$\psi_1 = (n_c(1))^{1/2} \exp(i\theta_1); \quad \psi_2 = (n_c(2))^{1/2} \exp(i\theta_2) \quad (15.68)$$

Here, we have used

$$|\psi|^2 = \frac{n_s}{2} = n_c$$

where n_s denotes the density of superconducting electrons and n_c is the Cooper pair density.

We saw in Section 15.7 that the above relation is a consequence of the Ginzburg–Landau theory. With this realization we were able to show that relation (15.50) represented the London equation (15.10).

Treating (15.68) as solutions, we place them in (15.67a). The separation of real and imaginary parts gives the following relations:

$$-\frac{\hbar}{2} \frac{\partial n_c(1)}{\partial t} \sin \theta_1 - \left(\hbar \frac{\partial \theta_1}{\partial t} + \text{eV} \right) n_c(1) \cos \theta_1 = T[n_c(1) n_c(2)]^{1/2} \cos \theta_2 \quad (15.69a)$$

$$\frac{\hbar}{2} \frac{\partial n_c(1)}{\partial t} \cos \theta_1 - \left(\hbar \frac{\partial \theta_1}{\partial t} + \text{eV} \right) n_c(1) \sin \theta_1 = T[n_c(1) n_c(2)]^{1/2} \sin \theta_2 \quad (15.69b)$$

On multiplying (15.69a) by $\sin \theta_1$ and (15.69b) by $\cos \theta_1$ and subtracting one from the other, we obtain

$$\frac{\partial n_c(1)}{\partial t} = \frac{2}{\hbar} T[n_c(1) n_c(2)]^{1/2} \sin(\theta_2 - \theta_1) \quad (15.70a)$$

$$\frac{\partial \theta_1}{\partial t} = -\frac{1}{\hbar} T \left(\frac{n_c(2)}{n_c(1)} \right)^{1/2} \cos(\theta_2 - \theta_1) - \frac{\text{eV}}{\hbar} \quad (15.70b)$$

Similarly, from (15.67b), we get

$$\frac{\partial n_c(2)}{\partial t} = -\frac{2}{\hbar} T [n_c(1) n_c(2)]^{1/2} \sin(\theta_2 - \theta_1) \quad (15.71a)$$

$$\frac{\partial \theta_2}{\partial t} = -\frac{1}{\hbar} T \left(\frac{n_c(1)}{n_c(2)} \right)^{1/2} \cos(\theta_2 - \theta_1) + \frac{\text{eV}}{\hbar} \quad (15.71b)$$

Since we have assumed that the two superconductors are of the same material, $n_c(1) = n_c(2) = n_c$; using this condition in the relations (15.70) and (15.71), we get the following two equations:

$$\frac{\partial n_c(1)}{\partial t} = -\frac{\partial n_c(2)}{\partial t} = \frac{2T}{\hbar} n_c \sin(\theta_2 - \theta_1) \quad (15.72a)$$

$$\hbar \left(\frac{\partial \theta_2}{\partial t} - \frac{\partial \theta_1}{\partial t} \right) = 2 \text{ eV} \quad (15.72b)$$

These equations describe the V - I characteristics of a Josephson tunnel diode as depicted in Fig. 15.23. For a comprehensive understanding of the observed characteristic curve shown in Fig. 15.23, we conduct the discussion in two steps.

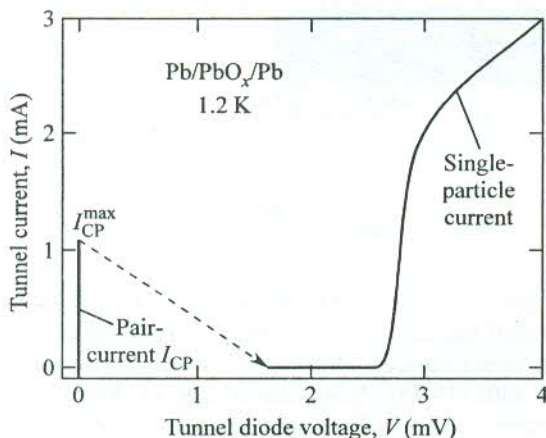


FIG. 15.23 V - I characteristic curve for a $\text{Pb}/\text{PbO}_x/\text{Pb}$ Josephson tunnel diode. [After D.N. Langenberg, D.J. Scalapino and B.N. Taylor, *Proc. IEEE*, **54**, 560 (1966).]

Step I: The dc Josephson effect. It is interesting to notice that relations (15.72) have a non-zero solution for current ($\partial n_c / \partial t \neq 0$) even when there is no voltage drop across the diode ($V = 0$). This implies that as soon as the contact across the junction is complete, there flows a tunnel current of Cooper pairs in a direction determined by the phase difference ($\theta_2 - \theta_1$) between the wavefunctions on the two sides of the tunnel barrier. It is a significant observation that the voltage drop V across the junction is zero though a voltage V_{ext} has been applied externally. The current flowing in the circuit in this condition is purely the tunnel current of Cooper pairs I_{CP} . This phenomenon is called the *dc Josephson effect*. The tunnel current is collected and replaced at the terminals of the external source of voltage in the circuit. This rules out any charge asymmetry that might arise on account of the flow of current. The dc Josephson current I_{CP} is thus kept constant and it has only one value initially at $V = 0$.

But with increase in V_{ext} , the I_{CP} also rises to a maximum value $I_{\text{CP}}^{\text{max}}$. If V_{ext} is increased further, the state becomes unstable and a potential difference now appears ($V \neq 0$) across the diode. The current I_R in this state depends on V_{ext} , V , and the external resistance R ; and the characteristic curve (beyond the arrowhead in Fig. 15.23) is determined by the single electron tunnelling [see Fig. 15.14(b)]. The electrons owe their presence to the breaking of Cooper pairs.

Step II: The ac Josephson effect. As far as the phase difference ($\theta_2 - \theta_1$) is time-invariant, in accordance with (15.72a) $I_{\text{CP}}^{\text{max}}$ remains stable. But (15.72b) tells us that this state is maintainable only if there is no voltage drop across the diode ($V = 0$). We saw above that an increase in V_{ext} that causes I_{CP} to exceed $I_{\text{CP}}^{\text{max}}$ results in the collapse of I_{CP} and the creation of a potential difference V (purely corresponding to the single-electron tunnelling current) across the diode. In the event of this voltage drop, the phase difference between the two states of the superconductor begins to grow with time according to relation (15.72b). We integrate (15.72b) to obtain

$$\theta_2 - \theta_1 = \frac{2 e V t}{\hbar} + \Delta\theta_0 \quad (15.73)$$

where $\Delta\theta_0$ represents the initial phase difference.

On placing the value of $(\theta_2 - \theta_1)$ from (15.73) in (15.72a), we obtain a relation for current that represents an alternating current:

$$\tilde{I}_{CP} \approx \frac{\partial n_c(1)}{\partial t} = \frac{2 T n_c}{\hbar} \sin(\omega_{CP} t + \Delta\theta_0) \quad (15.74)$$

where

$$\omega_{CP} = \frac{2 e V}{\hbar} \quad (15.75)$$

The phenomenon of generating an alternating current by producing a dc voltage drop across a Josephson junction is called the *ac Josephson effect*. It must be clear that the alternating current \tilde{I}_{CP} is in addition to the direct current contributed by single-electron tunnelling.

A simple calculation with (15.75) shows that a drop of mere 1 mV across the tunnel diode produces an alternating current of 3×10^{12} oscillations per second which correspond to a frequency in the infrared region of the electromagnetic radiation. The relation (15.75) implies that a photon energy $\hbar\omega_{CP} = 2 \text{ eV}$ must be absorbed or emitted as a Cooper pair tunnels through a Josephson junction. It provides a basis for an accurate measurement of the ratio h/e .

There are several applications of the Josephson effect. For example, the construction of binary switching devices in microelectronics is based on the two states of the Josephson junction, i.e. $I_{CP} \neq 0$ at $V = 0$, and single electron tunnelling at $V \neq 0$. These devices are very fast and are employed for computer data storage.

Supercurrent quantum interference

The Josephson tunnelling in the presence of a magnetic field provides strong evidence for the highly coherent nature of the superconducting state. Two Josephson junctions arranged in a parallel combination are placed in a region in which a magnetic field \mathbf{B} is impressed as shown in Fig. 15.24. A supercurrent starting in region I is divided into two parts and made to flow along parallel paths,

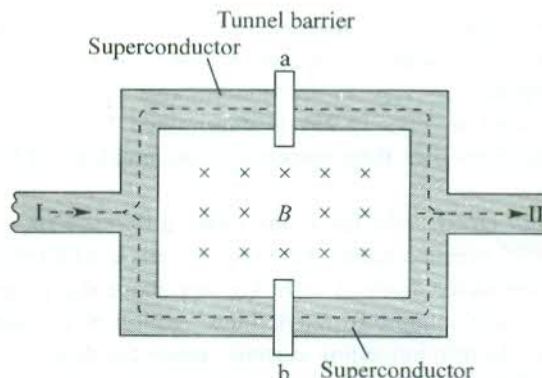


FIG. 15.24 Experimental geometry for producing supercurrent quantum interference. The phase difference of the total Cooper pair wave functions in region I and region II is monitored by the magnetic flux density \mathbf{B} that penetrates the ring.

each of which contains a tunnel junction. The currents I_a and I_b crossing the tunnel barriers 'a' and 'b', respectively, reunite in region II. The combined current shows oscillations characteristic of an interference pattern produced by two coherent sources. By analogy with the interference of light, I_a and I_b are regarded as two coherent sources of current whose disturbances, when superposed by the way of recombination, produce an interference pattern.

In view of relation (15.73), the tunnelling of Cooper pairs causes a phase shift of the total wavefunction of the superconducting state in region II relative to that in region I. If the phase shifts at the two barriers in the absence of the magnetic field be δ_a and δ_b , the supercurrents through the two junctions can be written as

$$I_a = I_0 \sin \delta_a \quad (15.76a)$$

$$I_b = I_0 \sin \delta_b \quad (15.76b)$$

We refer to relation (15.49) to determine the phase difference between the two regions I and II in the presence of a magnetic field of vector potential \mathbf{A} . The relation expresses the supercurrent density \mathbf{j}_s which can be taken as zero, deep inside the superconductor. Placing $\mathbf{j}_s = 0$ in (15.49), we have

$$\nabla \theta = \frac{2e}{\hbar} \mathbf{A}$$

Taking a line integral of the above equation along a path between two points P and Q deep inside the superconductor,

$$\Delta \theta \Big|_{\text{P}}^{\text{Q}} = \int_{\text{P}}^{\text{Q}} \nabla \theta \cdot d\mathbf{l} = \frac{2e}{\hbar} \int_{\text{P}}^{\text{Q}} \mathbf{A} \cdot d\mathbf{l} \quad (15.77)$$

Therefore, the total phase shifts in the wavefunction along the two paths from region I to region II can be expressed as

$$\Delta \theta \Big|_{\text{I}}^{\text{II}} = \delta_a + \frac{2e}{\hbar} \int_{\text{a}} \mathbf{A} \cdot d\mathbf{l} \quad (15.78a)$$

$$\Delta \theta \Big|_{\text{I}}^{\text{II}} = \delta_b - \frac{2e}{\hbar} \int_{\text{b}} \mathbf{A} \cdot d\mathbf{l} \quad (15.78b)$$

The two phase shifts must be identical because the wavefunction has a unique value at every point. Furthermore, the two line integrals in (15.78a) and (15.78b) are taken in opposite directions. Therefore, when taken together they give an integral over a closed path. Using this property and taking the phase shifts (15.78) for the two parallel paths as identical, we obtain

$$\delta_b - \delta_a = \frac{2e}{\hbar} \oint \mathbf{A} \cdot d\mathbf{l} = \frac{2e}{\hbar} \int \mathbf{B} \cdot d\mathbf{S} \quad (\text{using the Stokes theorem}) \quad (15.79)$$

The above relation states that the total phase difference around the loop can be controlled by varying the magnetic field. The general expressions for δ_a and δ_b in (15.76) may, however, be put as

$$\delta_a = \delta_0 - \frac{e}{\hbar} \int \mathbf{B} \cdot d\mathbf{S} \quad (15.80a)$$

$$\delta_b = \delta_0 + \frac{e}{\hbar} \int \mathbf{B} \cdot d\mathbf{S} \quad (15.80b)$$

where for the sake of generality we have introduced an arbitrary phase shift δ_0 that depends on the nature of the tunnel barrier and the applied voltage.

Inserting the values of δ_a and δ_b from (15.80) in (15.76), we obtain the total recombined supercurrent:

$$I = I_a + I_b = 2I_0 \sin \delta_0 \cos \left(\frac{e}{\hbar} \int \mathbf{B} \cdot d\mathbf{S} \right) \quad (15.81)$$

The cosine interference term characterizes the total current. This phenomenon is called the *supercurrent quantum* interference. Its maxima are determined by the condition,

$$\int \mathbf{B} \cdot d\mathbf{S} = m \frac{\pi \hbar}{e} = m \left(\frac{\hbar}{2e} \right); \quad 1, 2, 3, \dots \quad (15.82)$$

$$= m \text{ (flux quantum)}$$

This condition states that for every addition of a flux quantum to the enclosed flux, a new maximum appears. The total supercurrent is plotted as a function of magnetic field in Fig. 15.25 to demonstrate the quantum interference where each oscillation corresponds to a change of flux quantum. Based on this principle, extremely sensitive magnetometers have been developed. Even extremely weak magnetic fields such as those produced by currents in human brain can be measured with these magnetometers. This magnetometer is called a SQUID (Superconducting Quantum Interference Device).

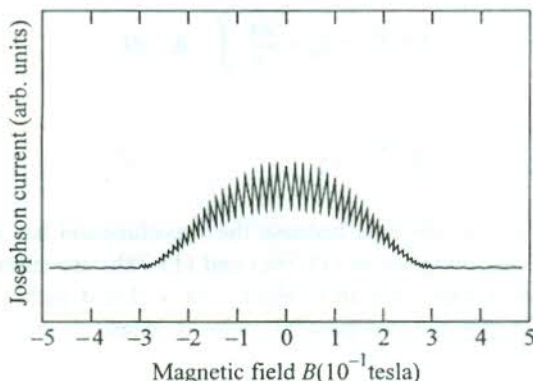


FIG. 15.25 Total supercurrent in region II as a function of the magnitude of the magnetic field, penetrating the loop shown in Fig. 15.24. The plot is typically an interference pattern produced by the superposition of two supercurrents I_a and I_b that have tunnelled two separate Josephson junctions 'a' and 'b'. [After R.C. Jaklevic, J. Lambe, J.E. Mercereau, A.H. Silver; *Phys. Rev.*, **140**, A1628 (1965).]

15.8 HIGH TEMPERATURE SUPERCONDUCTORS (HTS)

Extremely low critical temperatures of conventional superconductors (the low T_c type) put the most serious limitation on their use in technological applications. Working with devices that have to be cooled to temperatures in the range of liquid helium temperature (4.2 K) is obviously not viable on any count. This has kept the scientists world over relentlessly trying to discover superconductivity near room temperature. A decisive boost to this optimism came in 1986, when Bednorz and Müller synthesized metallic oxygen-deficient copper oxide compounds of La-Ba(Sr)-Cu-O system with the transition temperature of about 30 K. A vigorous activity towards the search for materials with higher critical temperatures ensued following this nobel prize winning announcement. It has resulted in the development of a variety of materials with the highest critical temperature T_c observed in the vicinity of 135 K in a mercury cuprate. Under pressure this T_c value approaches 165 K which is not far away from the temperature of the coldest regions on Earth (183 K). The T_c values being so high compared to those of conventional superconductors, these materials are called *high temperature superconductors* or *high T_c superconductors* (HTS).

The scope of this book does not permit us to do justice to the explosive development of HTS and their properties. Nevertheless, we give below an account of the structures and other salient features of some materials that represent the main classes of HTS in the order of their discovery.

15.8.1 Rare-earth Cuprates: Structural Aspect

Chu and Coworkers (1987) earned the distinction of raising T_c to 90 K in ceramics of the $\text{Ba}_{1-x}\text{Y}_x\text{CuO}_{3-y}$ system. With fastly improving methods of preparation of characterization, a ceramic alloy $\text{Y}_1\text{Ba}_2\text{Cu}_3\text{O}_{7-x}$ could be prepared even in single crystal form. In all respects including application this has emerged as the most thoroughly studied and tested system, often referred to as YBCO. A series of this class of HTS has been produced with the Y atom being replaced by other rare-earth elements such as Eu and Gd. On the basis of their stoichiometry, these types of ceramics are commonly called 123 systems.

The crystal structure of the YBCO system is illustrated in Fig. 15.26(a). It can be represented by an orthorhombic primitive cell in the superconducting state. The structure is essentially an oxygen-defect modification of the perovskite structure with about one-third oxygen positions vacant. All members of this series are axial crystals with alternating CuO_2 planes [$\text{Cu}(2), \text{O}(2)$] and oxygen atoms in both pyramid-type and rectangular coordination along the c -axis. Oxygen chains are formed along the b -axis with the involvement of atoms in the rectangular planar structure. We will see a little later that the oxygen vacancies in this chain may be interpreted to be actively involved in the mechanism of superconductivity.

15.8.2 Bi-based and Tl-based Cuprates: Structural Aspect

This class of HTS emerged within a year of the synthesis of 123 systems. These materials, typically represented by $\text{Bi}_2\text{Sr}_2\text{Ca}_2\text{Cu}_3\text{O}_{10}$ and $\text{Tl}_2\text{Ba}_2\text{Ca}_2\text{Cu}_3\text{O}_{10}$ systems, show still higher T_c . The main classes of ceramic superconductors with $T_c > 90$ K are compiled in Table 15.4. In accordance with their stoichiometry, Bi- and Tl-based HTS are named as 2212 and 2223 systems, respectively.

Similar to 123 systems, 2212 and 2223 systems too have a layered structure along the substantially larger c -axis. This layered structure is again considered to play a crucial role in the mechanism of superconductivity. The unit cell shown in Fig. 15.26(b) has two distinct regions, separated by two Bi-O (or Tl-O) planes. In the upper-half region, the copper atoms are located at centres while in the lower-half region they are at corners of the Cu-O planes. The T_c value is strongly controlled by the

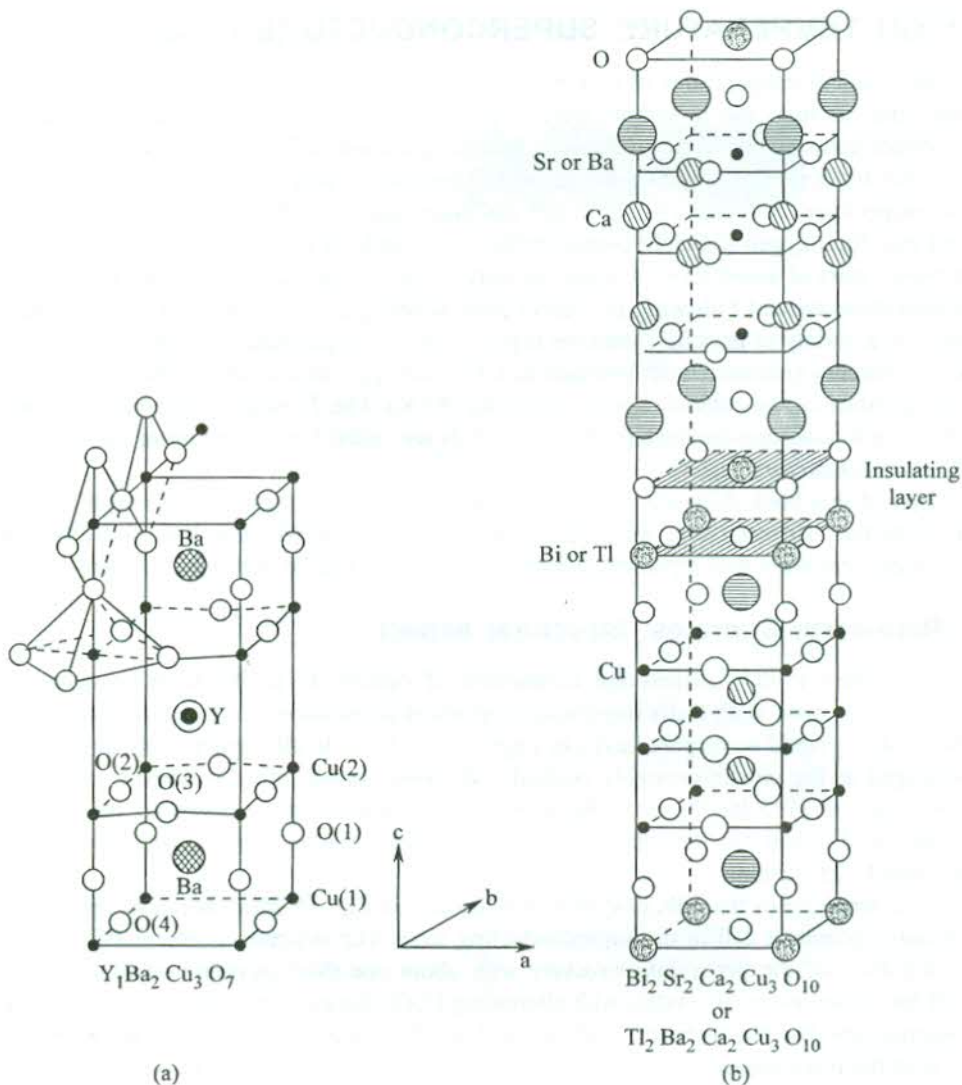


FIG. 15.26 (a) Unit cell structure of a $\text{Y}_1\text{Ba}_2\text{Cu}_3\text{O}_7$ crystal. The numbers in brackets represent the special sites of oxygen and copper atoms in CuO_2 layers. (b) Unit cell structure of $\text{Bi}_2\text{Sr}_2\text{Ca}_2\text{Cu}_3\text{O}_{10}$ or $\text{Tl}_2\text{Ba}_2\text{Ca}_2\text{Cu}_3\text{O}_{10}$ crystal.

number of CuO_2 layers in the unit cell. These ceramics differ from one another only in the number of CuO_2 layers per unit cell.

15.8.3 Significant Properties of Cuprate HTS

Consider the example of YBCO which is the most thoroughly researched system. Its resistivity around 90 K falls most sharply to an immeasurable value for $x = 0 - 0.1$, where x denotes oxygen deficiency. On increasing x , the transition temperature decreases. For $x > 0.7$, YBCO ceramics cease to be superconductors and behave as antiferromagnetic insulators. On account of their strongly anisotropic

Table 15.4 Prominent families of high temperature superconductors with highest T_c values reached. [After R. Hott, G. Rietschel, M. Sander; *Phys. Bl.*, **48**, 355 (1992).]

Formula	Short name	Highest T_c observed (K)
$\text{REBa}_2\text{Cu}_3\text{O}_7$ (RE = Rare Earths) = Y, Eu, Gd, ...)	RE BCO or 123	92 (YBCO)
$\text{Bi}_2\text{Sr}_2\text{Ca}_{n-1}\text{Cu}_n\text{O}_{2n+4}$ (+ Pb doping)	BSCCO or Bi-22 (n - 1)n	90 (Bi-2212) 122 (Bi-2223)
$\text{Tl}_2\text{Ba}_2\text{Ca}_{n-1}\text{Cu}_n\text{O}_{2n+4}$	TBCCO or Tl-22 (n - 1)n	110 (Tl-2212) 127 (Tl-2223)
$\text{Tl}_2\text{Ba}_2\text{Ca}_{n-1}\text{Cu}_n\text{O}_{2n+3}$ (A = Sr, Ba)	Tl-12 (n - 1)n	90 (Tl-1212) 122 (Tl-1223) 122 (Tl-1234) 110 (Tl-1245)
$\text{HgBa}_2\text{Ca}_{n-1}\text{Cu}_n\text{O}_{2n+2}$	Hg-12 (n - 1)n	128 (Hg-1212) 135 (Hg-1223)

* approaches 165 K under pressure.

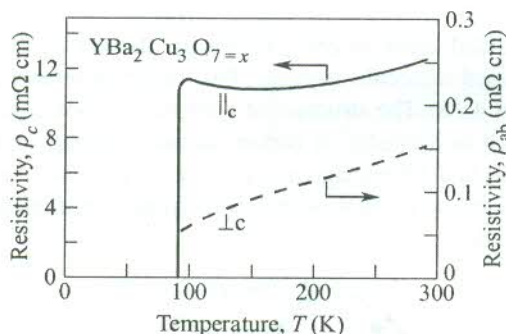


FIG. 15.27 Measured resistivity of YBCO along and perpendicular to the c -axis (ρ_a and ρ_{ab} respectively) as a function of temperature. [After S.J. Hagen, T.W. Jing, Z.Z. Wang, J. Horvath, N.P. Ong, *Phys. Rev.*, **B37**, 7928 (1988).]

crystal structure, the ceramic superconductors show highly anisotropic electronic properties. There is a large difference in the resistivities of YBCO, measured along and perpendicular to the c -axis (ρ_c and ρ_{ab} in Fig. 15.27). All the ceramic superconductors known to date show type II superconductivity for which B_{c1} is usually less than 10 mT and the largest estimates of B_{c2} are around 340 T.

A few extraordinary features of these HTS that might provide clue to the mechanism of superconductivity are as under:

1. The resistivity in the normal state varies linearly with temperature.
2. A near zero oxygen isotope effect is observed ($\alpha \sim 0-0.2$). The vanishingly small isotope effect is considered an important evidence for non-phononic superconductivity in cuprates.

3. The observed energy gaps are large, nearly 20–30 meV, and $\frac{\Delta(0)}{k_B T_c} = 3$ to 4, which is appreciably greater than the BCS estimate equalling 1.764.
4. The thermoelectric power shows a universal behaviour as a function of hole concentration.
5. The Hall coefficient is temperature dependent.
6. An inverted parabolic relation between T_c and the hole concentration is observed.

From the data on Hall coefficient it is inferred that a Cooper pair in YBCO type and Bi- and Tl-based superconductors is a pair of holes resulting in the *p*-type superconductivity in these materials. Because of their high electronegativity, oxygen atoms act as electron acceptors. For example, in YBCO, both Y and Ba ions contribute two electrons separately to the bonding in CuO₂ layers where the oxygen atoms trap these electrons. For small x (i.e. for a less oxygen-deficient composition), there are enough oxygen atoms to swallow the electrons. This way more holes are made available in the CuO₂ planes to get bound into hole Cooper pairs. These observations point to a quasi two-dimensional charge transport in CuO₂ planes by means of holes bound in Cooper pairs. These ideas are also applicable to the Bi and Tl superconductors. Although most of the cuprates show *p*-type superconductivity, there exist a couple of systems, namely Nd₂CuO₄ and Nd_{2-x}Ce_xCuO₄ in which the conventional *n*-type superconductivity has been confirmed.

15.8.4 Fullerenes

The novel superconductors added most recently (1991) to the list of HTS are fullerenes whose prominent members are C₆₀-based molecular crystals. The transition temperatures of materials of this class range from 15 K to about 48 K. The structure of a single C₆₀ molecule, as shown in Fig. 15.28, consists of 60 carbon atoms. It is a cluster of carbon atoms arranged in the shape of a truncated icosahedron with 20 hexagonal and 12 pentagonal faces (as in graphite, benzene and other organic molecules). The pentagons occur on account of the topological requirement for producing a closed structure that resembles a football.

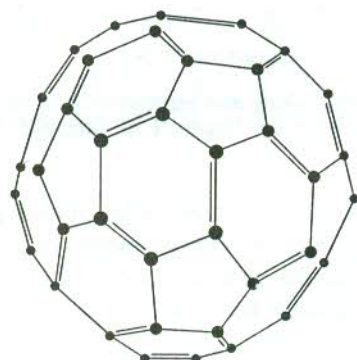


FIG. 15.28 The structure of a C₆₀-molecule.

The C₆₀ clusters form the basis for a three-dimensional crystal structure of C₆₀ which is characterized by an FCC unit cell. Some other interesting fullerenes have been derived from C₆₀ by crystallizing C₆₀ along with alkali metals whose atoms are placed in gaps between the C₆₀ spheres. These are found to show superconductivity with values of T_c that justify to put them in the category of HTS. A list of such fullerenes with their T_c values is given as follows:

<i>Fullerene</i>	T_c (K)
K_3C_{60}	19.3
Rb_3C_{60}	28
$RbCs_2C_{60}$	33
$Rb_{2.7}Tl_{0.2}C_{60}$	48

Similar to ceramic HTS, fullerenes demonstrate the gradual onset of diamagnetism when cooled in zero magnetic field to temperatures below T_c . It has not been possible so far to carry out other experiments on fullerenes on account of their strong tendency to react with atmospheric oxygen.

Despite the availability of quality data of enormous volume and getting an exclusive attention of the entire community of solid state physicists, the theory of HTS continues to be in an uncertain shape. In view of this fact, it is appropriate to dispense with the theoretical treatment of HTS in this introductory version of the subject.

15.9 APPLICATIONS

Superconductors have tremendous potential for application. It is extremely advantageous to use them as conductors of electric current because of their nondissipative property. Applications are mostly based on conventional (liquid helium) superconductors. Although they have already found numerous applications, their utilization has been much restricted by the requirement of extremely low temperatures. It is not possible to give here a complete list of applications. The main applications are: high field magnets, SQUIDS, and some other electronic and rf devices. The NMR imaging technique employing high magnetic fields has proved far superior to CATSCAN used in medical diagnostics. High Q-cavities and various sensors are some other important devices where superconductors are used. In addition to being employed in SQUIDS, there are a large number of applications of Josephson junctions in electronic circuitry.

In view of their higher T_c , the use of HTS in a much larger number of applications seems imminent. With considerable advancement in the methods of sample preparation (e.g. laser ablation, MOCVD, etc.), good quality wires, tapes and films of cuprates have been produced. But the low critical current and ceramic nature of HTS have seriously limited their applications. The degree of success achieved has been highest with the YBCO system, which is utilized for the fabrication of Josephson junctions and SQUIDS. With revolutionary advancement in material research, a very large number of applications spread over different areas can be realized. A high speed (~ 550 km per hour) levitating train has been tested using a conventional superconductor. But these levitating vehicles and long distance non-dissipative power transmission systems have yet to be realized in practice.

SUMMARY

1. The dc resistance of a superconductor is zero.
2. The Meissner effect ($B = 0$) is complete in bulk metallic samples in the superconducting state. The London penetration depth λ_L gives the extent over which the magnetic flux penetrates from the surface of a superconductor.

3. The London equation

$$\text{curl } \mathbf{j}_s = - \frac{n_s e^2}{m} \mathbf{B}$$

leads to the equation

$$\nabla^2 \mathbf{B} = \frac{1}{\lambda_L^2} \mathbf{B}, \text{ which interprets the Meissner effect with } \lambda_L = \left(\frac{m}{\mu_0 n_s e^2} \right)^{1/2}$$

4. The application of magnetic field B_c (the critical field) destroys superconductivity. The B_c at any temperature T is given by the empirical rule,

$$B_c(T) = B_c(0) \left[1 - \left(\frac{T}{T_c} \right)^2 \right]$$

5. For a type I superconductor, there is a single critical field B_c for which the superconductivity is lost. There are some type II superconductors in which at a lower field B_{c1} , the magnetic flux begins to penetrate (Meissner effect is only partial). At a much higher field B_{c2} , there is no Meissner effect; the field penetration is complete and the superconductivity is destroyed. The thermodynamic critical field B_c is in between B_{c2} and B_{c1} ($B_{c1} < B_c < B_{c2}$).
6. The difference between Gibbs free energies per unit volume of the normal and superconducting states of a superconductor is

$$G_n(T) - G_s(T) = \frac{B_c^2}{2 \mu_0}$$

7. The specific heat of a superconductor is

$$C_V^s = A \exp \left(- \frac{\Delta}{k_B T} \right) + \alpha T^3$$

where 2Δ is the energy gap.

8. Isotope effect: $T_c M^\alpha = \text{constant}$, where $\alpha \approx 0.5$.
9. In the superconducting state the current carriers are Cooper pairs, i.e. electron pairs. In a Cooper pair the wavevector and spin of the two electrons are represented as $(\mathbf{k}\uparrow, -\mathbf{k}\downarrow)$.
10. In a superconductor, the magnetic flux is quantized in units of $h/2e$.
11. For a type II superconductor

$$B_{c2} \approx \kappa B_c \quad \text{and} \quad (B_{c2} B_{c1})^{1/2} = B_c$$

$$B_{c1} = \frac{B_c}{\kappa} \quad \text{where } \kappa \text{ is the Ginzburg-Landau parameter.}$$

12. The SQUID (Superconducting Quantum Interference Device) is an extremely sensitive magnetometer.

PROBLEMS

- 15.1** Show that, because of field penetration, the critical field of a superconducting slab of thickness t is of the order of $B_c \left(1 + \frac{\lambda}{t}\right)$, where B_c is the critical field for the bulk sample. (Assume that the free energy difference between the normal and the superconducting states is independent of the specimen size.)
- 15.2** A thin superconducting ring of inner diameter 1 cm has 10 flux quanta trapped in its central hole. Estimate the value of the persistent current, assuming the penetration depth as 50 nm. [The self-inductance of a loop of radius R made of wire of cross-sectional radius r is, $\mu_0 R \ln(8R/r)$ henry (for $R \gg r$)].
- 15.3** Show that the destruction of superconductivity by applying a magnetic field produces cooling. Calculate the final temperature of a tin sample, first thermally isolated at 2 K and then placed under a magnetic field that exceeds the critical field value. [Neglect latent heat and take $C_n = \gamma T$ with $\gamma = 1.75 \times 10^{-3}$ J mole⁻¹ K⁻²].
- 15.4** Taking the critical magnetic field for aluminium as 105 gauss at absolute zero, calculate its stabilization energy density at absolute zero. Calculate the heat capacity discontinuity for a unit volume of an aluminium specimen at the critical temperature T_c .
- 15.5** Calculate the power dissipation in 1 km of a superconducting Nb cable, 10 mm in diameter, maintained at 8 K when it is carrying a current of 1000 A at 50 Hz. Assume that the cable is in a perfect superconducting state. (For Nb, electrical resistivity = 3×10^{-9} ohm m, $T_c = 9.5$ K, $\lambda = 47$ nm).
- 15.6** The penetration depth of mercury at 3.5 K is about 750 Å. Calculate (a) the penetration depth and (b) the superconducting electron density as the temperature tends to absolute zero.
- 15.7** The BCS gap of lead at 4 K is about 2 meV. Calculate the frequency of the tunnel current in a lead Josephson junction when it is biased with a voltage equal to one half of the gap potential. Calculate the gap energy at 4.2 K to two significant figures.
- 15.8** When the current through a superconducting solenoid immersed in liquid helium is increased slowly to 40 A, the solenoid becomes a normal conductor. If the solenoid is 15 cm long with a mean diameter of 3 cm and has 2000 turns, calculate the volume of the liquid that is evaporated in the process.
(Latent heat of helium = 2.5 J cm⁻³)
- 15.9** How is the current started in a superconducting magnet? Suppose a large superconducting solenoid magnet is below T_c . What would happen if a small hearing aid battery is connected across the solenoid? What will be the result if a large car battery were used?
- 15.10** When a current I passes through a cylindrical superconducting wire of radius r , the magnetic field produced immediately outside the wire is B_c . If the current is measured in A, radius in cm and the field in gauss, show that
- $$I = 5rB_c$$
- 15.11** Consider a superconducting plate perpendicular to the x -axis and of thickness d placed in a region of an externally imposed magnetic field \mathbf{B} . If the penetration of field inside the plate

is described by $\nabla^2 \mathbf{B} = \frac{\mathbf{B}}{\lambda}$, show that the magnetic field at any point x inside the plate can be expressed as

$$B(x) = B_0 \frac{\cosh(x/\lambda)}{\cosh(d/2\lambda)}$$

where the centre of the plate is at $x = 0$ and λ denotes the penetration depth. Show that the effective magnetization $\mathbf{M}(x)$ in the plate is given by

$$\begin{aligned}\mu_0 \mathbf{M}(x) &= \mathbf{B}(x) - \mathbf{B}_0 \\ &= - \frac{\mathbf{B}_0 (d^2 - 4x^2)}{8d^2}\end{aligned}$$

provided $d \ll \lambda$.

- 15.12** A Josephson junction of rectangular cross-section and of thickness d is placed in the region of a magnetic field B_0 , applied normal to an edge of width b . If the phase difference between the two superconductors be $\pi/2$ when $B_0 = 0$, prove that the dc current in the presence of the field is given by

$$I = I_0 \frac{\sin(bdB_0 e/\hbar)}{bdB_0 e/\hbar}$$

SUGGESTED FURTHER READING

- Aschroft, N.W. and N.D. Mermin, *Solid State Physics* (Saunders College, 1988).
 Burns, G., *High-Temperature Superconductivity* (Academic, 1991).
 Ibach, H. and H. Lüth, *Solid State Physics* (Springer, 1995).
 Ramakrishnan, T.V. and C.N.R. Rao, *Superconductivity Today* (Wiley Eastern, 1992).
 Schrieffer, J.R., *Theory of Superconductivity* (Benjamin/Cummings, 1983).
 Tinkham, M., *Introduction to Superconductivity* (Krieger, 1980).

Nanomaterials

16.1 INTRODUCTION

Materials with at least one of the dimensions measuring less than 100 nm ($1 \text{ nm} = 10^{-9} \text{ m}$) are known as nanomaterials. Alternatively, we define nanomaterials as those which have a characteristic length scale within about 100 nm. A particle diameter, grain size, layer thickness, or width of a conducting line on a device are some examples of length scale. Examples of some common nanostructures with their approximate sizes are listed in Table 16.1. The properties of bulk materials are mostly retained till the reduction of their dimensions to the micrometre range. But materials in the nanometre scale may show remarkably new properties. For example, a nanocrystal of gold serves as an excellent low temperature catalyst whereas the bulk gold does not. Bulk semiconductors transform into insulators if their dimensions shrink to a couple of nanometres. The melting temperature of crystals in the nanometre scale is very low, lower by 1000°C in some cases. The lattice constants are, too, reduced. The role of surface energy in thermal stability assumes a great significance, because in this scale the number of atoms or ions occupying the surface turns out to be a big fraction of the total number of atoms or ions. The crystalline order that is stable at a high temperature in bulk stabilizes at a much lower temperature in the respective nanomaterial. As a result, the properties such as ferroelectricity

Table 16.1 Examples of some common nanostructures with their approximate sizes*†

<i>Nanoparticle</i>	<i>Size (nm)</i>	<i>Nanoparticle</i>	<i>Size (nm)</i>
Gas ion salts	0.1–1	Paint pigment	$10^2\text{--}5 \times 10^3$
Sugars	~ 1	Pet dander	$10^3\text{--}5 \times 10^3$
Quantum dot	1–5	Red blood cells	$\sim 10^4$
Micelles	1–10	Microparticle	$10^3\text{--}10^4$
Pyrogens	1–15	Bacteria	$5 \times 10^2\text{--}5 \times 10^4$
Micromolecules	1–80	Yeast cells	$5 \times 10^3\text{--}5 \times 10^4$
Colloid silica	5–80	Pollens	$10^4\text{--}10^5$
Virus	10–100	Macroparticle	$10^4\text{--}10^5$
Cooking smoke	$10\text{--}10^3$	Sand	$\sim 10^5$
Macromolecules	$10^2\text{--}10^3$	Human hair	$10^4\text{--}10^5$
Clay	$10^2\text{--}10^3$		

* Microscopy and Histology Catalog, Polysciences, Washington, PA, 1993–1994

† N. Itoh, in Functional Thin Films and Functional Materials: New Concepts and Technologies, ed. D.L. Shi, Tsinghua Univ. Press and Springer-Verlag, Berlin, p.1 (2003).

and ferromagnetism may disappear when the dimensions of materials having these properties are cut down to fall in the nanometre scale. It should surprise none that a nanoscale wire or circuit component does not necessarily obey the venerable law of electricity, the Ohm's law.

With the realization of the characteristic properties of nanomaterials, not seen in bulk materials, a revolution in the growth of nanoscience and its technology has occurred. Nevertheless, the historical survey reveals that the existence of nanomaterials and functional devices based on them dates back to the inception of life itself. For example, the cells near the nose of trout fish are believed to possess a fluid of magnetic nanoparticles. The fish takes advantage of the feel of change in magnetization when it deviates from the direction of the Earth magnetic field. It changes its orientation according to need (say, for avoiding the enemy) under the guidance of brain that stores the information on the change of magnetization. Humans too started exploiting the properties of nanosized materials as early as the fourth century A.D. when Roman glass-makers fabricated the classic Lycurgus cup, named after a king and now displayed in the British Museum in London. The cup contains nanosized metal particles and changes its colour from green to deep red on shining its inner surface with light. Even though the results of initial human effort might not have been always fortuitous, there is no denying the fact that the characteristic properties of nanoparticles remained less understood for a long time. The scenario was almost static for three decades even after the advent of quantum mechanics whose application has ultimately yielded all the exclusive information on nanomaterials. It was the brilliance and imagination of Richard Feynman that broke the ice in 1960 at a meeting* of the American Physical Society. Perhaps, in view of his reputation for jokes cracking the audience did not take him seriously when he stated that a cube of side 0.02 inch could store all the books ever written if the material of the cube were constructed by adding individual atoms with the use of a finely tuned technique. He gave the thought of electron beam lithography indirectly while professing for etching lines a few atoms wide with electron beam. Even then, the spin-off in the fabrication of nanostructures could occur only after two decades of this prediction, albeit a beginning made at Bell Labs and IBM in 1970. Feynman is known primarily for laying the foundations of quantum electrodynamics that fetched him Nobel Prize in the year 1965. His contribution of giving the concept of nanotechnology has too been suitably acknowledged by creating THE FEYNMAN PRIZE to recognize the achievements of nanoscientists.

The last two decades have seen a remarkable growth of knowledge in nanoscience and its applications. As a result of this buzzing activity, the nano has moved from the world of the future to the world of the present. It is exemplified by the arrival of computers that compute algorithms to mimic human brain, biosensors that detect the onset of disease and traject drugs attacking the diseased cells on site, and nanorobots capable of repairing internal damages in our body and extricating chemical toxins. These simple-to-use devices successfully detect even the dangerous biotoxins such as anthrax. Other fascinating achievements of nanotechnology include the development of new superconductors with higher transition temperatures and the emergence of nanoelectronics. The latter has led to a drastic miniaturization of devices and is being used to constantly monitor our environment. On popular commercial front, nano skin creams and scented lotions are already in the market whereas tennis balls with nanoenhanced bounce arrived at the 2002 Davis Cup. The wide range of these applications unambiguously shows that the current advanced form of nanotechnology is essentially the outcome of an intense interdisciplinary and multi-disciplinary effort. A coordination of so many wide-ranging disciplines is not known in the history of science and technology. With such a united force behind to propel it, nanotechnology holds the

* R.P. Feynman, *Eng. Sci.* **23**, 22 (1960).

promise to produce unforeseen commercially viable technology and satisfy the everlasting human curiosity at the same time.

16.2 NANOPARTICLES

A group of 10^6 or less number of atoms or molecules bonded together in a cluster with the radius of about 100 nm (1000 Å) or less forms a nanoparticle. The role of the small colloidal particles of silver in image formation on a photographic film is common knowledge. The presence of silver and gold nanoparticles in the material of Lycrus cup, referred earlier, accounts for the change in its colour on shining its inner surface with light. The metal oxide nanoparticles of different sizes in stained glass windows produce different beautiful colours because a particle scatters only that wavelength which compares with its size. This goes on to corroborate the observation that nanoparticles show unique properties when their size is smaller than certain critical lengths corresponding to respective physical phenomena. To quote an example, the electron mean free path that strongly controls the electrical conductivity of a metal is a critical length.

The understanding of structure and properties of nanoparticles is crucial for the interpretation of the characteristic phenomena exhibited by them. A brief description of some well-studied nanoparticles is given below.

16.2.1 Metal Nanoclusters

The procedure of making the clusters of metal atoms is demonstrated in Fig. 16.1. The metal surface is melted and the atoms evaporated by making a high power laser beam fall on the metal surface. A burst of helium gas is used to carry the evaporated atoms through a narrow opening into an evacuated chamber where the vapour of atoms expands and cools to form clusters. A mass spectrometric study of these clusters is carried out to determine their stability in terms of the number of atoms contained in a cluster. For this purpose, the clusters are first ionized by exposing them to a UV radiation and then pushed into a mass spectrometer. The data reveal that the number of ions (counts) is large for certain numbers of atoms in a cluster. These numbers indicate the number of

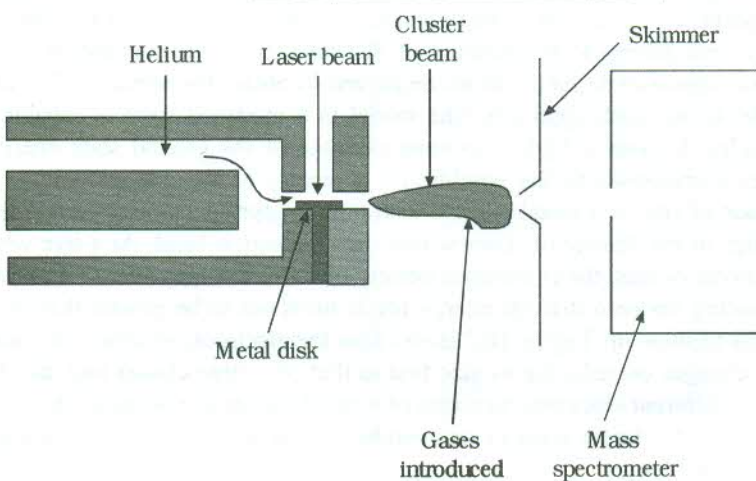


FIG. 16.1 Illustration of the experimental set-up for making metal clusters. (Reprinted from *Introduction to Nanotechnology*, C.P. Poole, Jr., and F.J. Owens, John Wiley, 2003, with permission from John Wiley).

atoms that combine to form a stable cluster. The atoms combine in different numbers to produce stable clusters of different sizes. These different numbers are called *magic numbers*. The magic numbers result mostly from the enhanced stability of closed-shell electronic configurations. In rare gas clusters the magic number arises from geometric effect.

There exist two well-known theoretical models to calculate the properties of clusters: the jellium model and the density functional model (based on the molecular orbital theory). In jellium model the clusters are viewed as superatoms. A sphere approximates the size and the shape of a certain cluster and the positive nuclear charge of each atom of the cluster is considered to be uniformly distributed over the sphere. The interaction between the electron and the positive spherical charge distribution is denoted by a spherically symmetric potential. The solution of Schrödinger equation yields a different order of energy levels for clusters as compared to that for the hydrogen atom. The electronic magic numbers (the total number of electrons in a superatom) correspond to those cluster sizes where all the energy levels are completely occupied.

In the other model the electronic wavefunction for the cluster is constructed on the principles of molecular orbital theory. The simplest of clusters, one could think of, is a molecule such as H_2^+ because the Schrödinger equation can be solved exactly for a hydrogen atom. The ground state wavefunction of the hydrogen atom is expressed as

$$\Psi_{1s}(\mathbf{r}) = Ae^{-\mathbf{r}/a_0} \quad (16.1)$$

where \mathbf{r} gives the position of the electron, relative to that of the nucleus and a_0 is the Bohr radius.

The wavefunction of the electron in molecule is taken as a linear combination of the ground state wavefunctions (16.1) of the two individual H atoms. The problem now reduces to solving the Schrödinger equation using the Hamiltonian

$$\mathcal{H} = \left(-\frac{\hbar^2}{2m} \nabla^2 - \frac{e^2}{r_a} - \frac{e^2}{r_b} \right) \quad (16.2)$$

where r_a and r_b are the distances of the electron from the two nuclei 'a' and 'b'.

The Schrödinger equation with the above Hamiltonian is solved to calculate the actual electronic and geometric structures of small clusters. As the cluster size grows, the exercise assumes a complex shape and getting to the solution of Schrödinger equation ceases to be straightforward. However, several approximate methods are employed to obtain the solution. The use of the density functional model is one such approach. The model in a modified form is capable of dealing with metal nanoparticles. It gives a highly accurate estimate of the ground state energy. The structure with this energy corresponds to the equilibrium geometry of the nanoparticle.

The reduction of size of a metal particle with bulk properties below a certain level brings about a dramatic change in the density of states within the conduction band. At a size when a particle has a few hundred atoms or less, the continuous density of states changes over to a set of discrete energy levels. If the spacing between discrete energy levels turns out to be greater than the thermal energy $k_B T$, a gap begins to show up. Figure 16.2 shows how the electronic structure of a metal particle with bulk properties changes on reducing its size first to that of a large cluster and then to one of a small cluster. Radically different electronic structure of a small cluster is essentially the quantum size effect that can be observed for larger sizes in semiconductors on account of the wavelength of carriers in semiconductors being longer.

Barring small changes in lattice parameters, there is generally no difference in the crystal structure of a large nanoparticle and that of its bulk. But particles having diameters less than 5 nm may have

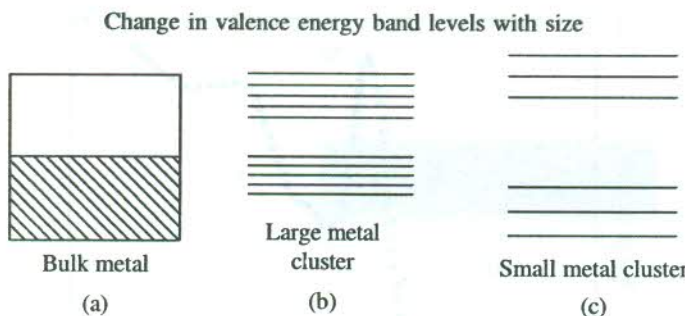


FIG. 16.2 Effect of reducing the number of atoms in a metal sample on the distribution of the valence band energy levels. The bulk sample (a) does not show the gap; in a large cluster (b) containing 100 atoms, the gap becomes distinct and it grows further for a small cluster (c) composed of only three atoms.

a different crystal structure. For example, gold particles of 3–5 nm sizes are shown to have an icosahedral structure and not the bulk FCC structure. Additionally, a high catalytic is switched on in gold nanoparticles as they approach less than 3 to 5 nm size. However, the size at which the transition to bulk behaviour occurs seems to vary according to the property under study.

Also, the evidence for the magnetic behaviour of nanoparticles is well documented. But the observation of a net magnetic moment in clusters comprised of non-magnetic atoms is, perhaps, one of the most remarkable properties of nanoparticles. As the number of atoms in a cluster falls below 20, there occurs a pronounced enhancement in the magnetic moment of these clusters.

16.2.2 Semiconductor Nanoparticles

Here, we refer to nanoparticles that are made of the normal constituents of semiconductors. The constituents are semiconducting elements (Si, Ge, etc.) or the semiconducting compounds (GaAs, CdSe, etc.). The nanoparticles themselves may not behave as semiconductors as is exemplified by the behaviour of the nanoparticles of Ge, Si and Cd. The method of synthesis used for metal nanoparticles works equally well for these particles.

The optical properties of these particles are most interesting. The properties undergo a remarkable change as the transition from bulk to nanoscale occurs. The excitation of excitons strongly modifies the absorption spectra of these particles. When the particle radius is larger than the exciton size, with the exciton motion confined to a limited range, a blue shift (shift towards higher energies) in the spectrum occurs. On the other hand, when the particle size is smaller than the orbital radius of the electron-hole pair, the electron-hole coupling vanishes and the exciton exists no more, releasing the electron and the hole for independent movement. Because the electron and the hole have separate schemes of energy levels, new lines appear in the absorption spectrum, showing again a blue shift. The optical absorption spectra of CdSe nanoparticles recorded at 10 K for two particle sizes are shown in Fig. 16.3. For the smaller particle, we observe that the absorption is more intense and the absorption edge is blue shifted, which is the indication of a larger band gap in this particle. The spectra also reflect the effects of the confinement of exciton. The exciton lines being represented by peaks at higher energies shift towards further higher energies on reducing the particle size. In a particle of smaller size, the electron and the hole are drawn closer and the energy level separations change.

The nanoparticles of Ge and Si are found to undergo fragmentation on being irradiated with a Q-switched Nd-YAG laser light. For example, a Si_{12} particle breaks into two Si_6 particles. The emerging products depend on the cluster size, the wavelength and the intensity of laser beam. A

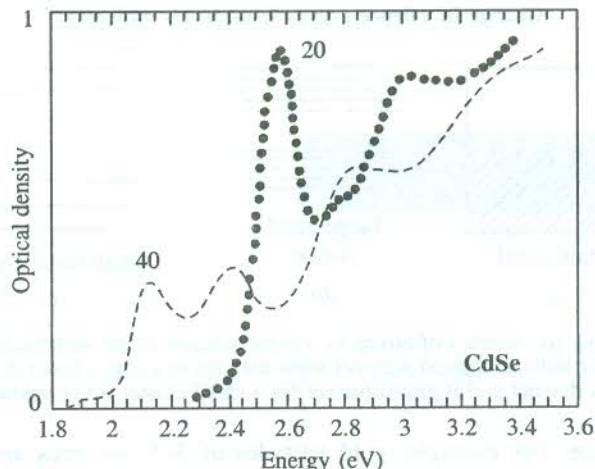


FIG. 16.3 Size effect on the optical absorption spectrum of CdSe at 10 K. The figure shows the spectra for two nanoparticles (sizes: 20 Å, 40 Å) [Reproduced from D.M. Mittleman, *Phys. Rev.*, **B49**, 14435 (1994)].

cluster with more than 30 atoms tends to fission explosively. This is most likely to happen in multiply ionized clusters where each atom gets the positive charge through the quick redistribution of charges on the atoms following the process of ionization. When the Coulombic repulsion between the atoms in a cluster grows beyond the binding energy between the atoms, the cluster explodes and the atoms fly apart with great velocities. The phenomenon is popularly identified as ‘Coulombic explosion’.

16.2.3 Other Nanoparticles

Nanoparticles can be formed from rare gases and molecules such as water and carbon dioxide. Some of these are stable even in multiply charged form. Examples of such largest clusters are: $(Kr_{73})^{2+}$, $(Xe_{206})^{4+}$ and $(CO_2)_{216}^{4+}$. Water is comprised mostly of its molecular clusters where the hydrogen atom of one molecule bonds with the oxygen atom of another molecule, such that the hydrogen atom is not equidistant from the two oxygen atoms. Under normal conditions about 80% of water molecules are clustered.

Nanoparticles are also known to show some unusual properties such as superfluidity. It has been observed in He clusters with 64 and 128 atoms. In the state of Bose–Einstein condensation (the state where all the bosons occupy the lowest energy level), the liquid He^4 at 2.2 K becomes a superfluid, losing its viscous property completely.

16.3 NANOSTRUCTURES

16.3.1 Carbon Clusters

In 1985, Kroto and Smalley with their collaborators recorded mass spectra of laser ablated graphite that showed several intense lines corresponding to the clusters of different sizes. Calculations on small clusters based on the density functional theory demonstrated that the clusters form in linear or closed non-planar monocyclic structures. The linear clusters have sp hybridization with carbon

bond angle as 180° . These clusters contain an odd number of atoms and those with 3, 11, 15, 19 and 23 are more stable as reflected by the large intensity of respective lines in the mass spectrum (Fig. 16.4). The two other forms of hybridization occurring in carbon molecules are sp^2 and sp^3 , with carbon bond angles measuring 120° and $109^\circ 28'$ respectively. Clusters with closed structures contain an even number of atoms and the carbon bond angles are different from the three standard hybridization values given above. One such cluster composed of 60 atoms is found to show the highest intensity in the mass spectrum and hence the most stable. The evidence for the existence of this molecule was first found while measuring the intensity of light coming from stars at different wavelengths. A pronounced reduction in the intensity of light at 220 nm falling on Earth was detected. The phenomenon referred to as 'optical extinction' was attributed to scattering by small graphite particles believed to be present in the interstellar dust filling the regions of the outer space between stars and galaxies. The IR studies involving the use of graphite arcs were carried out for further clarification and confirmation. Huffman and Kratschmer observed four IR lines that correspond closely to the lines of a molecule C_{60} , predicted theoretically to exist several years earlier. Other investigations using techniques including the mass spectrometry were then made that led to the confirmation of the existence of C_{60} molecule in 1990.

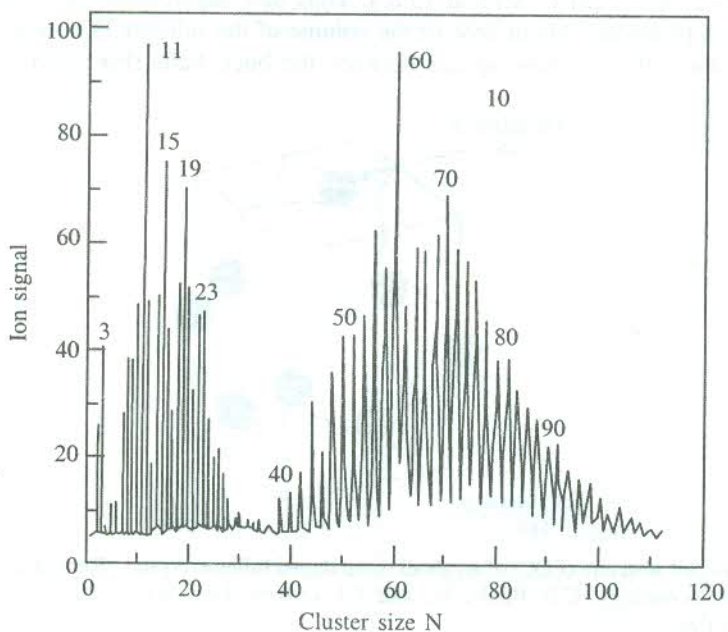


FIG. 16.4 A mass spectrogram of carbon clusters (Reproduced from *Microcluster Physics*, S. Sugano and H. Koizumi, Springer-Verlag, 1998 with permission from Springer).

On the basis of the analysis of their mass spectrum, the team of Kroto, Smalley and collaborators proposed a soccer ball shape and the icosahedral symmetry for C_{60} molecule. According to this model, the three-fold coordinated carbon atoms are bonded to form a spherical surface composed of 12 pentagons and 20 hexagons. The formation of pentagons lends the otherwise graphite sheet bend into a closed surface having no dangling bonds. It resembles geodesic domes whose structure was studied by the American architect Buckminster Fuller. In view of this similarity, the C_{60} molecule was named 'Buckminsterfullerene'. The similarity of its geometric configuration with that of a soccer

ball forms the basis for its familiar name ‘Buckyball’. The C_{60} molecule shows a single line C^{13} NMR spectrum which strongly confirms the buckyball model. Simply, because the mass spectra showed the evidence for many other even-numbered carbon clusters as well (e.g. C_{70}), the general name ‘fullerenes’ has been adopted to represent the group of these cage-shaped carbon clusters.

The structure of C_{60} molecule (the buckyball) is shown in Fig. 15.28. Crystalline C_{60} is formed from an ordered array of the tightly bound buckyballs, which are bound together by weak van der Waals forces. The crystals have FCC symmetry and retain many of the molecular properties contrary to the behaviour of other crystalline forms of carbon: diamond and graphite. The buckyballs are highly resistant to photofragmentation and very resilient to collisions against surfaces. The mechanical properties of solid C_{60} (also called ‘fullerite’) are characterized light, weak and soft while comparing with other forms of carbon. The electronic energy bands show a slight broadening. The fullerite is dubbed as a large bandgap semiconductor. It does not absorb in the near IR and into the visible region where the thin films show orange colour due to the transitions near the bandgap energy (minimum 1.5 eV). In the powder form, the colour depends on the crystallite size and varies from grey to black.

The fullerite is a poor conductor of electricity. But it turns into a superconductor when doped with alkali metals as discussed in Section 15.8.4. Thus new superconductors with T_c in the range 20–50 K have been produced. About 26% of the volume of the fullerite FCC unit cell is empty and the alkali metal atoms fit into these spaces between the buckyballs (Fig. 16.5).

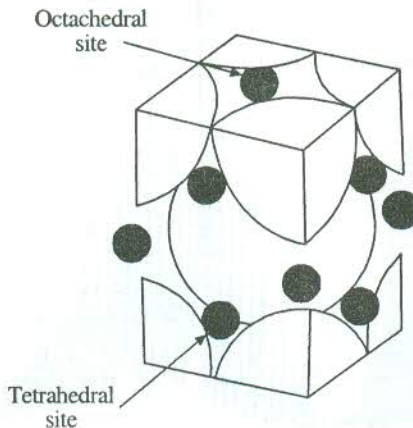


FIG. 16.5 The unit cell structure (FCC) of an alkali metal doped fullerite crystal. (Reproduced from *Introduction to Nanotechnology*, C.P. Poole, Jr., and F.J. Owens, John Wiley, 2003, with permission from John Wiley).

Till date, the fullerenes have not been applied on a large scale. Their biggest potential lies in their use as building blocks for synthesizing new diverse organic chemicals and solid materials. Some of the other projected applications are: photochromic goggles, xerographic materials, lubricants, sensors, ion rocket propulsion, diamond seeding, new semiconductors, patterned superconductors, patterned diamond films and anti-viral agents.

16.3.2 Carbon Nanotubes

Carbon nanotubes have the potential for wide-ranging applications due to their interesting properties. The nanotubes form generally as multiple-walled nanotubes (MWNT) whereas the single-

walled nanotubes (SWNT) are fabricated by mixing traces of some catalysts—cobalt, nickel or iron with the graphite target.

There are three well-known techniques of synthesizing carbon nanotubes: laser evaporation, carbon arc and chemical deposition method. The set-up used in evaporation method is sketched in Fig. 16.6. Argon gas and a graphite target is enclosed in a quartz tube. The tube is centred inside a horizontal furnace maintained at 1200°C with portions toward the ends falling outside the furnace. The target contains small amounts of cobalt and nickel that serve as the catalytic nucleation centres. Carbon atoms are evaporated from the graphite target with the help of an intense laser beam incident on the target. A water-cooled copper collector is mounted within the tube at one of its ends, lying outside the furnace. The large temperature difference between the middle and the end portions of the tube facilitates the argon gas to sweep the carbon atoms to the cold copper collector, resulting in the formation of nanotubes by condensation. The tubes are typically 10–20 nm in diameter and 100 μm long. This method as well as the carbon arc method produces tubes with closed ends. The chemical vapour deposition method, on the other hand, gives tubes with open ends.

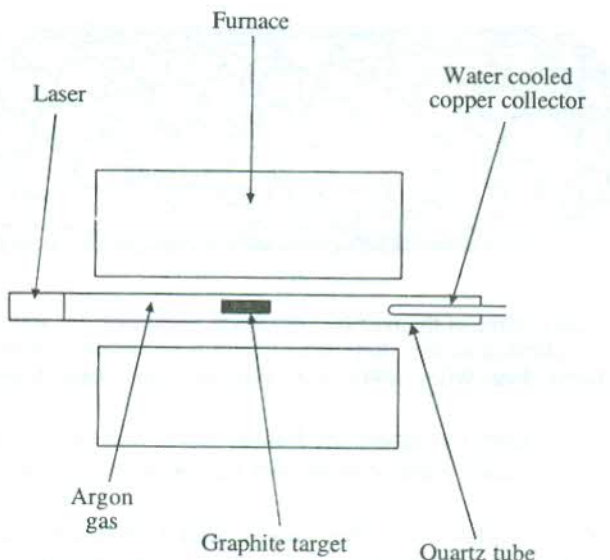


FIG. 16.6 Illustration of the laser evaporation method of synthesizing carbon nanotubes.

The carbon nanotubes are imagined to have been formed by rolling the graphite sheet the bonds at whose ends may join to close the tube. In the actual process of formation, however, no rolling of the sheet occurs. The above imagination only serves to explain various observed structures of nanotubes. The axis about which the graphite sheet is rolled is represented by the axis vector lying on the sheet plane. For example, three possible structures of carbon nanotubes are shown in Fig. 16.7. The structure shown in Fig. 16.7(a) (and referred to as the armchair structure) results when the axis vector is parallel to the C–C bonds of the carbon hexagons. The zigzag structure [Fig. 16.7(b)] and the chiral structure [Fig. 16.7(c)] are formed for two other orientations of the axis vector.

The molecular symmetry of carbon nanotubes classifies their vibrations into two normal modes denoted by A_{1g} and E_{2g} representations. A_{1g} mode represents the ‘in and out’ oscillations of the diameter of the tube. In the other normal mode (E_{2g}), the tube’s cross section oscillates between the

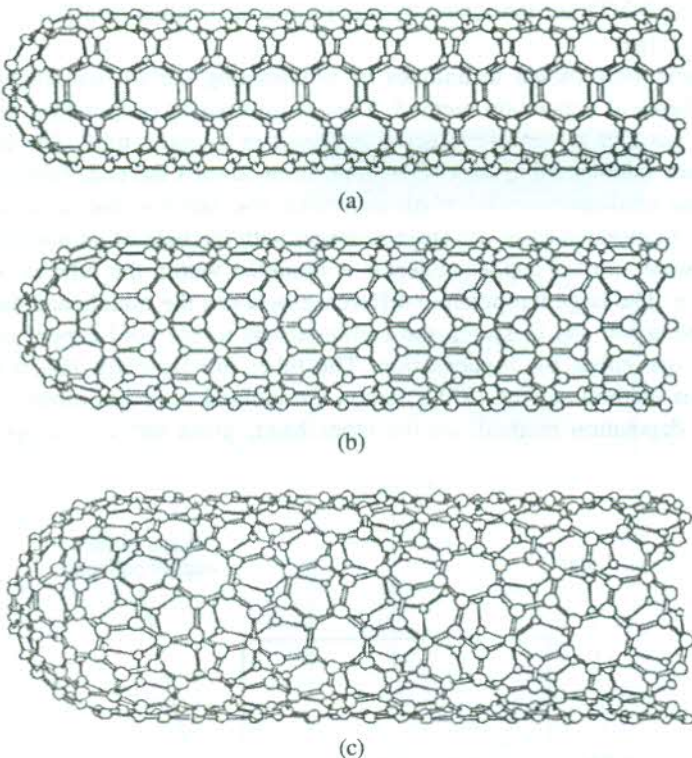


FIG. 16.7 Common structures (three of the possible) of carbon nanotubes: (a) armchair structure, (b) zigzag structure and (c) chiral structure. (Reproduced from *Introduction to Nanotechnology*, C.P. Poole, Jr. and F.J. Owens, John Wiley, 2003; with permission from John Wiley).

circular and elliptical shapes. Both the modes are Raman active and their frequency depends on the tube diameter. It is now a standard practice to exploit this property for measuring the diameter of carbon nanotubes.

The Young's modulus of carbon nanotubes ranges from 1.28 to 1.8 terapascal (one terapascal ($Tpa \approx 10^7$ atmospheric pressure), a value that is about 10 times that for steel. Thus carbon nanotubes are very stiff and resilient to bending. They buckle without breaking. Since their wall structure has a very low density of defects, they do not fracture when bent severely. The tensile strength is very high (about 45 billion pascals), making them about 20 times stronger than steel. The single-walled nanotubes are stronger than their multiple-walled counterparts.

Generally, carbon nanotubes form as a mixture of semiconducting and metallic tubes in the ratio 2:1. The diameter and the chirality of a tube determine the conducting behaviour of the tube. Chirality describes the manner in which the graphite sheet is rolled with respect to the axis vector. The metallic nanotubes have the armchair structure shown in Fig. 16.7(a). The bandgap of semiconducting chiral nanotubes decreases with increasing diameter. The electronic structure is studied using scanning tunnelling microscopy (STM). The data show that the electronic states split into one-dimensional sub-bands instead of forming a single wide band. The electronic states turn out to be the solutions of the Schrödinger equation where the length of the nanotube is taken as the depth of the involved potential well.

Individual single-walled nanotubes show interesting electronic transport. The voltage-current characteristics of a single metallic nanotube placed across two metal electrodes show step-like features which is similar to that of a field effect transistor (FET) constructed from a carbon nanotube. The metallic nanotubes can carry extremely high current with density approaching 10^9 A/cm^2 . The density of defects in carbon nanotubes is so low that the defects cannot cause electron localization and the electrons do not suffer much scattering from defects. This is the cause for high electrical conductivity of nanotubes. The current does not heat carbon nanotubes the same way as in copper, which fails at 10^6 A/cm^2 . Carbon nanotubes are also very good conductors of heat, the thermal conductivity being almost twice as large as that of diamond.

Carbon nanotubes are used to enhance the strength of plastic composites. They serve as good catalysts to speed up the rate of some chemical reactions. They are also applied in battery technology. The field-effect transistor made of chiral semiconducting nanotubes has proved to be a sensitive detector of many gases. Most of the challenging applications are in the fields of electronics and computers. Some have already been realized and several more are envisioned. For example, electrons are emitted at a high rate from the ends of a nanotube when a small electric field is applied along its axis. The effect, known as ‘field emission’, has contributed to the development of flat panel displays. Based on this effect, vacuum tube lamps are being made in Japan which are equally bright as the common light bulbs and have a higher efficiency and a longer life.

Very low resistance of carbon nanotubes makes them ideally suitable for use as interconnects and their high thermal conductivity for use as heat sinks for chips. The fabrication of field effect transistors from carbon nanotubes has raised vision for very fast computer switches. One of the major challenges of nanotubes has been physical assembly because they tend to stick to one another and do not exhibit the molecular recognition properties more generally associated with organic molecules. Elsewhere, the computer scientists are striving to increase the number of switches on a chip, pressing for large-scale production of thinner nanotubes. Methods for large-scale production of multiple-walled nanotubes are well developed. But those for single-walled nanotubes have very low yields, raising their cost exorbitantly. The application potential of carbon nanotubes can be truly realized with the development of methods for large-scale production of single-walled nanotubes, in view of their more remarkable features.

16.3.3 Quantum Nanostructures

Three limiting classes of nanostructures emerge on the basis whether only one, only two or all three dimensions fall in nanometre scale. When only one dimension is reduced to nanometre range and two remain large, we get the material called *quantum well*. If two dimensions are in nanometre range and one large, the structure is known as *quantum wire*. But if all three dimensions are made to be in nanorange, we refer it to as *quantum dot*. The rectangular and curvilinear quantum nanostructures are shown in Fig. 16.8. The word ‘quantum’ here signifies that the materials with these structures possess new physical properties or exhibit new physical phenomena which their bulk counterparts do not. As such, the word quantum draws parallel to getting new results with the use of quantum mechanics in situations involving small (quantum) numbers and small (physical) quantities.

There are two approaches to the synthesis of nanomaterials and the fabrication of nanostructures: bottom-up and top-down. The bottom-up approach generally uses a sequence of catalysts controlled chemical reactions. The procedure involves the collection of individual atoms and molecules and making them condense into a specific pattern or structure. The top-down approach employs the opposite method where the size of a large-scale object or pattern is reduced gradually.

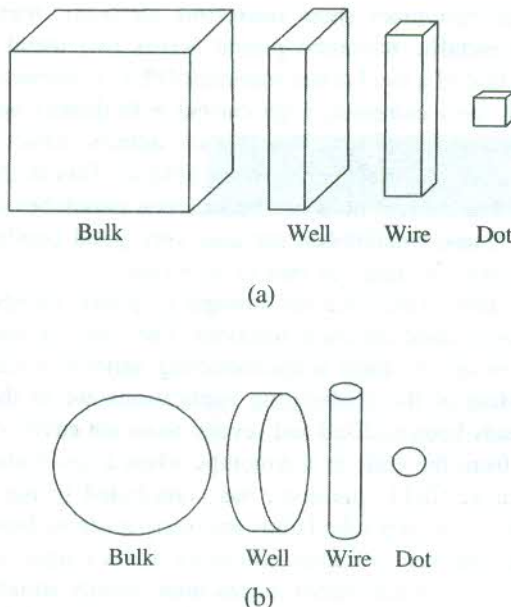


FIG. 16.8 Formation of (a) rectangular and (b) curvilinear quantum structure by progressive reduction in size.

The colloidal dispersion is the simplest example of the bottom-up method whereas attrition or milling describes best the top-down approach to making nanoparticles. Though nanolithography and nanomanipulation are commonly taken as the bottom-up approach, the lithography should in fact be treated as a hybrid approach since the growth of thin film is bottom-up and the etching is top-down.

The quantum wires and quantum dots are fabricated by the attrition of a thin film (quantum well) of the sample material supported by its substrate. The procedure followed in the electron-beam lithography is illustrated in Fig. 16.9. In the first step, the sample quantum well is coated with a radiation-sensitive resist (e.g. polymethyl methacrylate). Then, the central region on the surface of the resist, under which some specific nanostructures is desired, is irradiated by an electron beam through a template. The irradiation transforms the resist material in this region chemically to a form that is soluble in a developer. The irradiated part of the resist is removed, using the developer. Next, an etching mask is planted into the groove or pit formed as a result of the removal of the resist. The remaining part of the resist is now taken out and the region of the quantum well uncovered by the etching mask is chemically etched away. The resulting structure is a quantum nanostructure which may be a quantum wire or a quantum dot, depending on the shape and the size of the groove. If required, the mask may be lifted. Figure 16.9 shows the fabrication of a quantum dot.

Quantum structures of more complex type have shown some remarkably improved properties, making them attractive for device fabrication. The lithographic technique has generally been used to get these structures. For example, a quantum dot array derived from a multiple quantum well structure produces a very enhanced photoluminescent output that is about hundred times greater than that of the initial multiple quantum wells. The property has been exploited in the fabrication of quantum dot lasers. The genesis of the remarkably different properties of quantum nanostructures lies in their drastically reduced dimensions. As the size on nanoscale reduces, the fraction of atoms on the surface of the nanocrystal grows larger and larger. Consequently, the number of conduction electrons

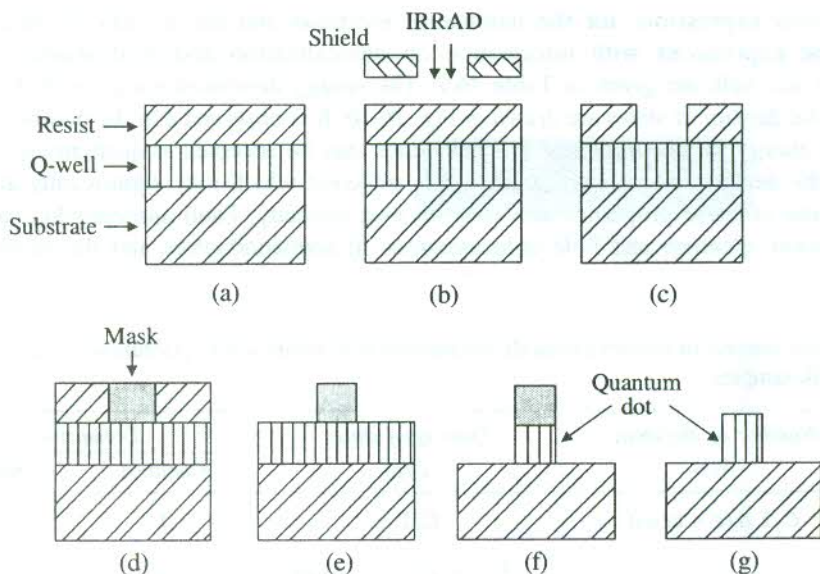


FIG. 16.9 Stages of formation of a quantum structure in electron-beam lithography: (a) a substrate supported quantum well, covered by a resist, (b) irradiation of the sample that is shielded by a template, (c) form after dissolving the irradiated portion of the resist, (d) placing the etching mask, (e) configuration after removing the unirradiated resist, (f) structure after etching away the undesired portion of the quantum well, (g) quantum dot structure on substrate obtained by removing the etching mask. (Reproduced from *Introduction to Nanotechnology*, C.P. Poole, Jr. and F.J. Owens, John Wiley, 2003; with permission John Wiley).

in metals and semiconductors drops considerably and the electron mean free path becomes size-dependent. When the diameters of microcrystallites are much larger than the mean free path, a network of interconnected resistors would be the appropriate representation for the resistivity of polycrystalline sample. But if the dimensions match the mean free path, the scattering from the boundaries between crystallites controls the resistivity in a big way.

It has been shown that an *n*-type semiconductor quantum dot cube of side 10 nm with 10^{18} donors per cm^3 will have only one conduction electron. Similar estimates have been made for quantum wells and quantum wires. This leads to drastically different forms of density of states that are so vital to the determination of many physical properties of solids. When the delocalization of electrons in a free electron Fermi gas is considered, the density of states in one, two and three dimensions of bulk metals are found to differ very much from each other. However, the consideration of the electron confinement in broad potential wells yields qualitatively a common discrete energy spectrum. The energy spectrum is independent of dimensionality and shape of the potential wells. The presence of both the potential well confinement and the Fermi gas delocalization in the same nanostructure has been found, an evidence for the partial confinement. As a result of confinement in one or two directions, the electrons move along the confinement coordinate directions to occupy the respective potential well levels (*i*), lying below the Fermi level and tied to the degeneracies d_i . At the same time, the electrons in each case delocalize in the remaining dimensions as they occupy the Fermi gas levels in the delocalization direction of the reciprocal lattice.

Quantum dots exhibit total confinement as against no confinement in bulk materials. Quantum wire and quantum well structures provide only partial confinement to electrons. This behaviour

leads to different expressions for the number of electrons and the density of states for these structures. The expressions with information on delocalization and confinement in quantum nanostructures and bulk are given in Table 16.2. The energy dependence curves of the number of electrons and the density of states are drawn in Fig. 16.10. It is observed that the number of electrons increases with energy for all structures. The behaviour may be accepted as qualitatively similar. But the forms of the density of states are dramatically different which may significantly affect certain properties. Some of these properties are: electron heat capacity, Pauli susceptibility, the intensity of x-ray emission, electron and hole concentrations in semiconductors and the superconducting energy gap.

Table 16.2 Some features of electrons delocalized/confined in quantum wells, quantum wires, quantum dots and bulk samples

Sample	Number of electrons $N(\epsilon)$	Density of states $D(\epsilon)$	Dimensions	
			Confined	Delocalized
Q-well	$C_1 \sum d_i (\epsilon - \epsilon_i(w))$	$C_1 \sum d_i$	1	2
Q-wire	$C_2 \sum d_i (\epsilon - \epsilon_i(w))^{1/2}$	$\frac{1}{2} C_2 \sum d_i (\epsilon - \epsilon_i(w))^{-1/2}$	2	1
Q-dot	$2 \sum d_i \Theta(\epsilon - \epsilon_i(w))$	$2 \sum d_i \delta(\epsilon - \epsilon_i(w))$	3	0
Bulk	$C \epsilon^{3/2}$	$\frac{3}{2} C \epsilon^{1/2}$	0	3

$$C = \frac{V}{3\pi^2} \left(\frac{2m}{\hbar^2} \right)^{3/2}; \quad C_1 = \frac{L^2}{2\pi} \left(\frac{2m}{\hbar^2} \right); \quad C_2 = \frac{2L}{\pi} \left(\frac{2m}{\hbar^2} \right)^{1/2}$$

$\Theta(x) = 0$ for $x < 0$ and 1 for $x > 0$

$\delta(x) = 0$ for $x \neq 0$, and ∞ for $x = 0$, and integrates to a unit area.

$\epsilon_i(w)$ refers to the energy of the level i in the potential well.

There are a large number of applications of quantum well structures in electronics, quantum electronics and photonics where they form heterojunctions. Discrete energy levels of quantum wells have been used for the fabrication of modern infrared detectors. The quantum well and quantum wire-based lasers are other important arrivals where the confinement and the localization of conduction electrons in discrete energy levels is finely tuned. The production of quantum dot lasers is one of the most recent advancements in this direction. In view of their increasing utility, a brief discussion on their design and principle of working is very much in order.

A schematic diagram showing the structure of a quantum dot laser as fabricated by Park et al.* is given in Fig. 16.11. A quantum dot laser diode is assembled on a p-type GaAs substrate. The top layer is derived from a p-type metal with the GaAs contact-layer immediately underneath. There is a 190 nm thick waveguide of $\text{Al}_{0.05}\text{Ga}_{0.95}\text{As}$ that centres a 30-nm thick GaAs region (marked QD) comprising 12 monolayers of $\text{In}_{0.5}\text{Ga}_{0.5}\text{As}$ quantum dots of surface density 1.5×10^{10} per cm^2 . A

* G. Park, O.B. Shchekin, S. Csutak, D.L. Huffaker and D.G. Deppe, *Appl. Phys. Lett.*, **75**, 3267 (1999).

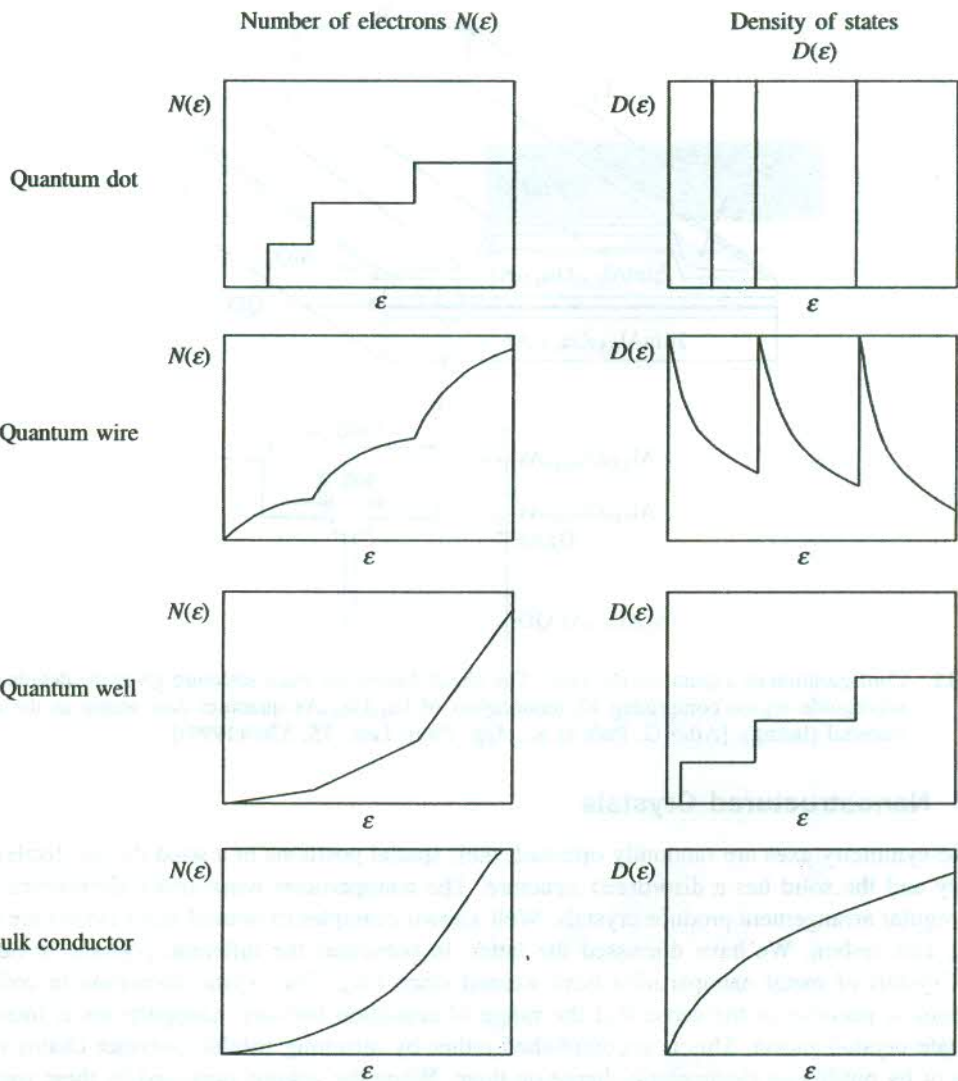


FIG. 16.10 Variation of number of electrons $N(\epsilon)$ (left column) and of density of electron $D(\epsilon)$ (right column) with change in energy in square well—Fermi gas approximation for three quantum structures and their bulk counterpart.

pair of 2 μm thick $\text{Al}_{0.85}\text{Ga}_{0.15}\text{As}$ layers is used to bound the waveguide. The pair lies between the contact layer and the substrate (not shown). The coatings of ZnSe/MgF_2 at the faces of the laser cause the internal back and forth reflection of light to step-up the stimulated emission. The cavity is typically 1 to 5 mm long and 4 to 60 μm wide. The quantum dots assume the role of active atoms as the neon atoms do in a helium-neon laser. The lasing action is excited through the lateral edge of the device. The threshold current for CW operation at room temperature is close to 4 mA and the output radiation happens to fall in near infrared region around 1.32 μm .

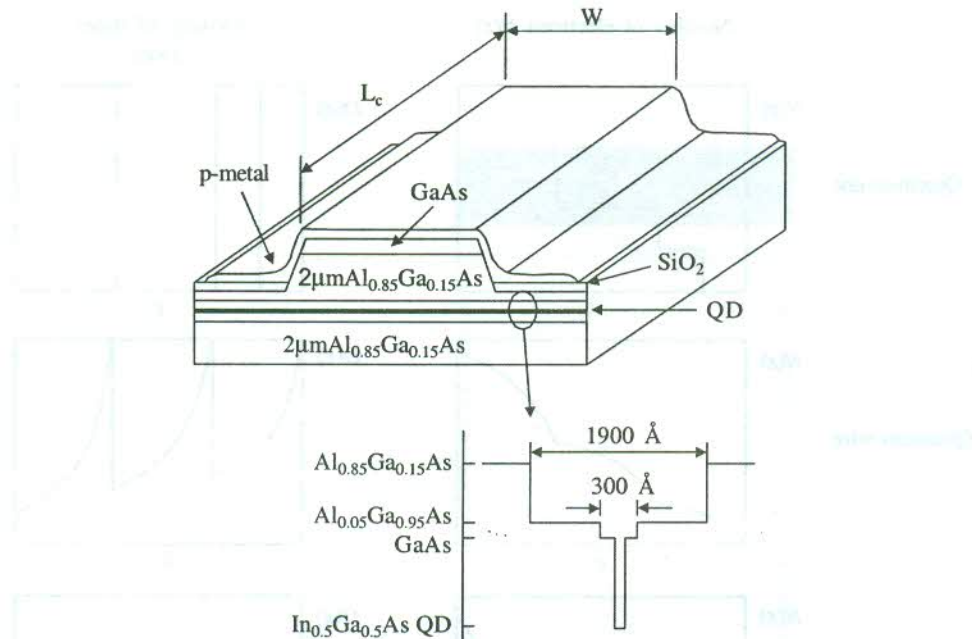


FIG. 16.11 Configuration of a quantum dot laser. The sketch below the main structure gives the details of the waveguide region comprising 12 monolayers of $\text{In}_{0.5}\text{Ga}_{0.5}\text{As}$ quantum dots acting as the active material (lasing). [After G. Park et al., *App. Phys. Lett.*, **75**, 3267(1999)].

16.3.4 Nanostructured Crystals

When the symmetry axes are randomly oriented, their spatial positions in a solid do not display any symmetry and the solid has a disordered structure. The nanoparticles when order themselves in an infinite regular arrangement produce crystals. Well-known examples of natural nanocrystals are those of boron and carbon. We have discussed the latter, in particular the fullerene crystals, in Section 16.3.1. Crystals of metal nanoparticles have existed since long. The crystal formation in colloidal suspensions is peculiar in the sense that the range of repulsion between nanoparticles is increased to facilitate crystallization. This is accomplished either by attaching soluble polymer chains to the particles or by putting an electrostatic charge on them. When the volume occupied by these particles becomes more than half the total volume, the particles start ordering themselves in a regular pattern and crystallize. In view of the limited scope of the book, only two very special classes of these crystals are treated below.

Nanostructured zeolites

The cubic mineral faujasite ($\text{Na}_2, \text{Ca} (\text{Al}_2\text{Si}_4)\text{O}_{12} \cdot 8\text{H}_2\text{O}$) is a typical representative of zeolites. These materials are porous with pores arranged in a regular array. Small clusters can be accommodated in these pores where the van der Waals force between the clusters and the zeolite provide stabilization to the clusters. The material desired to fill the pores is added to the melt of the zeolite. Zeolites are often referred to as molecular sieves since their structure enables them to sift materials. Their structure resembles nanoscopic galleries or chambers interconnected by nanoscopic tunnels or pores (see Fig. 16.12).

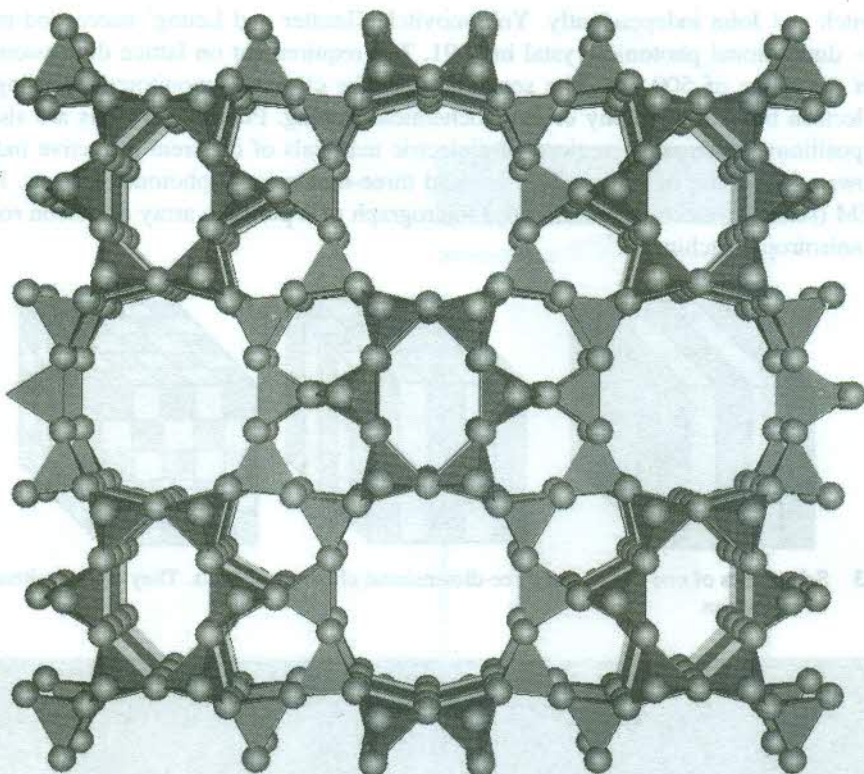


FIG. 16.12 A complex zeolite structure. The holes of different size represent various channels and galleries. (Courtesy Geoffrey Price, University of Tulsa)

Tremendous interest has been shown in using zeolite structures for directed catalysis whereby petroleum is produced more efficiently and one can select desired products from the broad distribution of petroleum components. The particles of a catalyst are found within the galleries of the zeolite in the catalysis. The locally controlled reactivity by the catalyst particles combined with the physical constraints of the gallery and the pore size selects the formation of hydrocarbons of certain specific shape and composition. More efficient use of feedstocks, less wastage and low cost are the salient features of the process of catalysis by design.

The property of zeolites to facilitate the exchange of calcium ions by sodium ions is made use of to reduce water hardness, promoting them as domestic water softeners. Zeolites, in fact, are one of the first broad-scale, highly profitable applications of nanotechnology.

Photonic crystals

Dielectric nanoparticles arranged on a lattice form photonic crystals. The separation between the nanoparticles is artificially adjusted to match the wavelength of the electromagnetic waves (or photons) that the crystal is meant to deal in an application. For this lattice dimension, the electromagnetic waves will suffer Bragg reflection at the Brillouin zone boundaries where an energy gap opens up (refer to Fig. 7.6). The idea of a photonic crystal was first given in 1987 by

Yablonovitch and John independently. Yablonovitch, Gmitter and Leung[†] succeeded in getting the first three-dimensional photonic crystal in 1991. The requirement on lattice dimensions for visible light is in the range of 500 nm. The separation can be clinically monitored by using techniques such as electron beam lithography or electrochemical etching. Photonic crystals are also fabricated with composition of alternating regions of dielectric materials of different refractive indices. Figure 16.13 shows a schematic of such one-, two- and three-dimensional photonic crystals. Figure 16.14 shows SEM (scanning electron microscopy) micrograph of a periodic array of silicon rods produced by deep anisotropic etching.

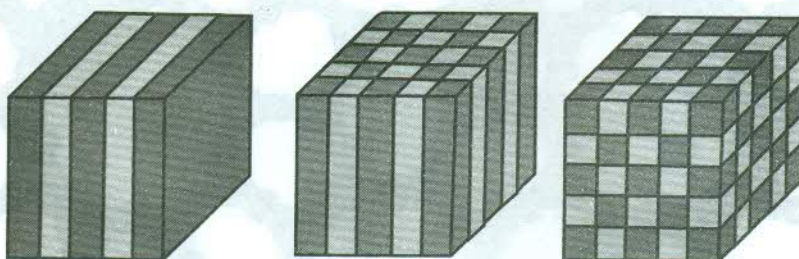


FIG. 16.13 Schematics of one-, two- and three-dimensional photonic crystals. They contain alternating regions of dielectrics.

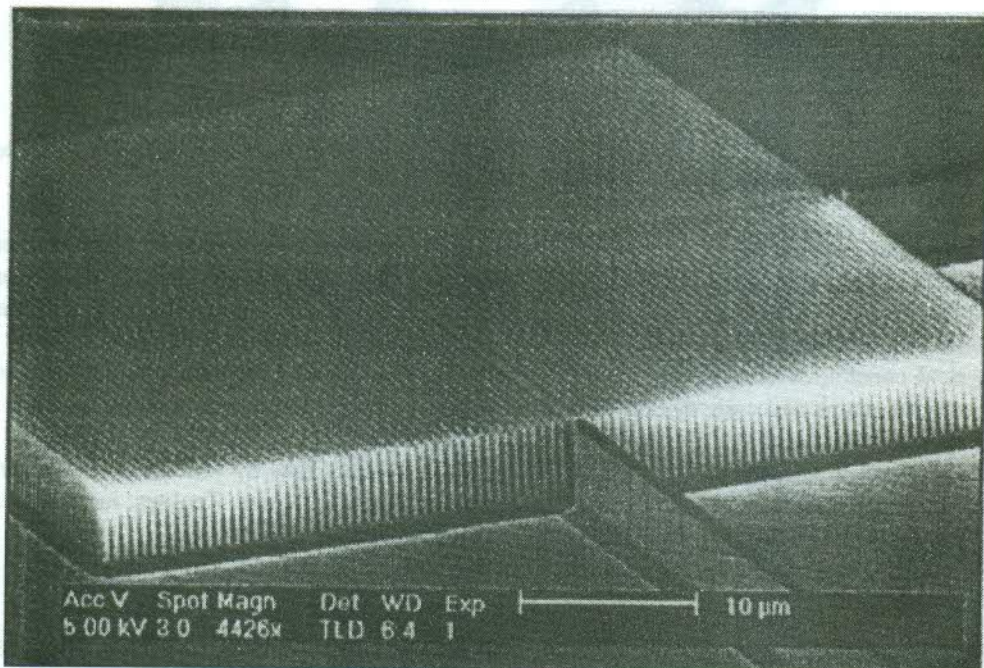


FIG. 16.14 SEM micrograph of a periodic array of silicon pillars made by using deep anisotropic etching. Pillars diameter is 205 nm and height 5 μm . Band gap $\sim 1.5 \mu\text{m}$ for TM polarization. [After T. Zijlstra et al., *J. Vac. Sci. Technol.*, **B17**, 2734 (1999)].

[†] E. Yablonovitch, T.J. Gmitter and K.M. Leung, *Phys. Rev. Lett.*, **67**, 2295 (1991).

Features of electromagnetic wave propagation in photonic crystals are obtained by solving Maxwell's equations in a periodic dielectric medium. In absence of external current sources, the associated Helmholtz equation reads as

$$\nabla^2 \mathbf{H}(\mathbf{r}) + \epsilon \left(\frac{\omega^2}{c^2} \right) \mathbf{H}(\mathbf{r}) = 0 \quad (16.3)$$

where ϵ is the macroscopic dielectric constant of the medium and \mathbf{H} is the magnetic vector associated with the electromagnetic wave.

Because the photon–photon interaction is negligibly small, Equation (16.3) can be solved exactly and the dispersion relation determined accurately. Figure 16.15 shows the dispersion curves for the transverse magnetic modes in a square lattice of aluminium rods designed for microwaves. The symbols Γ and X correspond to special symmetry points in k -space for the square lattice. It is expected that the visible light would be treated similarly at the needed smaller rod separations. In the photonic band structure, there exists a forbidden gap, marked as the photonic band gap in Fig. 16.15. The gap excludes the existence of optical modes within the frequency range spanned by the gap.

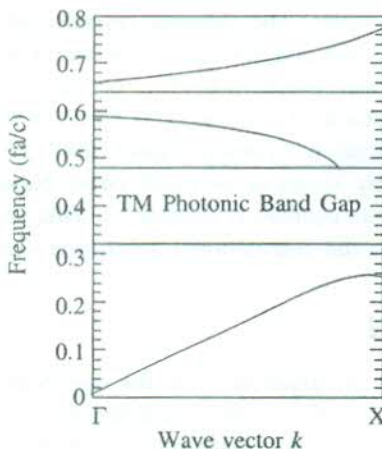


FIG. 16.15 Dispersion curves for a photonic crystal TM mode in a square lattice of aluminium rods designed for microwaves; f stands for frequency and a is the lattice constant. [Taken from J.D. Joannopoulos, *Nature*, 386, 143 (1997)].

Creating a line imperfection in a photonic crystal amounts to forming a waveguide that may enable the crystal to transmit or focus the light of certain frequency. This is done in the lattice of aluminium rods by pulling a row of rods out of the structure. In the modified dispersion curves, a localized energy level (similar to the donor level or the accepter level in semiconductors) appears in the forbidden gap (see Fig. 16.16). The level, in the present case, is often referred to as 'the guided mode'. The frequency of the mode depends on the radius of the rod. The guided mode acts as a pipe which confines the electromagnetic waves and allows them to move along one direction. The confinement in the waveguide is total whereas the light may escape from an optical fibre when the fibre is too much bent, and the requirement on the angle of incidence for total internal reflection is not met. The waveguide may as well be used as a resonant cavity. The frequency of the cavity can be tuned by monitoring the gap.

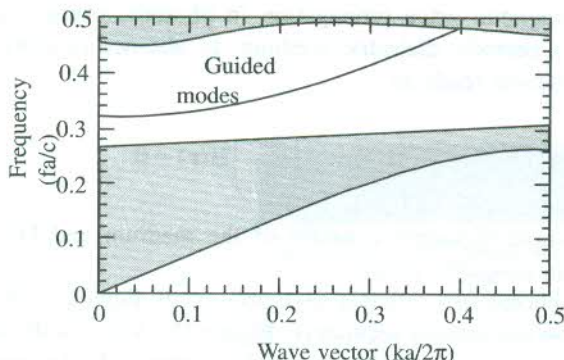


FIG. 16.16 Creation of a level in the forbidden gap (the guided mode) on removing one row of rods from a square lattice of an aluminium photonic crystal. f stands for frequency and a is the lattice constant. [Taken from J.D. Joannopoulos, *Nature* 386, 143(1997)].

These properties provide for blocking the propagation of photons irrespective of polarization direction, localizing photons to a specific area at restricted frequencies, for example using photonic crystals as filters and couplers in lasers. The photonic crystals can also be made to manipulate the dynamics of the spontaneous emission and the stimulated emission independently for lasing action. They serve as an ideal lossless waveguide to confine or direct the propagation of light along a specific channel. Because the photonic crystals work at all wavelengths, they have strong potential for application in telecommunication systems. Apart from providing lossless and noiseless propagation, an optical channel by virtue of its much larger bandwidth carries many times more information than what an electronic channel is capable of. This projects photonics as a technically much advantageous alternative to the conventional solid state electronics.

16.4 POROUS SILICON

Although porous silicon was first produced in 1956, the significant interest in the material became evident only in 1984 with the report of its visible photoluminescence. Porous silicon is also known to display electroluminescence and cathodoluminescence. It appears very surprising because the ordinary silicon has a band gap of 1.125 eV at 300 K and shows emission in the near infrared region. In 1990, Canham brought forward the importance of this phenomenon with special reference to its possible role in the improvement of electronics, based on reducing the dimensions and increasing the functional speed. In a device with reduced dimensions, the interconnects may become three to four times larger than the actual device whose features then get dominated by properties and failure modes in interconnects. The emission of visible light (above 1.4 eV at room temperature) by porous silicon raised the vision of replacing metal interconnects by optical interconnects to overcome this problem. Prospects brightened with the record of high quantum efficiencies (1–10%) in contrast to the low values ($\sim 10^{-4}\%$) for ordinary silicon, an indirect gap material involving phonons in interband transitions. The grossly modified luminescence of porous silicon is, however, interpreted mainly as a consequence of the presence of quantum well, quantum wire and quantum dot structures and the surface defect states.

The current electronic technology is heavily based on silicon because of several advantages it holds over other semiconductor materials. Its abundance, low cost, good thermal and mechanical

properties and excellent passivating characteristics provide silicon a distinct edge over widely used group III-V and II-VI compounds. In addition, the porous silicon light emitting structures can be fabricated using a relatively simple and inexpensive etching technique. Also, the structures can be easily integrated with thriving silicon technology. These have created an extraordinary interest in the study of porous silicon in the recent past.

Electrochemical etching is one of the simplest techniques used to produce porous silicon. A silicon wafer is deposited on a metal at the bottom of the cell made of teflon or polyethylene. The silicon wafer is etched by dilute HF solution contained in the cell at a constant current. The silicon is used as the positive electrode and platinum forms the other electrode (see Fig. 16.17). Canham used a two-step etching process, involving the anodization in dilute HF at low current densities in the first step and the open-circuit pore widening in the next. The open-circuit etching carried out in the dilute HF increases the pore size and produces a blue shift in the photoluminescence. But it is now settled that the pore widening is not required for visible luminescence, though the emission peak is blue shifted in the sample etched over a longer duration. Factors determining the nature and the size of the pore have been identified as: the type of extrinsic silicon (*n*-type or *p*-type), the concentration of HF in the electrolyte, the order of current and the presence of a surface-active agent (surfactant). A *p*-type silicon after etching contains a fine network of pores measuring typically less than 10 nm.

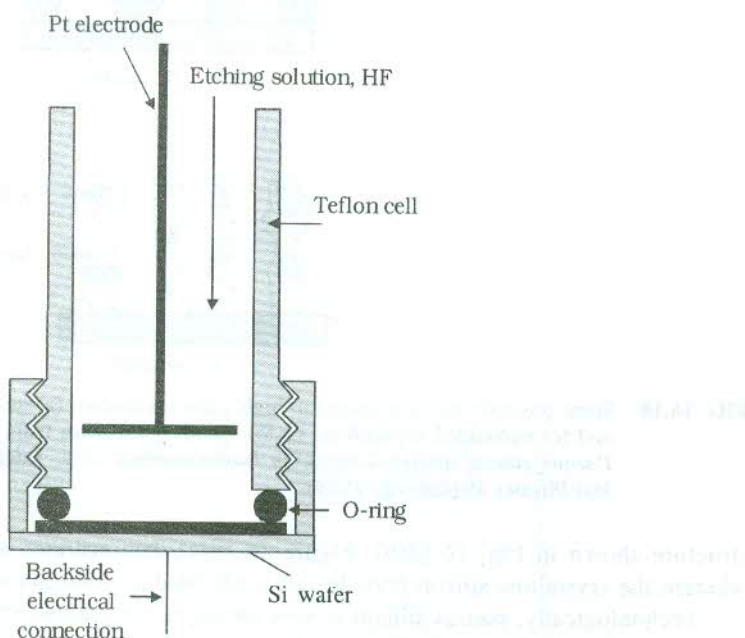
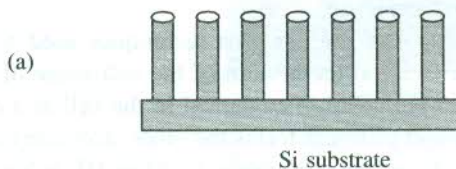


FIG. 16.17 Structure of the cell used for etching a silicon wafer in HF solution to make it porous. (Reprinted from *Handbook of Nanostructured Materials and Nanotechnology*, H.S. Nalwa (Ed.), Academic Press (2000), Vol. 4, Chapter 3, p. 173; with permission from D.F. Thomas (an author) and Elsevier).

Depending on doping and on etching conditions to some extent, specimens of porous silicon can have significantly different structures and surface properties. Some of the common structures of porous silicon are shown in Fig. 16.18. The first of these is the quantum wire structure [Fig. 16.18(a)] with 78% porosity, formed by open-circuit etching. Undulating wires approximate the alternative

Porous Silicon Formation

I. Quantum Wires



II. Undulating Wires or Embedded Particles

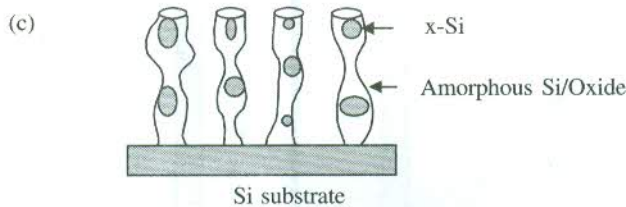
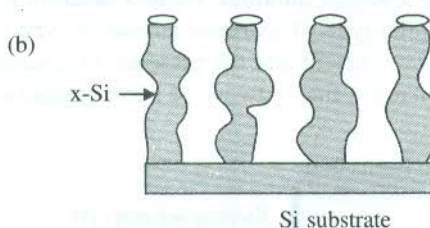


FIG. 16.18 Some possible microstructures of highly porous silicon: (a) quantum wires, (b) 'undulating' wires, and (c) embedded crystallites, ($x\text{-Si}$). (With permission from S.M. Prokes (the author) and IPB, *Porous silicon nanostructures, in Nanomaterials*, A.S. Edelstein and R.C. Cammarata (Eds.), Inst-Physics Publishing, 1998).

structure shown in Fig. 16.18(b). Figure 16.18(c) demonstrates another highly porous structure wherein the crystalline silicon particles are embedded in amorphous silicon or oxide.

Technologically, porous silicon is very attractive for photoelectronic applications. The stability of luminescence under atmospheric conditions and the way it changes on prolonged irradiation are crucial to the fabrication of devices. The exposure to atmosphere and prolonged irradiation both are known to affect the intensity of luminescence in porous silicon adversely. At the present stage, considerable development is required to minimize the effect of these parameters. However, the production of efficient electroluminescent devices holds the key to the ultimate adoption and success of porous silicon. The devices produced so far have unattractive efficiencies that follow from the large requirement on current densities, because the particles are isolated and the electrons must tunnel through oxide.

16.5 PHYSICAL TECHNIQUES OF FABRICATION

Many synthesis routes have been used for the fabrication of nanostructures. Some of them are based on chemical approaches while in others, physical techniques are applied. In this section, we describe a couple of physical techniques, which have assumed importance based on their use for micro-electronic fabrication in semiconductor industry. The techniques selected for a proper discussion are photolithography and scanning probe microscopy.

16.5.1 Photolithography

As per our interpretation in Section 16.3.3, photolithography is a hybrid of the bottom-up and top-down approaches. It is also referred to as “photoengraving”, essentially a process of transferring a pattern into a reactive polymer film, called resist. The resist is used to replicate the pattern into an underlying film or substrate. Lithographic approaches using various lens systems and exposure radiation sources have been applied, all working on similar principles. Among these, photolithography happens to be the most commonly applied technique in the mass production of integrated circuits.

The basic steps of photolithographic process are illustrated by Fig. 16.19. The base is first thin-coated with a resist whose selected areas are then exposed to light through a mask in an image-wise fashion. The developer is now brought in contact with the exposed resist. A positive tone or a negative tone image of the mask is obtained after the developing process, depending on whether the exposed areas of the resist are more or less soluble in the developer as compared to the unexposed areas. The three-dimensional relief image thus produced in the resist material is a replica of the opaque and transparent areas of the mask. The parts of the resist that remain after developing mask the underlying areas of the substrate and prevent them from attack during the subsequent

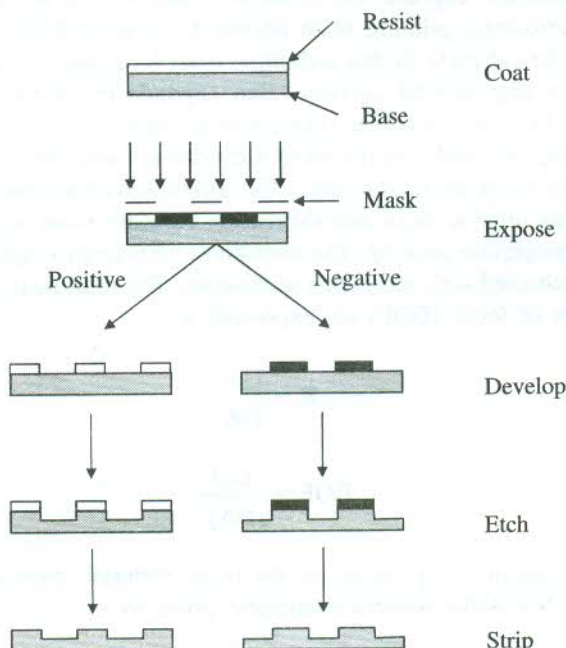


FIG. 16.19 Steps in the photolithographic process of transferring images in the mask to the substrate surface. (After G. Cao, *Nanostructures & Nanomaterials*, Imperial College Press, 2004)

etching operation. When the resist is removed by stripping, the relief image emerges in the underlying substrate. In addition to polymer films, Langmuir–Blodgett films and self-assembled monolayers are other resists that have been used in photolithography. In these applications, photochemical oxidation, generation of reactive groups or cross-linking are used to transfer patterns from the mask to the monolayers. Photolithography is practised in two basic approaches: (1) shadow printing which itself may be of two types, contact-mode printing and proximity printing and (2) projection printing.

The minimum size of elements that can be obtained by photolithography is determined by the limit of resolution in the diffraction pattern extended into the geometrical shadow. For shadow photolithography using a mask consisting of equal lines and spaces of width e , the theoretical limit of resolution is given by,

$$2e_{\min} = 3 \sqrt{\lambda \left(w + \frac{t}{2} \right)} \quad (16.4)$$

where $2e$ is the grating element, w the gap width maintained between the mask and the photoresist surface, λ the wavelength of the exposure radiation and t the photoresist thickness. In the case of hard contact printing ($w = 0$) for 1 μm thick resist film and the light of wavelength 400 nm, the maximum resolution obtained in accordance with eqn. (16.4) is slightly less than 1 μm . The resolution provided by other photolithographic techniques can at best approach but not exceed the value obtained with a contact-mode photolithography, because the mask and the wafer are in intimate contact in this method, enabling the transfer of a mask pattern into a photoresist with utmost accuracy. The presence of dust on the substrate and the non-uniformity in thickness of the photoresist and the substrate degrade the resolution which in practice hardly approaches its maximum value. The proximity printing is an answer to these problems. But the gap introduced between the mask and the substrate in this technique must be controlled with precision for desired results. The increase in gap beyond certain value expands the penumbral region, created by diffraction and worsens the resolution. The diffraction in shadow printing is typically Fresnel type.

In projection printing, the mask and the wafer substrate are separated by several centimetres and lens elements are used to focus the mask image. The diffraction concerned in the technique belongs to Fraunhofer class. Lens imperfections and diffraction considerations account for relatively lower resolution provided by projection printing. The well-known Rayleigh's equation is used to determine the limit of resolution achieved with projection techniques. The minimum resolution feature (R) and the corresponding depth of focus (DOF) are expressed as:

$$R = \frac{C_1 \lambda}{NA} \quad (16.5)$$

$$DOF = \frac{C_2 \lambda}{(NA)^2} \quad (16.6)$$

where C_1 and C_2 are constants, depending on the resist material, process technology and image formation method, and NA is the numerical aperture given by

$$NA = \bar{n} \sin \alpha \quad (16.7)$$

Here \bar{n} is the index of refraction of the image space and α is the maximum cone angle of the exposure light beam.

Using shorter wavelengths of light and larger numerical apertures, sufficiently high resolutions can be achieved. Generally, the minimum feature size that can be obtained with large numerical features (greater than 0.5) matches the wavelength of light used or is slightly less than this.

16.5.2 Scanning Probe Microscopy (SPM)

SPM forms the basis for nanomanipulation and nanolithography. The technique differs from other imaging techniques like scanning electron microscopy (SEM) and transmission electron microscopy (TEM) in its ability to manipulate molecules and nanostructures on a surface.

SPM is a combination mainly of the scanning tunnelling microscopy (STM) and the atomic force microscopy (AFM) which treat two extreme classes of materials when used independently. STM is applied to conductors whereas AFM is ideally suited to deal with dielectric materials.

Scanning Tunnelling Microscopy (STM)

STM has evolved on the principle of electron tunnelling that is perceived as a quantum mechanical phenomenon. Consider two flat surfaces of a metal or semiconductor, separated by an insulator or vacuum. Generally, the transfer of electrons between the flat surfaces would not be possible due to the presence of an energy barrier as shown in Fig. 16.20(a). But when a difference of potential is applied between the surfaces, the shape of the energy barrier changes [see Fig. 16.20(b)]. The electrons on one surface are now under the influence of a force and they tunnel through the separating region in compliance with the quantum mechanical diktat that the electron wavefunction on one side of the energy barrier has a non-vanishing amplitude on the other side of the barrier. Specially, when the thickness of the separating region is very small, the electron wavefunctions (electron waves) on two sides of the separating region may overlap, making tunnelling feasible. The tunnelling is exhibited by the flow of a small current (I), expressed as

$$I \propto e^{-2kz} \quad (16.8)$$

where z is the thickness of the separating region and

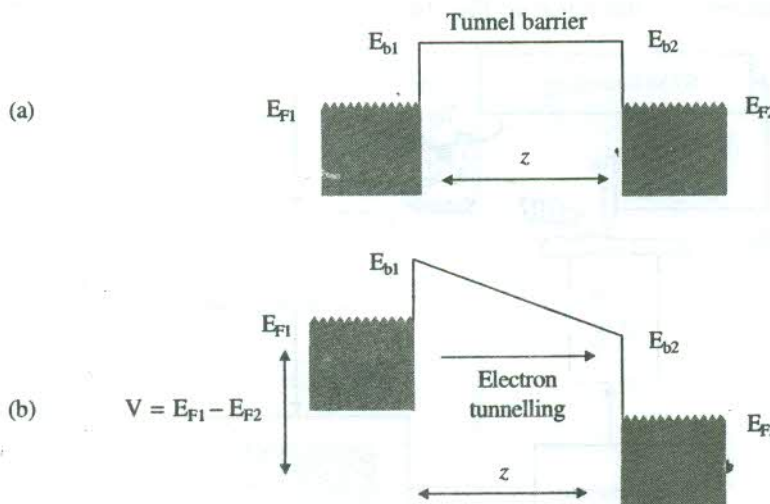


FIG. 16.20 Energy levels in two solids (metals or semiconductors) separated by an insulating or vacuum barrier. (a) in the absence of the electric field (b) when an electric field applied between the solids. E_{F1} and E_{F2} indicate the positions of Fermi level in the two solids.

$$k = \frac{\sqrt{2m(V - E)}}{h} \quad (16.9)$$

Here V is the height of the potential barrier, m the electron mass, E the electron energy and h denotes the Planck's constant. According to relation (16.8), a decrease in the separation (z) by 0.1 nm would increase the tunnelling current by one order of magnitude. This property has been exploited in STM. Binning and Rohrer developed the technique and demonstrated its functioning for the first time in 1982.

In the STM assembly, a conducting wire having a very sharp tip is positioned above the surface of the sample under study. The conducting tip is usually derived from a metal or metal alloy such as tungsten or platinum-iridium alloy. The tip is positively charged and held at a distance about 2–6 nm above the sample surface. Being positively charged, the tip exerts a strong force on electrons in the individual atoms at the surface. Under the influence of this force, the electrons tunnel into the tip, creating the flow of a feeble current (1–10 nA). Thus the tip acts as a probe. The probe tip is moved back and forth in either a constant current imaging mode or an alternating imaging mode. In constant current mode, a feedback loop maintains a constant probe height above the sample profile, involving up/down movement of the probe. The alternating imaging mode is essentially a constant height operation in which the feedback establishes the initial height and the feedback is switched off. As the tip moves, the distance between the tip and the sample surface in this mode keeps varying and so does the current. The alternating current mode provides for faster scan rates whereas the constant current mode is known for producing a contrast directly related to electron charge density profiles.

The tip positions are used to construct a topographic map of the surface. The probe tip is often mounted on a piezoelectric tripod scanner. The piezoelectric arrays accurately control the movement of such a tip in three-dimensions above the sample surface. The method offers scanning resolution of about 0.01 nm in x - y direction and 0.002 nm in z direction. This results in the atomic scale resolution in the three-dimensional image. The first atomic scale resolution was achieved in a STM image of silicon 7×7 restructured (111) surface by Binning and collaborators in 1983. The schematic of a STM assembly is illustrated in Fig. 16.21.

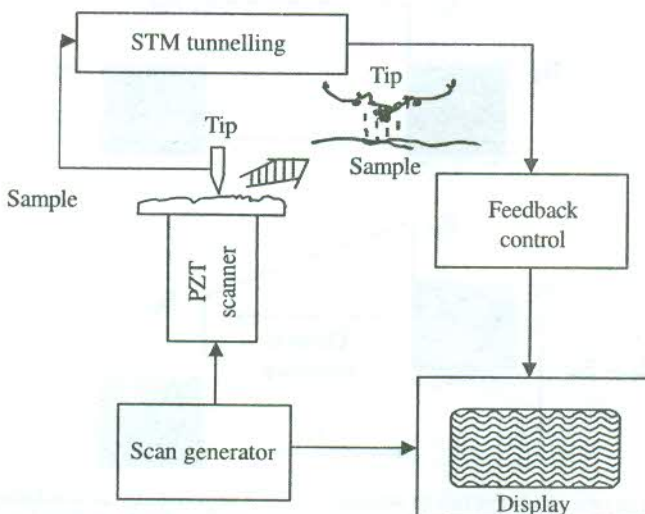


FIG. 16.21 Block diagram of a scanning tunnelling microscope. (After G. Cao, *Nanostructures & Nanomaterials*, Imperial College Press, 2004)

Atomic Force Microscopy (AFM)

AFM is a modification of STM, suitable for application to dielectric materials. The basic difference between the two is that STM monitors the tunnelling current between the surface and the probe tip whereas AFM monitors the force between the surface and the probe tip. Thus AFM is capable of measuring various tip-sample interactions, dominant at respective tip-sample separations. For example, the van der Waals interactions are predominant at small separations and long range forces such as electrostatic attraction or repulsion are significant at large separations. Even capillary forces, in case of condensation of water between the tip and the sample, dominate when the tip to sample distance is increased. The AFM technique is about measuring the motion of a cantilever beam with an ultra small mass and a nanoscale tip. Typically, a force of 10^{-18} N is required for a movement through about 10^{-4} Å. Piezoelectric scanners are used and the images are also created by scanning the tip across the surface. An interference pattern of light beam through an optical fibre serves to monitor the up/down motions of the tip (see Fig. 16.22). The alternative method uses the reflection of a laser beam. The schematic of the technique is depicted in Fig. 16.23. In addition to the laser whose beam is directed at the end of the cantilever, other components of the assembly are—a mirror, a photodiode and an array of piezoelectrics, forming a three-dimensional positioning sample stage.

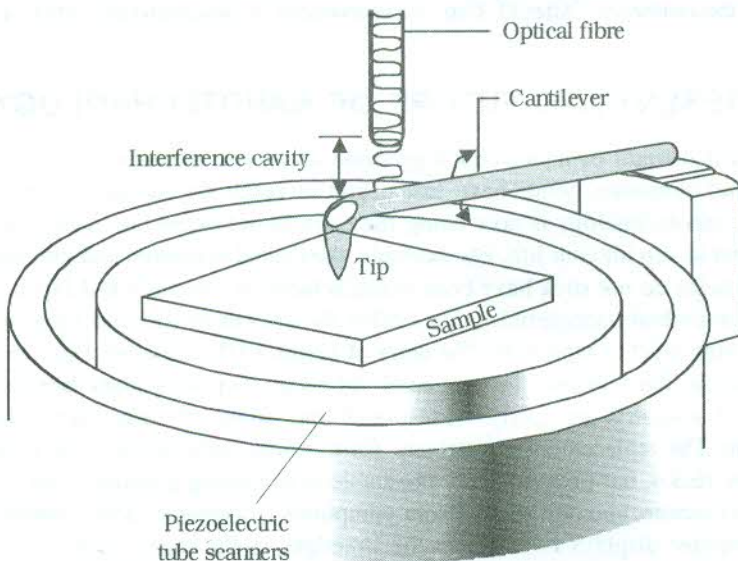


FIG. 16.22 Schematic of an atomic force microscope. A cantilever arm is shown to have the probe tip that traverses the sample surface in coordination with a piezoelectric scanner. (Reprinted from *Introduction to Nanotechnology*, C.P. Poole, Jr. and F.J. Owens, John Wiley 2003; with permission from John Wiley).

The atomic force microscopy is sensitive to the vertical component of surface forces. However, both normal and lateral components of surface forces on the tip can be simultaneously measured with a more versatile microscope called '*the friction force microscope*'. STM and AFM happen to be the prominent members of SPM. The SPM has proved most useful in imaging of surfaces of all kinds of solids and the fabrication and processing of nanostructures.

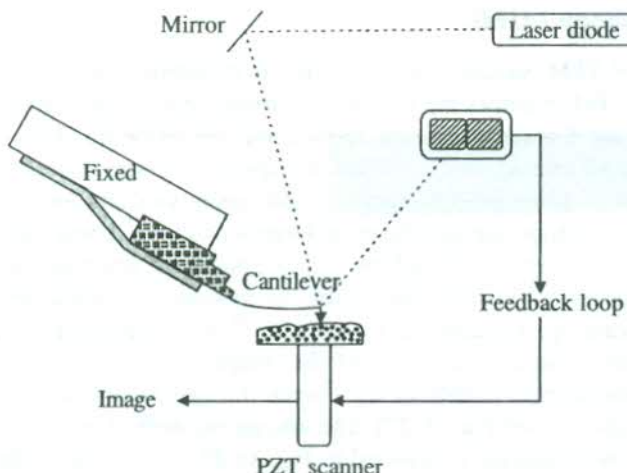


FIG. 16.23 Working of an atomic force microscope. A microscopic positioning device is employed in the assembly where the sample is mounted on a scanner; and the cantilever and tip have to be positioned near the surface. A photo diode records the position of a laser beam, reflected off the top of the cantilever. (After G. Cao, *Nanostructures & Nanomaterials*, Imperial College Press, 2004).

16.6 THE PRESENT AND FUTURE OF NANOTECHNOLOGY

Although the original thought of nanotechnology came about two decades ago, the first few nano-based appliances and consumer goods have just begun to reach the market. Apart from its major impact in industry, nanotechnology is now being felt even in our home and daily life. Coatings and laminates are the first to slip into our life. For example, the coated bathroom and kitchen tiles to which the dirt and grit particles do not stick have been manufactured in Germany and Japan. The tiles have suspensions of antimicrobial nanoparticles that inhibit the growth of rots and fungi, thus helping in maintaining a very high level of sanitation. The entry of harmful UV radiation, a source of skin cancer, is prevented by coating the windows in new Audi A4 series cars with glass laminates.

Applications in industry are fairly widespread and some of them have already become commercially viable. The replacement of catalysts, for example, with zeolites (the molecular sieves), described in Section 16.3.4, has proved highly profitable in extracting gasoline from crude. However, the major support to nanotechnology comes from computers, communications, consumer electronics and medicine. Computer displays have stolen the limelight in the recent past. The heavy TV-like cathode ray tubes (CRTs) are being replaced by more compact flat-panel liquid crystal displays (LCDs) that cause less eye strain and have higher energy efficiency. Samsung and some other companies have started using nanotubes as replacement for scanning electron guns and succeeded in shrinking the screens and reducing the power consumption. Being small, light and efficient, these screens may soon be applied in laptop computers. The nano accounts for the most amazing and spectacular invention in display technology—known as ‘digital paper’. It is very likely to create computers with ultrasharp screens. It would be possible to feed digital files in these computers, facilitating the storage of a large number of books and documents that could be read by holding the screen like a book. In order to make up for the poor screen resolutions, new digital displays have been fabricated by using the same chemicals as employed for paper fabrication. This gives the display a paper-like look. The displays employ elements whose bistable characters enable to maintain a programmed

image without consuming additional power. So, the day is not far in signage when the advantages with digital paper, its commercial viability included, would prepare us mentally to lose our love for the touch and feel of a book, raising the vision of a paperless world.

Nanotechnology has come in a big way to serve the cause of human health. Some details to this effect have already been given in introduction. Additionally, with the use of nanoparticles the accuracy of several tests, including the home pregnancy test, has improved remarkably. Tests have become easy and speedy as well and many of these can be conducted at home. It is also believed that tests for AIDS and anthrax can be made simpler for self-application. Braces and Prosthetics are the examples of goods that are being targeted as early ventures.

A lot of sports equipment is manufactured using nanomaterials. In lightweight motorbikes and sailboats, carbon fibre and graphite composites are made use of. Better football and hockey pads have been made using similar stuff and plastics. Longer bouncing balls and stronger rackets are already on tennis courts. It is expected that nanotubes would find a large application in the manufacture of sports goods.

Lastly, our fashion too does not live uninfluenced by nanotechnology. Developments in molecular-scale composite materials have produced a new generation of clothing and brought nano very much into our fashion arena. Some special features of these products are: resistance to stains, strength and durability, convenience and sharp looks. Biocidal agents similar to those incorporated in bathroom and kitchen tiles, described earlier, are mixed during the manufacture of some fabrics that are ideally suited for use in hospitals where pathogens are common and the risk of infection from each other is very high.

There is no denying the fact that the most outstanding technical advancement during the second half of the 20th century has been the advent of silicon electronics. The miniaturization of microchips, the heart of nanoelectronics and its revolutionary applications, forms the centre of development of silicon technology. The world's first integrated circuit (IC), containing one transistor and a few other components, was built by Nobel Laureate Jack Kilby more than 40 years ago on a slice of germanium, measuring $(7/16 \times 1/16)$ inches. Today, one can place more than 100 million transistors in less than 1 cm^2 of silicon surface area because of the availability of nano-sized transistors ($\sim 90\text{ nm}$ long). Such a single IC can implement an entire electronic system and is called *system-on-chip* (SoC). The raw power of semiconductor fabrication technology is only one aspect of challenges. The other equally important aspect concerns the rapid design of a differentiated product and bringing it to the market place.

In 1975, Gordon Moore gave two empirical laws to describe the growth of IC electronics. According to his first law (famous as Moore's law), the amount of space required to install a transistor on a chip shrinks by roughly half every 18 months. Figure 16.24(a) shows how rapidly the size of a feature on a chip is getting smaller with time. While the first law brings joy to smile, the second law paints a gloomy picture as it predicts that the cost of building a chip fabricating plant (also called fab) doubles every 36 months [see Fig. 16.24(b)]. Thus we see that the shrinking is not to come for free. In fact, the soaring manufacturing cost is posing a big challenge. As we shift from microchip to nanochip, it is strongly felt that the basic principles involved in present chip making cannot survive in totality beyond 2010 and a rethinking will become utmost essential. As for present, the revolutionary applications of nanotechnology and its impact on our life clearly indicate that the age of nano is truly upon us. Its great potential is very much likely to instill an instant motivation among scientists for surmounting the future barriers in sight.

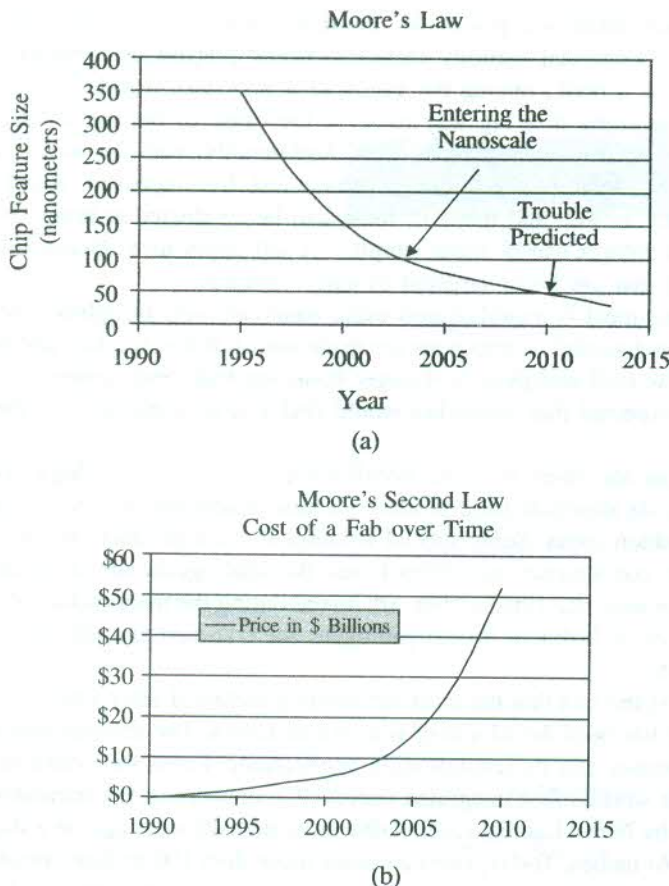


FIG. 16.24 (a) Illustration of Moore's first law: fastly decreasing chip size with time. Chip size shrinks by roughly half every eighteen months.
 (b) Illustration of Moore's second law: increasing cost (Fab) of chip manufacturing plant with time. It doubles every 36 months.

SUMMARY

1. Nanomaterials: at least one dimension $< 100 \text{ nm}$.
2. Nanoparticles: metal nanoclusters, semiconductor nanoparticles, rare gas and CO_2 clusters: $(\text{Xe}_{206})^{4+}$, $(\text{CO}_2)_{216}^{4+}$.
 Cluster Theory: Jellium model, Density functional model.
3. Nanostructures:
 - (A) Carbon clusters:
 Linear—sp hybridization, carbon bond angle $- 180^\circ$, with odd number of atoms
 Closed—carbon bond angles—different from 180° , 120° and $109^\circ 28'$ (the standard hybridization values), with even number of atoms
 Example— C_{60} molecule (fullerene)—called ‘Buckyball’, icosahedral symmetry with spherical surface, composed of 12 pentagons and 20 hexagons.

	Crystalline C ₆₀ (Fullerite) :	FCC symmetry; light, weak and soft as compared to other forms of carbon.
Pure	:	poor conductor.
Alkali metal dopped	:	superconductor, T_c in 20–50 K range. No application on large-scale till date.
Biggest potential	:	as building blocks for making new organic materials
(B) Carbon nanotubes	:	(Single-walled, Multiple-walled) Dia ~ 10–20 nm, 100 μm long
Armchair structure	:	Axis vector parallel to C–C bonds
Zigzag structure and Chiral structure	:	For two other orientations of the axis vector
		Diameter estimated from Raman Spectra

Features:

SWNT are stronger than MWNT ~ 20 times stronger than steel.

Mixtures of metallic and semiconducting nanotubes (2:1)

Defect free metallic nanotubes can carry 10⁹ A/cm² (copper fails at 10⁶ A/cm²)

For semiconducting chiral tubes: bandgap decreases with increasing diameter.

Challenges: (i) physical assembly, as they tend to stick,
(ii) large-scale production of SWNT at a reasonable cost.

Common applications: to increase strength of plastic composites, catalysts, FET as gas detector in electronics and computers.

(C) Quantum nanostructures

Quantum well : only one dimension in nanometre scale

Quantum wire : two dimensions in nanometre scale

Quantum dot : all three dimensions in nanometre scale

Q-nanostructures : have different forms of density of states and exhibit new physical phenomena—not shown by bulk counterparts.

Common applications : quantum wells in heterojunctions used in electronics, quantum electronics, photonics; most recent—Q-dot lasers.

(D) Nanostructured crystals

Examples: boron, carbon, zeolites, photonic

Zeolites: porous, pores arranged in a regular array (serve as molecular sieves) used for directed analysis (production of petroleum more efficiently)—the first broad-scale profitable application of nanomaterials.

Photonic crystals: (Dielectric nanoparticles arranged on a lattice)

- (i) Separation between particles clinically monitored using techniques such as electron beam lithography or by electrochemical etching.
- (ii) Separation adjusted to match the wavelength of em waves to be dealt. For visible light ~ 500 nm.

- (iii) Creation of a line imperfection produces a localized energy level in the forbidden gap, often referred to as 'the guided mode'. It acts as a pipe or waveguide that confines the em waves of a certain frequency and allows them to move along one direction. The confinement is complete.

Common applications:

- (i) Resonant cavity, filters and couplers in lasers
- (ii) Lossless waveguide for light

Projected use: in telecommunication (possible to have crystals working at all wavelengths).

4. Porous Silicon (produced by electrochemical etching technique):

Features:

- (i) Displays visible photoluminescence (ordinary silicon emits in the infrared region). Also electroluminescence and cathodoluminescence displayed.
- (ii) High quantum efficiencies (1–10%), contrasting low values ($\sim 10^{-4}\%$) for ordinary silicon.
- (iii) Light emitting structures fabricated, using a relatively simple and inexpensive etching technique.

Luminescence interpreted as a consequence of the presence of quantum structures and surface defect states.

Attractive for photoelectric applications. Porous silicon has raised the vision of replacing metal interconnects by optical interconnects.

5. Physical Techniques of Fabrication

Basic approaches: bottom-up, top-down

(A) Photolithography (hybrid of bottom-up and top-down)

Practised in two approaches:

- (i) shadow printing (contact mode and proximity printing)
- (ii) projection printing

Shadow printing (Diffraction – Fresnel type)

Limits of resolution

$$2e_{\min} = 3\sqrt{\lambda(w + t/2)}$$

$2e$: grating element

λ : wavelength of exposure radiation

w : gap width

and t : photoresist thickness

Projection printing (Diffraction – Fraunhofer type)

Min. resolution feature

$$R = \frac{C_1 \lambda}{NA}$$

and depth of focus

$$\text{DOF} = \frac{C_1 \lambda}{(\text{NA})^2} \quad \text{with NA} = \bar{n} \sin \alpha$$

C_1, C_2 : constants depending on resist material, process technology and image formation method

NA : numerical aperture

(B) Scanning Probe Microscopy (SPM)

Basis of nanomanipulation and nanolithography. Mainly combination of scanning tunnelling microscopy (STM) and atomic force microscopy (AFM).

(i) STM: (applied to conductors)

Evolved on the principle of electron tunnelling, a quantum mechanical phenomenon.

Tunnelling current

$$I \propto e^{-2kz}$$

with z as the thickness of the separating region

and $k = \frac{\sqrt{2m(V-E)}}{h}$; V is the height of the potential barrier and m is the

electron mass and E its energy.

STM offers atomic scale resolution in the three-dimensional image: ~0.01 nm in x - y direction and ~0.002 nm in z direction.

(ii) AFM: (applied to dielectric materials)

Features:

- (i) Capable of measuring various tip-sample interactions
- (ii) Detects the effect of capillary forces for increased tip-sample separation.
- (iii) Involves the measurement of the motion of an ultralight cantilever and a nanoscale tip. (A force of 10^{-18} N required for movement through 10^{-4} Å.)
- (iv) Sensitive to the vertical component of surface forces.

Difference between STM and AFM:

STM: monitors the tunnelling current between the surface and the probe tip.

AFM: monitors the force between the surface and the probe tip.

QUESTIONS

- 16.1 What are nanomaterials? Describe briefly different types of nanoparticles and discuss their structures.
- 16.2 Describe the structure and properties of various nanoparticles.
- 16.3 Discuss in brief the essentials of jellium model and its success.

- 16.4** Describe the structure and properties of carbon clusters.
- 16.5** What are fullerenes? Describe in detail the structure and properties of fullerite. Mention present and projected applications of fullerenes.
- 16.6** Describe in brief how carbon nanotubes are formed. Discuss their structure, characteristic properties and applications.
- 16.7** What are quantum nanostructures? Give a brief description of their fabrication.
- 16.8** Discuss the salient features of quantum nanostructures and describe their potential applications.
- 16.9** Describe the properties and applications of zeolites.
- 16.10** What are photonic crystals and how are they formed? Discuss in detail their characteristic properties and significance in device fabrication.
- 16.11** Discuss salient features of photonic crystals. Give a systematic account of their present and projected applications.
- 16.12** Describe special features and properties of porous silicon. Discuss critically how it is advantageous to apply porous silicon in devices.
- 16.13** Describe in brief how porous silicon is produced and discuss the significance of its visible photoluminescence and its impact on technology.
- 16.14** Discuss the basic principles of photolithography. Give experimental and theoretical bases of the technique.
- 16.15** Describe the principle and working of a scanning tunnelling microscope. Discuss briefly its application and the resolution achieved.
- 16.16** Describe the principle and working of an atomic force microscope. Give a comparative discussion on its application with reference to STM.
- 16.17** Give a critical review of the present and future of nanotechnology.

SUGGESTED FURTHER READING

- Nalwa H.S., ed., *Handbook of Nanostructured Materials and Nanotechnology*, Vols. 1–5 (Academic Press, Boston, 2000).
- Poole Jr., C.P. and F.J. Owens, *Introduction to Nanotechnology* (Wiley-Interscience, 2003).
- Cao G., *Nanostructures & Nanomaterials* (Imperial College Press, 2004).
- de Heer W.A., “Physics of Simple Metal Clusters”, *Rev. Mod. Phys.* **65**, 611(1993).
- Sugano S. and H. Koizumi, *Microcluster Physics* (Springer-Verlag, Heidelberg, 1998).
- Dresselhaus M.S., G. Dresselhaus and P.C. Eklund, *Science of Fullerenes and Carbon Nanotubes* (Academic Press, San Diego, 1995).
- Ferry D.K. and S.M. Goodnick, *Transport in Nanostructures* (Cambridge Univ. Press, Cambridge, 1997).
- Jacak L., P. Howrylak and A. Wojs, *Quantum Dots* (Springer, Berlin, 1998).

van der Waals Interaction

The van der Waals interaction is a weak attractive force between neutral atoms or molecules. It is due to the presence of dipoles in the molecules, which are induced by the presence of other dipoles. This interaction is important in determining the properties of liquids and solids.

As mentioned in Section 2.3.1, the liquefaction and solidification of noble gases serve as pointer to a certain attractive interaction among neutral atoms or molecules. It is so, especially because the closed electronic configurations of noble gas atoms can be treated as spherical charge distributions that must be disinclined to interact with their neighbours. The attractive interaction, though weak, was introduced as the van der Waals interaction in Section 2.3.1. One of the simplest methods used to calculate this interaction is to follow the perturbation approach of quantum mechanics. To show how this works, we consider the interaction between two widely separated hydrogen atoms. Let \mathbf{R} denote the distance vector between two protons treated as fixed; and let \mathbf{r}_1 and \mathbf{r}_2 represent the position vectors of the electrons relative to the positions of the protons in the respective atoms, as shown in Fig. A-1. The interaction between the two atoms is the sum of the various Coulomb interactions between the charges on the first atom and those on the second atom:

$$U = K e^2 \left[\frac{1}{|\mathbf{R}|} + \frac{1}{|\mathbf{R} + \mathbf{r}_2 - \mathbf{r}_1|} - \frac{1}{|\mathbf{R} - \mathbf{r}_2|} - \frac{1}{|\mathbf{R} - \mathbf{r}_1|} \right] \quad (\text{A.1})$$

where $K = \frac{1}{4\pi\epsilon_0}$, assuming that the atoms are placed in vacuum.

It is possible to expand the denominators in (A.1) in powers of \mathbf{r}_1/\mathbf{R} and \mathbf{r}_2/\mathbf{R} , if $\mathbf{R} \gg$ the Bohr radius a_0 . In this expansion, the first nonvanishing terms are second-order terms, leading to

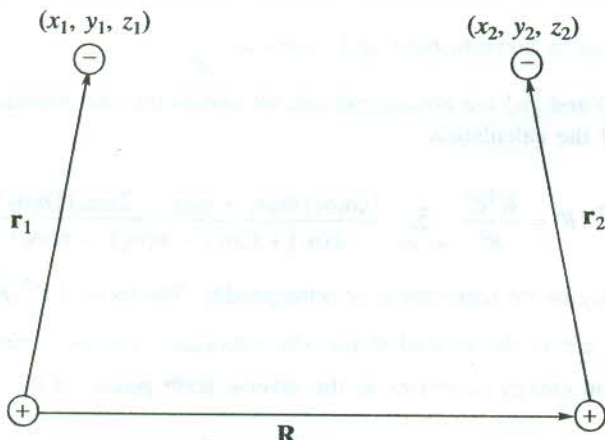


FIG. A-1 Two hydrogen atoms at separation $|\mathbf{R}|$: the protons are shown as (+) and the electrons as (-). $\mathbf{r}_i (i = 1, 2)$ represents the position vector of the electron with respect to the position of the proton in atom i .

$$U = -Ke^2 (\mathbf{r}_1 \cdot \nabla) (\mathbf{r}_2 \cdot \nabla) \frac{1}{R}$$

$$= Ke^2 \left[\frac{\mathbf{r}_1 \cdot \mathbf{r}_2}{R^3} - \frac{3(\mathbf{r}_1 \cdot \mathbf{R})(\mathbf{r}_2 \cdot \mathbf{R})}{R^5} \right] \quad (A.2)$$

The above result assumes importance since its form reveals that for large separations R , the interaction between the two atoms is simply represented by the interaction between the two electric dipoles of dipole moments $e\mathbf{r}_1$ and $e\mathbf{r}_2$. If \mathbf{R} happens to be directed along the z -axis,

$$U = \frac{Ke^2}{R^3} (x_1 x_2 + y_1 y_2 - 2z_1 z_2) \quad (A.3)$$

Let us consider a situation when the atoms are in states $|n_1\rangle$ and $|n_2\rangle$, and no interaction between them is effective with the result that the unperturbed energy of the atoms is $[\varepsilon(n_1) + \varepsilon(n_2)]$. The total energy of the atoms when allowed to interact to first order in the perturbation approach is expressed as

$$\varepsilon(R) = \varepsilon(n_1) + \varepsilon(n_2) + \langle n_1 n_2 | U(R) | n_1 n_2 \rangle \quad (A.4)$$

Using (A.3), the diagonal matrix element of $U(R)$ is written as

$$\langle n_1 n_2 | U(R) | n_1 n_2 \rangle = \frac{Ke^2}{R^3} [\langle n_1 | x_1 | n_1 \rangle \langle n_2 | x_2 | n_2 \rangle + \langle n_1 | y_1 | n_1 \rangle \langle n_2 | y_2 | n_2 \rangle - 2\langle n_1 | z_1 | n_1 \rangle \langle n_2 | z_2 | n_2 \rangle] \quad (A.5)$$

in view of the fact that the wavefunction of the state $|n_1 n_2\rangle$ is a simple product of the states $|n_1\rangle$ and $|n_2\rangle$.

In case either of the atoms is in the ground state, (A.5) contributes only in the second-order as the first-order correction vanishes from the reflection symmetry of the ground state wavefunction. But if both the atoms are in degenerate states, the necessary diagonalization process for $U(R)$ shows that

the first-order correction is nonvanishing and varies as $\frac{1}{R^3}$.

Assuming that $|n_1\rangle$ and $|n_2\rangle$ are nondegenerate, we obtain the first nonvanishing correction only in the second-order of the calculation:

$$\varepsilon^{(2)}(R) = \frac{K^2 e^4}{R^6} \sum_{m_1, m_2} \frac{|\langle n_1 n_2 | (x_1 x_2 + y_1 y_2 - 2z_1 z_2) | n_1 n_2 \rangle|^2}{\varepsilon(n_1) + \varepsilon(n_2) - \varepsilon(m_1) - \varepsilon(m_2)} \quad (A.6)$$

with $m_1 \neq n_1$ and $m_2 \neq n_2$, on the requirement of orthogonality. The form of $\varepsilon^{(2)}(R)$ has two vital features:

- (i) If both sums are in the ground states, the interaction energy is negative.
- (ii) The interaction energy decreases as the inverse sixth power of the separation between the atoms.

We use the substitution

$$\frac{e^2}{a_0^5} \sum_{m_1, m_2} \frac{|\langle n_1 n_2 | (x_1 x_2 + y_1 y_2 - 2z_1 z_2) | n_1 n_2 \rangle|^2}{\varepsilon(n_1) + \varepsilon(n_2) - \varepsilon(m_1) - \varepsilon(m_2)} = \xi \quad (\text{A.7})$$

where ξ turns out to be a dimensionless constant. Detailed calculations for hydrogen atoms in their ground states give $\xi = 6.5$.

Making use of the substitution (A.7) in (A.6), the total energy of the two atoms is written as

$$\varepsilon(R) = \varepsilon(n_1) + \varepsilon(n_2) - \frac{K^2 e^2}{a_0} \left(\frac{a_0}{R} \right)^6 \cdot \xi \quad (\text{A.8})$$

where the third term on RHS shows up as a second-order correction and represents the effective potential energy for interaction between two widely separated hydrogen atoms in their ground states. This effective potential energy is the ‘van der Waals interaction’. It is interpreted as a quantum effect since the interaction energy goes to zero as $h \rightarrow 0$; ($a_0 = \hbar^2/m e^2$).

The occurrence of the van der Waals interaction between two hydrogen atoms sounds misconceived at first sight because the hydrogen atom has no electric dipole moment in its ground state. In fact, the presence of a second atom in the vicinity of an atom marked as the first atom induces a dipole moment in the first atom whose components are proportional to the dipole moment operator of the second atom times R^{-3} . The van der Waals interaction is essentially an interaction ($\sim R^{-3}$) between the induced dipole moment of the first atom and the dipole moment operator of the second atom (and vice versa). It must be clear that it is certainly not the interaction between the induced dipole moment of the first atom and the induced dipole moment of the second atom because that varies as R^{-9} .

Photoconductivity

Illumination of an insulating crystal by photons of energy equal to or greater than the band gap E_g usually excites electrons from the valence band to the conduction band. It makes available the free electrons in the conduction band and the free holes in the valence band, both of which contribute to the electric current under the influence of an external electric field. This phenomenon is called *photoconductivity*.

In addition to the intrinsic process, impurities and imperfections, too, have significant contributions to photoconductivity. We learnt in Section 9.4 that the presence of certain impurities in semiconductors gave rise to the localized energy levels in the forbidden energy gap. Such an energy level is identified as donor or acceptor level depending on whether the level is closed to the conduction band edge or to the valence band edge (see Fig. 9.9). Just as these levels enhance the electrical conductivity of semiconductors, they also contribute appreciably to the photoconductivity. For example, the impurity induced photoconductivity forms the basis of the working of many infrared detectors that are mostly derived from the semiconducting materials. In this case, photoconduction does not necessarily require the excitation through the forbidden gap; instead, low energy photons as may ionize the donor/acceptor atoms cause photoconductivity.

Certain imperfections such as lattice vacancies also create discrete energy levels in the forbidden gap. The carriers of photocurrent are freed from one or other type of the bound state by incident photons. The electrons and holes spend sometime in the conduction band and the valence band, respectively and their flow during this period of time constitutes the photocurrent. They may finally be captured (trapped) at the discrete levels in the energy gap region. These levels are commonly referred to as *traps* (see Fig. B-1). The photocurrent is, however, sustained owing to almost the continuous generation of carriers by a constant photon flux. There is evidence for another type of traps that act as the centres of electron-hole recombination, leading to the restoration of thermal equilibrium. One such trap is labelled as 'Recombination centre' in Fig. B-1. Therefore, the decay of photoconductivity is a natural consequence of switching the illumination off. This is true even for an intrinsic sample since band-to-band process of electron–hole recombination always has a finite probability.

Let us discuss the process of photoconductivity in an extrinsic material for the sake of generality. Suppose that the incident photons add electrons to the conduction band at a rate r_E and other natural processes (e.g. the thermal ionization of donors in semiconductors) do so at a rate r . Let the electron–hole recombination resulting from a variety of energy transformation mechanisms occur at a rate r_C . We may then express the time rate of change of the population of conduction electrons by the following continuity equation:

$$\frac{dn}{dt} = (r - r_C) + r_E \quad (\text{B.1})$$

The RHS of the above equation would have an additional term, if the photoconductor had a

nonuniform distribution of electrons, requiring the excess electrons to move elsewhere. In such a case, dn/dt would have to be replaced with $\partial n/\partial t$ in (B.1) whose present form ignores the spatial dependence.

Denoting the electron density in the equilibrium state (i.e. in the absence of illumination) by n_0 and at any time t by n , we write the excess density of electrons at time t as $n_e \equiv (n - n_0)$. Supposing that this excess density is not very large, we assume that $(r_C - r)$ is proportional to n_e in a crude approximation. The electron lifetime is then conveniently given by

$$\tau_n = \frac{n_e}{(r_C - r)} \quad (B.2)$$

With use of this relation, (B.1) can be written as

$$\frac{dn_e}{dt} = \frac{dn}{dt} = r_E' - \frac{n_e}{\tau_n} \quad (B.3)$$

At a steady state $dn/dt = 0$, and hence the excess electron lifetime is simply n_e/r_E' .

Similarly, the rate of change of the hole population (in the valence band) may be expressed as

$$\frac{dp_e}{dt} = \frac{dp}{dt} = r_E' - \frac{p_e}{\tau_p} \quad (B.4)$$

The lifetimes of electrons and holes are equal, if their generation and recombination both occur exclusively through band-to-band processes ($r = r'$, $r_C = r'_C$, $n_e = p_e$). The two lifetimes have different values, if only one carrier density deviates from its equilibrium value. For example, this happens when low energy photons excite electrons from the donor states in semiconductors. Also, the electron and hole lifetimes are generally different when the recombination occurs by successive capture of electrons and holes at localized impurity states (shown as traps in Fig. B-1).

Some of the important applications in which the photoconductive effect is applied are television cameras, lightmetres, photographic processes (indirectly), photoconductive cells and infrared detectors. Of these, the development of infrared detectors has attracted maximum attention on account of difficulties faced with the detection of radiation at long wavelengths (far infrared region). A high level of sensitivity has been achieved for photons at long wavelengths by using extrinsic photoconductors. In this context the transient response of n_e to the transient illumination is a matter of prime concern. Hence, if the excess generation caused by photons is some arbitrary function $r_E(t)$ of time, our immediate task is to calculate $n_e(t)$. But the dependence of τ_n on n_e as shown by (B.2) complicates the calculation. The task becomes simpler if the lifetime did not deviate much from its value τ_0 at equilibrium so that τ_n could be treated as a constant ($\tau_n = \tau_0$) in a crude approximation. We shall see below that it enables us to have knowledge about $n_e(t)$ over the full time interval before time t .

The generation of electrons takes place as a sequence of instantaneous events, each of which is represented by a delta function. Let us denote the generative activity at time t_0 by $N\delta(t - t_0)$, where N determines the density of electrons created at time t_0 . Then according to equation (B.3), the density of those electrons that survive at time t out of those with density N at time t_0 is

$$n_e(t) = N \exp\left(\frac{t_0 - t}{\tau_0}\right) \quad (B.5)$$

In view of our assumption that the electron lifetime τ_n is constant, equation (B.3) becomes linear.

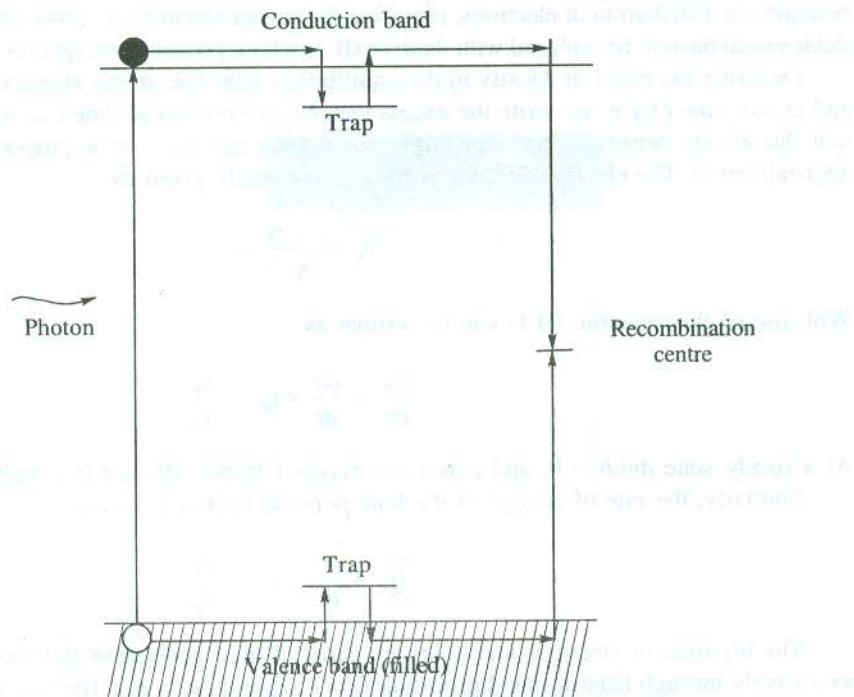


FIG. B-1 The figure shows two different types of traps. One type marked 'trap' affects the freedom of motion of electrons or holes. The other type helps the electron–hole recombination. Such a trap is labelled as 'Recombination centre'.

Therefore, the solution for $n_e(t)$ is simply a sum of the terms of the type in equation (B.5) under the realization that r_E could have been a continuous or discontinuous function of time previously. Hence,

$$n_e(t) = \int_{-\infty}^t r_E(t_0) \exp\left(\frac{t_0 - t}{\tau_0}\right) dt_0 \quad (\text{B.6})$$

It is implicit in the validity of the above relation that the lifetime does not depend on n_e . This enables us to find the time dependence of n_e for a generation function which may be an isolated pulse (delta function, sinusoidal, rectangular, etc.) or a series of pulses.

It may be in order to comment briefly on the crucial role of impurity centres or traps in detection at extremes of the infrared region. For extending the long wavelength limit of detection, the detector must be operated at temperatures low enough for the electrons (holes) to be trapped in dark. The operating temperature is reduced as the ionization energy of impurity centres decreases. Te-doped InSb is a typical example with extremely shallow (close to conduction band edge) donor levels ($\sim 10^{-4}$ eV) because of small effective mass ($m^*/m = 0.01$) and large dielectric constant (~ 25).[†] Even at 1 K, the binding of electrons to donors is not noteworthy. The binding energy in this case is enhanced by applying a magnetic field that reduces the electron orbit, constraining it in the plane perpendicular to the field. The orbit size is smaller than even the Bohr radius at high magnetic fields. This method enables an extrinsic photoconductor to be used for detecting photons of wavelengths

[†] Refer to relation (9.25).

as long as 1 mm. For near infrared region (> 0.1 eV), the inconvenience of working at low temperatures is avoided by incorporating deep level impurities. Germanium doped with Cu or Zn is one such example where the state of ionization of Cu or Zn is adjusted by simultaneous doping with a shallow donor (like As).

In all photoconductive devices, a uniform illumination and a free supply of carriers by the electrodes must be ensured. Otherwise, the space charges would reduce the photocurrent severely. The current may be even stopped, if the electric field of the space charges becomes large enough to cancel the electric field produced by the electrodes. Because of this problem, pulse methods are now very often used to study photoconductivity.

Luminescence

The phenomenon of the absorption of energy in matter and its re-emission (mostly in part) as visible or near visible radiation is generally termed *luminescence*. In specific terms the phenomenon is identified as *fluorescence* if the emission occurs during excitation or within 10^{-8} s of excitation. If the emission occurs after 10^{-8} s, it is commonly known as *phosphorescence* or *after glow*. The period of after glow may be between microseconds to hours. The decay time of 10^{-8} s, taken as the demarcation line between fluorescence and phosphorescence, refers to the order of lifetime of an atom in an excited state for which the return to the ground state is accompanied by dipole radiation.

Crystalline luminescent solids are called *phosphors*. Most of the commercially important luminescent materials, however, are used in the form of microcrystalline powders. The ability of phosphors to convert energy into visible radiation has been immensely exploited for application. But the efficiency of conversion in pure materials is poor with a few exceptions. The high efficiency is mostly related to activator atoms that are special impurity atoms introduced intentionally with a small concentration. Examples of phosphors broadly identified as belonging to two different classes are Cu-activated ZnS and Tl-activated KCl. Anthracene activated with naphthalene is a typical example of the organic phosphors.

Some of the prominent applications of luminescent solids are: fluorescent lamps, CRO, radar, television presentation, nucleon and radiation detectors. Light emitting diodes (LEDs) and solid state injection lasers are examples of more sophisticated devices.

Luminescence in solids is excited in a variety of ways. Based on these, the luminescence may be categorized into the following types:

Photoluminescence. Luminescence excited by the absorption of photons is called *photoluminescence*. The absorption of a photon in the valence band leads to the generation of electrons and holes, photoconductivity and optical emission by a process characteristic of the system under study. Photoconductivity must not be taken as a necessary adjunct to luminescence. The luminescence may be entirely within the luminescence centre.

Cathodoluminescence. Electron-beam excited luminescence is known as *cathodoluminescence*. One of its common applications is in the television tube where the primary electrons of about 15 keV energy strike the luminescent screen and generate a shower of electron-hole pairs. Luminescence occurs by the usual recombination processes. This type of luminescence is far less efficient as compared to photoluminescence.

Electroluminescence. It involves the excitation by electric fields. The most common applications of electroluminescence are luminescent panels (e.g. activated ZnS) as traffic lights, LEDs and injection lasers (see Section 9.10.2).

Thermoluminescence. In this case the excitation is accomplished by heating. The heating keeps on

pumping the electrons stored in a metastable state to the conduction band or an excited state of the activator from where they make a radiative transition. It is shown as a second possibility of the radiative emission in Fig. C-1. One fascinating application of thermoluminescence is in personal radiation dosimeters which are heated periodically to determine the total radiation dose received since previous heating.

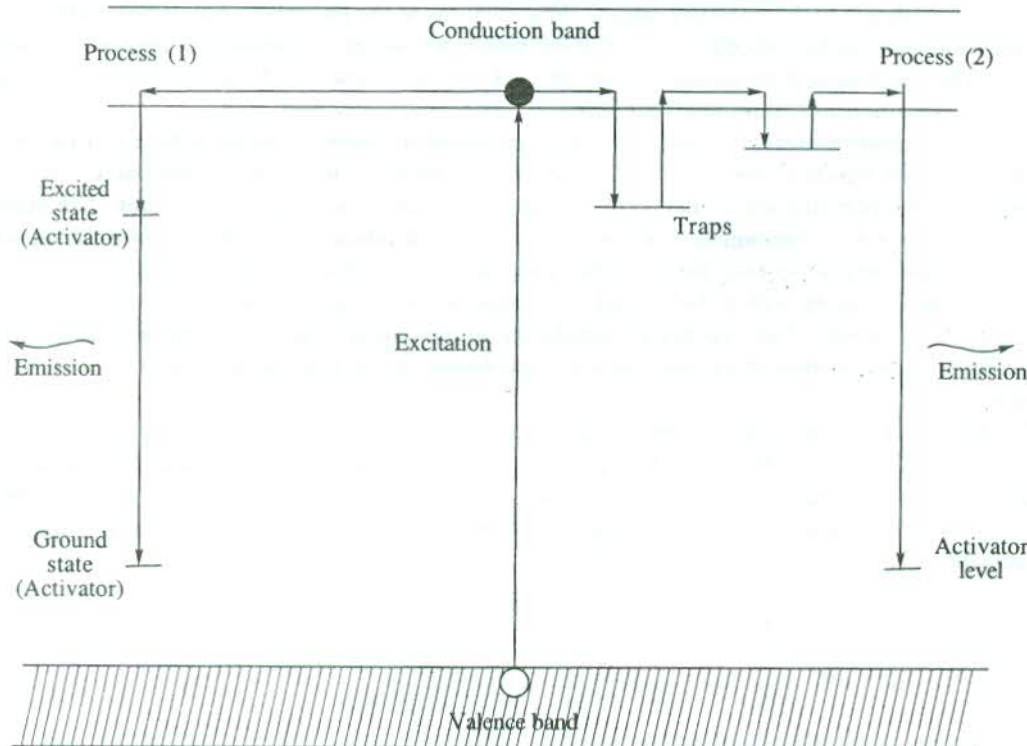


FIG. C-1 Two simple processes of an activated radiative emission. In process (2), electrons at the traps are thermally excited to the conduction band.

Chemiluminescence. It occurs in certain exothermic chemical reactions where the energy is released mostly in the form of the visible radiation.

Activated Luminescence: A Simple Approach

Commercially applied phosphors generally have traces of some impurity or the other to achieve a desired level of efficiency. Controlled amounts of impurities identified as activators are introduced into phosphors to create localized energy levels in the forbidden energy gap of the host phosphor. These localized levels may be of two types: (i) levels of activator atoms; (ii) perturbed energy levels of the host lattice with activators as the source of perturbation. The levels in the latter class may also include those associated with lattice defects such as vacancies. The condition of charge neutrality demands the creation of these vacancies when the oxidation state of an activator atom is higher than that of the atom it substitutes in the host lattice (e.g. Mn^{4+} replacing Zn^{2+} in ZnS). The levels attributed to lattice defects are referred to as *traps*. We will see below that the role of the localized levels is very

vital to the processes of luminescence in real systems. Of these, only those activator levels are crucial which the electrons find easy to enter and leave.

Figure C-1 shows two simple possibilities for a radiative emission. In the first process, an electron in the conduction band (excited from the valence band) drops to an excited activator level and produces radiation by finally descending to the activator ground state. This process is frequent only when the free carrier density is high. The other process involves a trap (located in the forbidden gap), owing its existence to the naturally present imperfections in the phosphor. An electron falls from the conduction band to be trapped at a level from which no radiative transition is allowed (metastable state). The electron is then thermally excited back to the conduction band from where it makes a radiative transition to certain activator level.

Several comprehensive models have been proposed to interpret luminescence in real systems. The process on which a model is based is generally typical of the system under study. As it is not possible to describe all these models here, we restrict ourselves to a general discussion. The treatment shall, however, remain incomplete without mention of an excitation process that involves the movement of an exciton simply because the excitonic processes are central to many optical phenomena. An exciton that is mobile within the crystal may transfer its energy to a luminescence centre that is subsequently excited. The process is significant in the sense that it demonstrates a mechanism whereby the energy from an external source of excitation can be transferred to activators via the host lattice.

The colour and intensity of luminescence are characteristic of the activators used, as is evident from Fig. C-2 for ZnS phosphor. This property has been exploited to increase the 'whiteness' of fluorescence in fluorescent lamps by using two kinds of activators, one for blue and the other for yellow-orange emission. With the overlap of the two broad emission bands, a nearly white light is produced.

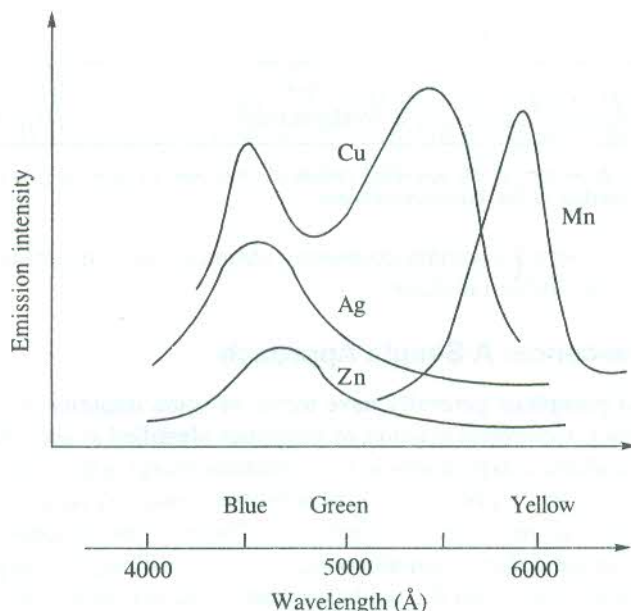


FIG. C-2 The luminescence of ZnS phosphors activated by Cu, Ag, Mn and excess Zn. The source of excitation is ultraviolet light. [After F.A. Kröger, *Proc. IRE*, (Solid State issue), p. 1941 (Dec., 1955).]

Radiative and Non-radiative Emissions

As stated in the beginning itself, the energy of the emitted radiation in luminescence is usually less than the energy absorbed. We use Fig. C-3 to show this. In the figure, the ground state and an excited state of an activator in a phosphor are plotted as functions of the configurational coordinate q whose each value corresponds to a certain configuration of the nuclei around the activator. According to

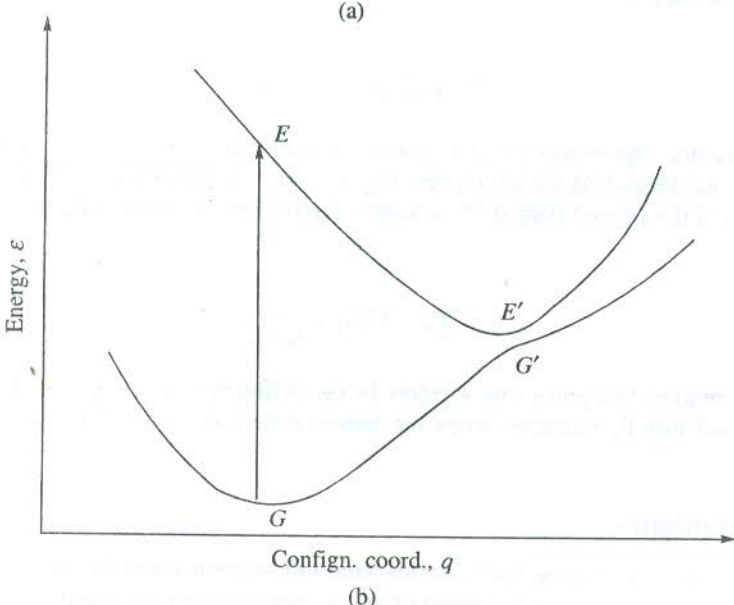
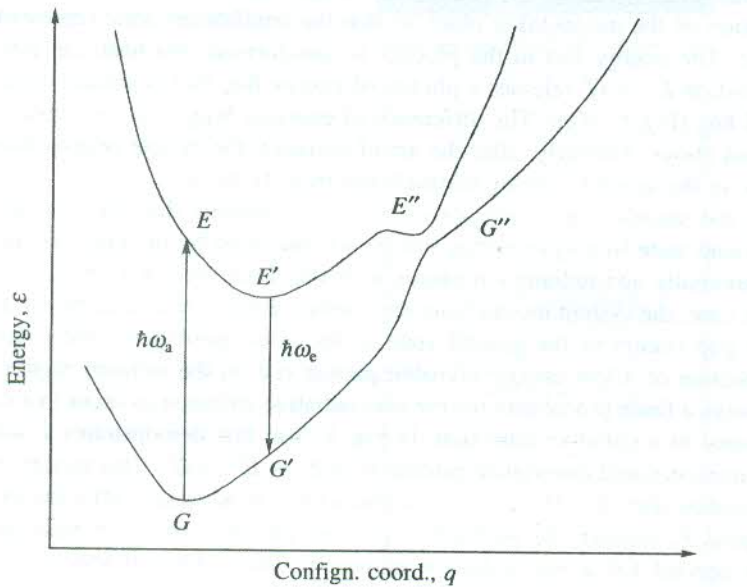


FIG. C-3 Plots of the energy ϵ in the ground state and in an excited state of an activator versus the configurational coordinate q showing: (a) the radiative emission $E' \rightarrow G'$ and the non-radiative possibility $E'' \rightarrow G''$ and (b) purely a non-radiative possibility $E' \rightarrow G'$.

the Frank-Condon principle, the configuration coordinate remains unchanged during a transition. This means that the transitions are vertical, beginning from the minima of the energy curves. The minimum of a curve refers to the configuration at equilibrium in an energy state. With the absorption of energy, the system is excited to the configuration in the excited state. Although the configurational coordinate does not change during the absorption, it does not certainly correspond to the equilibrium in the excited state since E is not at the minimum of the curve. As a result, a small rearrangement in the configuration of the nuclei takes place so that the equilibrium state represented by the point E' is approached. The energy lost in the process is transformed into heat, i.e. into the vibrational energy. The transition $E' \rightarrow G'$ releases a photon of energy $\hbar\omega_e$ that is smaller than the quantum of energy absorbed $\hbar\omega_a$ [Fig. C-3(a)]. The difference of energies $\hbar(\omega_a - \omega_e)$ is consumed in generating phonons, as stated above. Similarly, after the act of emission the system returns finally to the initial equilibrium state in the ground state by thermalizing from G' to G .

Contrary to the situation discussed above, it is also possible that the transition of an excited centre to the ground state in a system may not be accompanied by the emission of a photon. Such a transition is essentially non-radiative in nature, as is illustrated by Fig. C-3(b). After the absorption of energy in this case, the system moves from the configuration E to E' and then a transition through the thin energy gap occurs to the ground state in the non-equilibrium configuration G' with the emission of a phonon or a low energy invisible photon (i.e. in the infrared region).

There is always a finite probability for the non-radiative emission to occur in a configuration that may be most suited to a radiative transition. In Fig. C-3(a) that demonstrates a radiative process, a non-radiative transition could materialize enroute $E \rightarrow E' \rightarrow E'' \rightarrow G''$. This model, proposed by Mott and Gurney[†], implies that the efficiency of luminescence is adversely affected by a non-radiative transition. Suppose P_r denotes the probability per second for a radiative emission and P_n be the probability per second for a non-radiative emission. Then, the efficiency of luminescence is conventionally defined as

$$\eta = \frac{P_r}{P_r + P_n} = \left(1 + \frac{P_n}{P_r} \right)^{-1} \quad (\text{C.1})$$

The temperature dependence of η is mainly determined by P_n , since P_r is nearly temperature independent. In the Mott-Gurney model [see Fig. C.3(a)], the probability of finding an electron in a vibrational level of the excited state at E'' or higher determines the value of P_n . Hence, we may express P_n as

$$P_n = v \exp \left(\frac{-\varepsilon}{k_B T} \right) \quad (\text{C.2})$$

where v is a vibration frequency and ε refers to the difference of energies at E'' and E' .

Thus we find that P_n increases when the temperature rises, leading to a decrease in the value of η .

Decay Mechanisms

Decay characteristics of luminescence provide vital information about the luminescence centres and their energy levels. We discuss below some of the prominent decay mechanisms as are useful in these studies.

[†]N.F. Mott and R.W. Gurney, *Electronic Processes in Ionic Crystals*, 2nd ed., p. 221 (Oxford, 1948).

Temperature-independent exponential decay

Let us suppose that the source of excitation is withdrawn at time $t = 0$ and the number of electrons in an excited state is N_0 at $t = 0$ and $N(t)$ at time t . Also, assume that the probability per second of a radiative transition from an excited state of average lifetime τ is $1/\tau$. If a luminescence centre is shielded well from its surroundings, the lifetime τ does not depend on temperature and on the number of other excited centres. Then, we may write the intensity of luminescence as

$$I(t) = - \frac{dN(t)}{dt} = \frac{N(t)}{\tau} \quad (\text{C.3})$$

Integrating this equation, we get

$$N(t) = N_0 \exp(-t/\tau) \quad (\text{C.4})$$

The substitution of this value of $N(t)$ in (C.3) leads to

$$I(t) = I_0 \exp(-t/\tau) \quad (\text{C.5})$$

where $I_0 = N_0/\tau$, the intensity at $t = 0$.

Temperature-dependent exponential decay

In the luminescence of Tl-activated alkali halides, τ is observed to drop exponentially with increasing temperature though the decay occurs still according to (C.5). Also, the value of τ is of the order of minutes as against 10^{-8} s for a dipole radiation. A model that explains these features of decay involves a metastable state M between the ground state G and an excited state E of an activator as shown in Fig. C.4. In this model the radiative emission (4) starts only when the source of excitation has been removed, i.e. at $t = 0$. During the excitation, i.e. at times prior to $t = 0$, the electrons are collected via

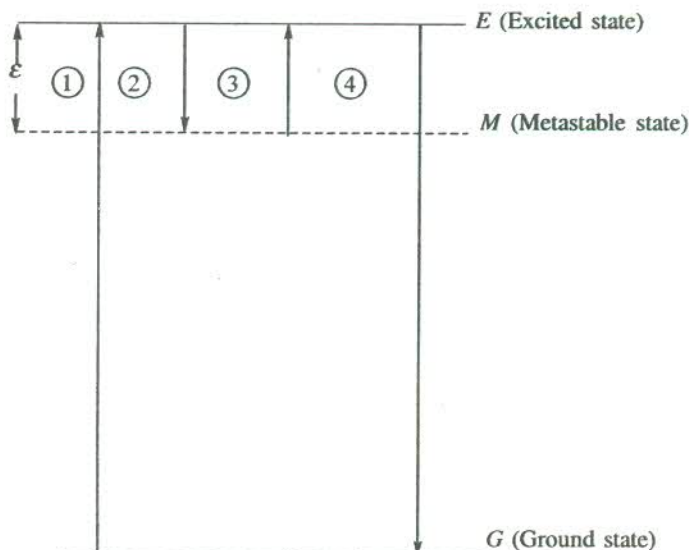


FIG. C-4 Qualitative representation of a delayed emission. The measured lifetime τ of the excited state E is appreciably increased owing to the time spent in storing an electron at the metastable state M and then thermally exciting it to E . The storing is indicated as (2) and the thermal excitation as (3).

(2) at M from E and at $t = 0$ the boiling of electrons [i.e. the thermal excitation (3)] to E begins from where they make the radiative transition to G shown as (4). If ε denotes the energy separation between E and M , then the probability per second for an electron to be excited from M to E is

$$\frac{1}{\tau} = \frac{1}{\tau_0} \exp\left(-\frac{\varepsilon}{k_B T}\right) \quad (\text{C.6})$$

where $1/\tau_0$ is a frequency.

Placing this value of $1/\tau$ in (C.5), we obtain the following form for the decay:

$$I(t) = \frac{N_0}{\tau_0} \exp\left(-\frac{\varepsilon}{k_B T}\right) \exp\left[-\frac{t}{\tau_0} \exp\left(-\frac{\varepsilon}{k_B T}\right)\right] \quad (\text{C.7})$$

This relation shows that the electrons are pumped from the metastable state to the excited state at high rates at higher temperatures. The intensity falls rapidly as the temperature is lowered.

Mössbauer Effect

The resonance phenomenon demonstrated by the emission and absorption of a γ -ray photon without loss of energy owing to recoil of the nucleus and without thermal broadening is known as the Mössbauer effect. This implies that a system in principle would show Mössbauer effect if the nature of atomic binding in the system did not allow a single atom to recoil in the emission and absorption process. Since the thermal broadening turns out to be a function of the recoil energy (to be established in the following section), the recoil-free emission or absorption does not incur thermal broadening. Hence, one of the easiest ways to explain the Mössbauer effect is to demonstrate how the recoil of the nucleus makes the resonance emission and absorption of a γ -ray photon least probable. We approach this exercise by giving below a treatment of nuclear recoil and average thermal broadening for a simple case of γ -ray emission and absorption.

Recoil and Thermal Energies of a Nucleus

Consider the emission of a γ -ray photon from a moving isolated atom. Such a situation is close to realization in a gaseous medium. We assume that the atom moves along a line that coincides with the directions of the γ -ray emission and the recoil of the atom. This simplified approach, however, does not suffer from lack of generality because the motion in other axes remains unaltered.

Denoting the energy of the nucleus at rest in the ground state by E_0 and in the excited state of interest by E_e , we write

$$E_e - E_0 = E$$

Let the γ -ray photon be emitted in the x -direction and the velocity of the atom in this direction at the time of the emission be denoted by \mathbf{u}_x . If the nucleus recoils in the x -direction with velocity \mathbf{v}_R , the energy conservation demands that

$$E + \frac{1}{2} M \mathbf{u}_x^2 = E_\gamma + \frac{1}{2} M(\mathbf{u}_x + \mathbf{v}_R)^2 \quad (D.1)$$

(before the emission) (after the emission)

where M is the nuclear mass and E_γ is the energy of the γ -ray photon.

It should be noticed that \mathbf{u}_x and \mathbf{v}_R are vectors and hence can be oppositely directed. The use of non-relativistic mechanics is valid here as u_x and v_R are both much smaller than the speed of light c .

From relation (D.1), we obtain the difference between the energy of the nuclear transition and the energy of the γ -ray photon:

$$\delta E = E - E_\gamma = \frac{1}{2} M v_R^2 + M u_x \cdot v_R \\ = E_R + E_{DB}$$
(D.2)

In the above relation, E_R represents the recoil energy of the nucleus and E_{DB} stands for the linewidth contributed by the Doppler effect. The composition of the second term in (D.2) indicates that the Doppler broadening energy depends on the recoil energy and the translational kinetic energy of the atom. The mean kinetic energy in the present case of one translational degree of freedom is

$$\bar{E}_k = \frac{1}{2} M \bar{u}_x^2 \simeq \frac{1}{2} k_B T$$

Making use of the above relation, we write the mean Doppler broadening energy as

$$\bar{E}_{DB} = M v_R (\bar{u}_x^2)^{1/2} = 2 \sqrt{\bar{E}_k E_R}$$
(D.3)

It is practically useful to express E_R and \bar{E}_{DB} in terms of the energy of the γ -ray photon E_γ . Applying the law of momentum conservation to the event of γ -ray emission.

$$\mathbf{p}_R = -\mathbf{p}_\gamma$$

or

$$p_R = -E_\gamma/c$$
(D.4)

where p_R is the momentum of the recoiling nucleus and \mathbf{p}_γ is the momentum of the γ -ray photon.

Using (D.4) we express the recoil energy as

$$E_R = \frac{p_R^2}{2M} = \frac{E_\gamma^2}{2Mc^2}$$
(D.5)

On placing this value of E_R in (D.3), we obtain

$$\bar{E}_{DB} = E_\gamma \sqrt{\frac{2 \bar{E}_k}{Mc^2}}$$
(D.6)

Now, it can be shown how the nuclear recoil renders the resonance emission and absorption of γ -rays impossible. In a process of γ -ray emission, the energy of the emitted photon is lower than the nuclear energy level separation E by the recoil energy of the nucleus E_R . Similarly, for the reverse process or the reabsorption of γ -rays to occur the photon energy is required to be equal to $(E + E_R)$. Thus the energy of the absorbed photon differs from the energy of the emitted photon by $2E_R$.

For $E_\gamma = 10^4$ eV and $M = 100$ a.m.u., relations (D.5) and (D.6) respectively give $E_R = 5.4 \times 10^{-4}$ eV and $\bar{E}_{DB} \simeq 5 \times 10^{-3}$ eV at 300 K. In this case the amount of overlap between the emission and absorption profiles, shown in Fig. D-1, turns out to be extremely small and resonance does not occur. In contrast, the magnitudes of E_R and \bar{E}_{DB} for ultraviolet radiation are smaller by several orders. For $M = 100$ a.m.u. and a radiation of energy 6.2 eV (2000 Å), E_R is merely 2.1×10^{-10} eV and \bar{E}_{DB} is of the order of 3×10^{-6} eV at 300 K. These magnitudes lead to a large overlap between the emission and absorption profiles, resulting in a strong resonance emission and absorption.

The above discussion suggests that in the presence of recoil, resonance emission and absorption

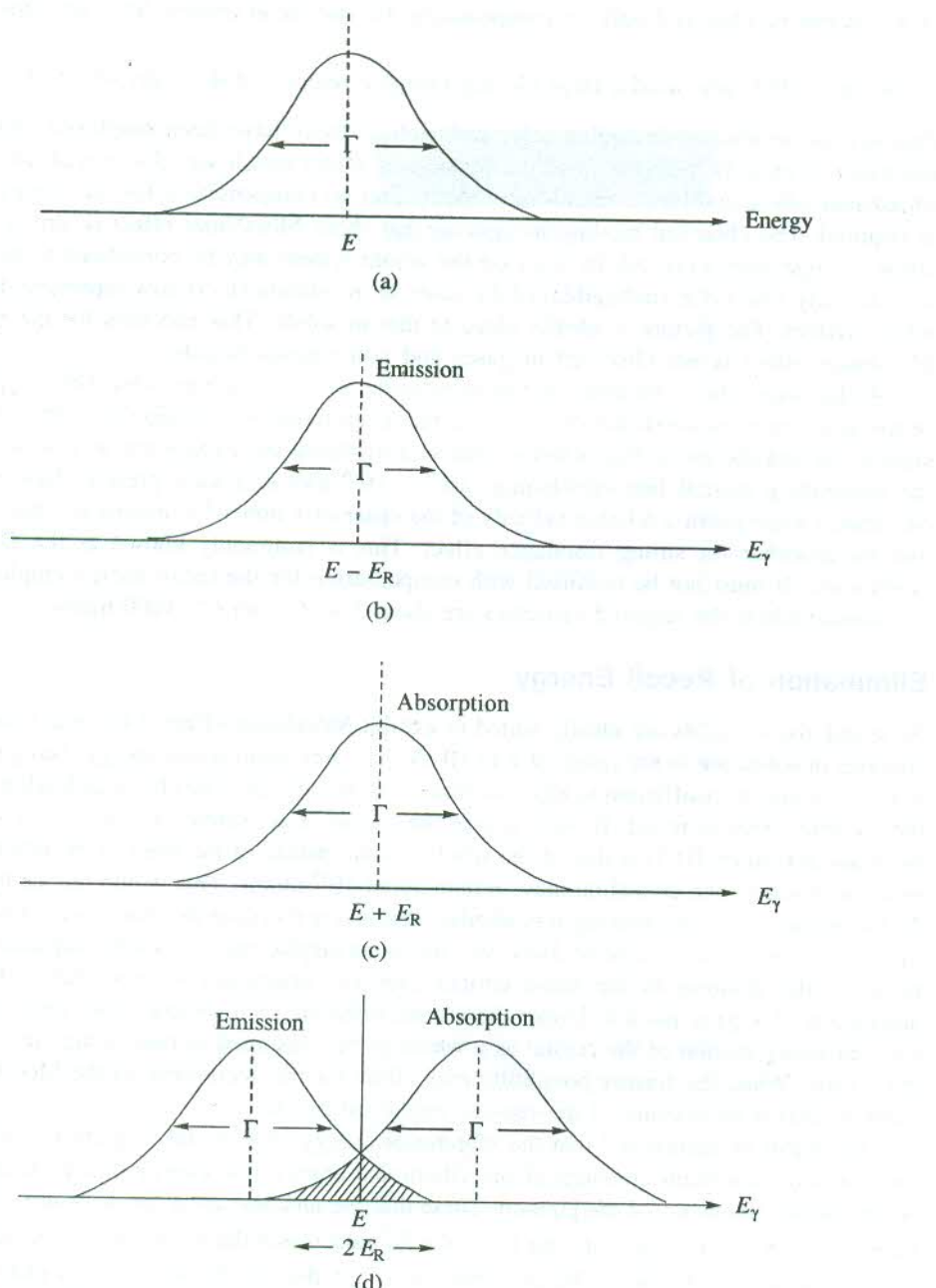


FIG. D-1 (a) Energy distribution of the excited state involved in the emission and absorption of the γ -ray photons. (b) Energy distribution of the γ -ray photons emitted by a free atom. (c) Energy distribution of the γ -ray photons absorbed by a free atom. (d) Overlap of the energy distributions for the emission and absorption of γ -ray photons in a free atom. The overlap region (shaded) is small. This region accounts for the small nuclear gamma resonance.

Symbols:

E is the transition energy; E_γ is the energy of the γ -ray photon; Γ denotes the linewidth, measured at half the height of the maximum.

of γ -rays can be observed only by compensating for the recoil energy. This was first demonstrated

by Moon in 1950 who used a large closing Doppler velocity of the order of $2v_R \left(= \frac{2E_\gamma}{Mc^2} \right)$. Since then several techniques including prior radioactive decay have been employed. But this form of resonance is entirely different from the Mössbauer effect which was discovered later in 1957. The Mössbauer effect involves a recoil-free process and no compensation for the energy disparity $2E_R$ is required. The chemical binding in systems that show Mössbauer effect is strong enough not to allow a single atom to recoil. In this case the whole system may be considered to recoil, leading to an extremely low value (negligible) of E_R since M in relation (D.5) now represents the mass of the whole system. The picture is ideally close to that in solids. This accounts for the reason why the Mössbauer effect is not observed in gases and non-viscous liquids.

At this stage a few comments on line broadening are very much in order. The Doppler broadening in solids is almost non-existent owing to the restricted translatory motion of atoms. It can be further suppressed and the recoil-free activity enhanced by doing the experiment at low temperatures. But the Heisenberg natural line broadening ($10^{-9} - 10^{-6}$ eV) is always present. Hence, in the actual Mössbauer experiment a relative velocity of the order of 1 mm s^{-1} is maintained between the source and the absorber for strong resonance effect. This is commonly known as the *Doppler velocity modulation*. It must not be confused with compensation for the recoil energy employed in Moon's experiment where the required velocities are about $5 \times 10^5 \text{ mm s}^{-1}$ (1600 mph).

Elimination of Recoil Energy

As stated above, solids are ideally suited to exhibit Mössbauer effect. Chemical binding and lattice energies in solids are in the range of 1 to 10 eV. The free-atom recoil energy, being small compared to these values, is insufficient to eject an atom from the crystal. The chemical binding may not allow the emitting atom to recoil. In such a case the crystal is considered to recoil as a single mass and the mass in relation (D.5) is that of the whole crystal instead of the mass of the emitting atom. Even in a fine powder, one crystallite may contain about 10^{15} atoms. This would reduce the recoil energy E_R by an identical factor making it negligible. But in a real crystal the atoms are not so rigidly bound; instead an atom is free to vibrate. However, the mean displacement of a vibrating atom about its mean position (the position in the static lattice) averages practically to zero during the emission or absorption of a γ -ray photon. Under these conditions the recoil energy may either be contained in the translatory motion of the crystal as a whole or be consumed in raising the vibrational energy of the crystal. While the former possibility may allow for the occurrence of the Mössbauer effect, the latter forbids it on account of the reasons explained below.

We learnt in Section 4.7 that the vibrational energy of a crystal is quantized and it can change only in units of certain quantum of the vibrational energy (the energy of a phonon, $\hbar\omega$), where ω is the angular frequency of the phonon. These discrete amounts are $\pm \hbar\omega, \pm 2\hbar\omega, \pm 3\hbar\omega, \dots$. For the transfer of the recoil energy into this form, the E_R must match these amounts. It implies that for values of E_R in between 0 and $\hbar\omega$ or $\hbar\omega$ and $2\hbar\omega$, and so on, the transfer will not take place. For the lowest vibrational excitation in which only one phonon is present, E_R must match $\hbar\omega$. But if $E_R < \hbar\omega$, the Mössbauer effect may occur, materializing through a zero-phonon transition.

Recoil-free Fraction

It follows from the above discussion that the probability of the occurrence of the Mössbauer effect

is determined by the extent to which the use of the recoil energy for creating phonons is inhibited. In other words, the fraction of γ -photons that are emitted without exciting phonons must be large for an intense Mössbauer effect. This fraction is commonly known as the *recoil-free fraction* and denoted by f . Accordingly, the emission of a fraction $(1-f)$ of γ -photons would be accompanied by the excitation of phonons. The simplest vibrating solid is described by the Einstein model in which all atoms are believed to vibrate independently with a common frequency ω_E . If it is assumed that with the emission of a single γ -photon only one phonon is created, in a crude approximation we can write

$$E_R = (1-f) \hbar \omega_E$$

or

$$f = 1 - \frac{E_R}{\hbar \omega_E} \quad (D.7)$$

An emission or absorption line involving purely a recoil-free process is identified as a zero-phonon line. It is imperative to approach a quantitative treatment of the process of emission or absorption in totality for evaluating the recoil-free fraction. We refer back to the case of the γ -ray emission in one dimension. Consider a general event in which with the emission of a γ -photon the crystal containing the emitting nucleus simultaneously undergoes a change in its vibrational state. If the interaction that materializes this event is represented by the Hamiltonian operator H_{int} , the probability P of the event varies according to the following proportionality.

$$P \propto |\langle \psi_f | H_{int} | \psi_i \rangle|^2 \quad (D.8)$$

where ψ_i and ψ_f are wavefunctions describing the initial and final quantum states of the crystal.

The interaction Hamiltonian H_{int} depends on the position of the emitting nucleus, and the momenta and spins of the particles inside the nucleus. The entire process involves the forces within and outside the emitting nucleus. The forces within the nucleus (nuclear forces) that hold the nucleons together are short-range forces in contrast to the long-range nature of crystal binding forces. Therefore, the processes of nuclear decay and the change of the vibrational states of crystal must go independently. Accordingly, the matrix element appearing in (D.8) can be split into two parts. The nuclear part being characteristic of the properties of the nucleus concerned can be treated as a constant. This enables us to represent the matrix element by a single term. The form of H_{int} in the present case leads to

$$P = \text{const.} \times |\langle \psi_f(v) | \exp(i\mathbf{k} \cdot \mathbf{x}) | \psi_i(v) \rangle|^2 \quad (D.9)$$

where \mathbf{k} is the wavevector of the emitted γ -ray photon and \mathbf{x} is the position vector of the centre of the emitting nucleus. The probability for the recoil-free emission f is obtained by replacing $\psi_f(v)$ in (D.9) with $\psi_i(v)$, since the change of the vibrational state is not allowed in a zero-phonon transition:

$$f = \text{const.} \times |\langle \psi_i(v) | \exp(i\mathbf{k} \cdot \mathbf{x}) | \psi_i(v) \rangle|^2 \quad (D.10)$$

Therefore, when the vibrational wavefunction $\psi_i(v)$ is normalized, the probability of the recoil-free fraction is written as

$$f = \exp(-\mathbf{k}^2 \cdot \mathbf{x}^2) \quad (D.11)$$

The vector \mathbf{x} in this relation denotes the random displacement of the emitting atom. Hence, it is appropriate to replace \mathbf{x}^2 by $\langle x^2 \rangle$, representing the component of the mean square displacement in the direction of the γ -ray emission. Using

$$k^2 = \frac{4\pi^2}{\lambda^2} = \left(\frac{E_\gamma}{\hbar c} \right)^2$$

relation (D.11) is rewritten as

$$f = \exp \left[- \left(\frac{E_\gamma}{\hbar c} \right)^2 \langle x^2 \rangle \right] \quad (\text{D.12})$$

It follows from this relation that the recoil-free fraction falls exponentially with increasing γ -ray energy and increasing mean square displacement. This puts an upper limit on the values of E_γ beyond which the Mössbauer effect may not be measurable. The highest γ -ray energy for which the Mössbauer effect has been observed is 155 keV, emitted by ^{188}Os . Similarly, the mean square displacement is too required to be restricted so that the Mössbauer effect might remain detectable in the system of interest. This restriction is most effective in solids of strong chemical binding. On the other hand, the magnitude of $\langle x^2 \rangle$ in gases and non-viscous liquids is so large that the Mössbauer effect becomes immeasurably weak. Relation (D.12) demands that for a detectable Mössbauer effect, $\langle x^2 \rangle$ should be small in comparison with the square of the wavelength λ^2 of the γ -ray photon. Practically, the magnitude is reduced by lowering the temperature (i.e. the experiment is performed at low temperatures). The study of the temperature dependence of recoil-free fraction offers itself as one of the accurate methods of probing lattice vibrations.

The precise nature of the temperature dependence of recoil-free fraction is obtained from an appropriate model of vibrational modes of crystals. Adopting the Einstein model for the evaluation of the matrix element in relation (D.10), we obtain

$$f = \exp(-E_R/\hbar\omega_E) = \exp(-E_R/k_B\theta_E) \quad (\text{D.13})$$

where $\hbar\omega_E = k_B\theta_E$; θ_E is called the Einstein characteristic temperature.

It may be observed that for $E_R \ll \hbar\omega_E$, the above relation reduces to (D.7), obtained by intuition. The Einstein model, though simple, is far from being realistic. The Debye model, another important model, describes the vibrations of real crystals more truthfully. Debye treated the crystalline medium as an elastic continuum and argued that atoms do not vibrate with a single common frequency. He proposed that the atoms in a crystal oscillate with frequencies that range from zero to a maximum ω_D (the Debye cut-off frequency). For details on the Einstein and Debye models, the reader is referred back to Section 5.2. The average frequency of vibration $\bar{\omega}$ in the Debye spectrum is given by

$$\hbar\bar{\omega} = \frac{3}{4} \hbar\omega_D$$

The expression for the recoil-free fraction as derived in the framework of the Debye model is

$$f = \exp \left[\frac{-6E_R}{k_B\theta_D} \left(\frac{1}{4} + \left(\frac{T}{\theta_D} \right)^2 \int_0^{\theta_D/T} \frac{x dx}{e^x - 1} \right) \right] \quad (\text{D.14})$$

where θ_D is the Debye characteristic temperature. It is also expressed as

$$f = \exp(-2W) \quad (\text{D.15})$$

where W is termed the 'Lamb-Mössbauer factor'. It is often referred to as the 'Debye-Waller factor'. The Debye-Waller factor figures in the theory of Bragg diffraction involving the elastic scattering of x-rays. Thus the Bragg diffraction occurs essentially through a recoil-free process. It is in this spirit that the Bragg diffraction is viewed as the Mössbauer effect for x-rays. The difference between the two forms of the Mössbauer effect lies in the relative time involved in x-ray scattering and emission or absorption of γ -rays. Compared to the characteristic time for lattice vibrations the x-ray scattering is fast whereas the lifetime of a Mössbauer nucleus is long.

It is useful to evaluate the expression for f (D.14) in the two extreme limits of temperature. The forms of the expression in these limits are found as under:

$$f = \exp \left[\frac{-E_R}{k_B \theta_D} \left(\frac{3}{2} + \frac{\pi^2 T^2}{\theta_D^2} \right) \right]; \quad \text{for } T \ll \theta_D \quad (\text{D.16})$$

(at low temperature)

and

$$f = \exp \left[\frac{-6 E_R T}{k_B \theta_D^2} \right]; \quad \text{for } T \gg \theta_D \quad (\text{D.17})$$

(at high temperature)

A universal feature of these expressions is that the recoil-free fraction increases with the lowering of temperature. The effect is established by experiments. The Mössbauer effect was discovered[†] while the scattering of 129 keV γ -rays from ^{191}Ir was being measured. In this case $E_R = 0.05$ eV and $E_{DB} \approx 0.1$ eV at room temperature. The emission and absorption lines thus have a considerable overlap and the resonance scattering can be observed at room temperature. Mössbauer cooled both the source and the absorber only to be surprised by the enhanced resonance scattering, an observation not expected on classical considerations. The Mössbauer's observation cannot be regarded as a mere accident. Instead, it is an exhibition of rare genius involved in planning the experiment and explaining the effect. Mössbauer was awarded the noble prize for this invaluable contribution in 1961.

Applications

The most useful feature of the Mössbauer effect is the sharpness of the γ -ray emission. The emission gives a typical Lorentzian line with a width of the order of 10^{-8} eV which is consistent with the measure of the natural line broadening predicted by the uncertainty principle. This is understandable because the width is purely due to the width of the nuclear levels (lifetime $\sim 10^{-7}$ s) involved and no excitation of lattice vibrations (phonons) occurs in the Mössbauer effect. The effective width in the presence of lattice excitation usually conforms to the order of the phonon energies and hence about six orders of magnitude larger.

The width of a spectral line is alternatively expressed in terms of the fractional linewidth obtained by finding the ratio of the linewidth to the energy of the transition. For a γ -emission of energy 100 keV and linewidth 10^{-8} eV in a Mössbauer experiment, the fractional linewidth is 10^{-13} . This implies that the energy of the γ -rays emitted by a Mössbauer nucleus is measurable to an accuracy of 1 part in 10^{13} . Such a precision in measurement is not achievable even with lasers used as common sources

[†] R.L. Mössbauer, *Z. Physik*, **151**, 124 (1958).

of visible and infrared radiations. Thus γ -rays acquire the status of the most stable and accurately defined electromagnetic radiation for use in experiments.

The discovery of the Mössbauer effect has proved to be revolutionary, in particular because of making it possible to use the transition between nuclear levels for studying the magnetic dipole and electric quadrupole interactions (or the hyperfine interactions) of nuclei with surrounding electrons. This is feasible due to the fact that the width of the γ -ray emission lines is smaller than even the characteristic energies of hyperfine interactions. Some of the important applications of the Mössbauer effect are described below.

Study of hyperfine interactions

There are three components of this interaction—the isomer shift (or electric monopole splitting), the nuclear electric quadrupole splitting and the nuclear magnetic dipole splitting. We obtain the charge density of atomic electrons at the nucleus from the measure of the isomer shift. This furnishes useful information about the chemical binding. The gradient of the electric field at the nucleus, created by other ions in the crystal lattice, determines the electric quadrupole coupling. Hence, the quadrupole splitting reveals the symmetry around the nucleus of interest. With no evidence of this splitting the site symmetry of the Mössbauer nucleus is usually taken as cubic or near cubic. The magnitude of splitting indicates the degree of distortion in the cubic symmetry. The measurement of the magnetic dipole splitting is used for studying the properties of magnetically ordered solids. It is an accurate method of determining the Curie and Néel temperatures.

Detection of impurities and short-lived charge states

It is a chemical application having no reference to hyperfine interactions. There is a distinct advantage in using the Mössbauer technique for this purpose on the ground that it provides a non-destructive analysis from which information about the valency and sometimes about the chemical composition of impurities (present in small concentrations) is obtained. It can also be used for detecting elements that have a Mössbauer isotope. But this is possible only for a lattice of atoms of low atomic numbers where the interference of the non-resonant absorption with the transmission of the resonant γ -rays may be ruled out. A slight modification in the technique enables us to study the chemical properties of radioactive atoms present as impurity in a crystal.

Measurement of red shifts

The Mössbauer effect provides the most stable electromagnetic radiation that is measurable most accurately. This property of γ -rays is exploited for the accurate determination of the gravitational red shift and the thermal[†] red shift.

[†] The thermal red shift is a measure of the lowering in the energy of an emitted γ -ray photon caused by heating.

Magnetoconductivity

Magnetoconductivity is the term used to denote the electrical conductivity as modified by the application of a steady magnetic field. On grounds of simplicity, we discuss the case of a metal whose conductivity is interpreted in terms of the nearly free electron motion and examine the same in the classical relaxation time approximation.

The Lorentz force controls the motion of nearly free electrons described by the usual equation of motion:

$$m \frac{d^2\mathbf{r}}{dt^2} + \frac{m}{\tau} \frac{d\mathbf{r}}{dt} = -e \left(\mathbf{E} + \frac{d\mathbf{r}}{dt} \times \mathbf{B} \right) \quad (\text{E-1})$$

The second term on LHS represents the damping force that follows from the collisions with an average relaxation time τ . When the magnetic field is impressed along z -direction ($\mathbf{B} = B\hat{\mathbf{z}}$), the components of electron motion along the three Cartesian axes (x , y , z) are given by the following equations:

$$\begin{aligned} m\ddot{\mathbf{x}} + \frac{m}{\tau}\dot{\mathbf{x}} &= -e\mathbf{E}_x - m\omega_c\dot{\mathbf{y}} \\ m\ddot{\mathbf{y}} + \frac{m}{\tau}\dot{\mathbf{y}} &= -e\mathbf{E}_y + m\omega_c\dot{\mathbf{x}} \\ m\ddot{\mathbf{z}} + \frac{m}{\tau}\dot{\mathbf{z}} &= -e\mathbf{E}_z \end{aligned} \quad (\text{E-2})$$

where ω_c stands for the cyclotron frequency $\left(\frac{eB}{m}\right)$.

We begin with the analysis of the motion along z -direction described by the last of the above equations simply because it is the simplest of the three. For the sake of generality, let us consider the application of an oscillatory electric field,

$$\mathbf{E}(t) = \mathbf{E}(\omega)e^{i\omega t} \quad (\text{E-3})$$

assuming a similar time dependence for the electron instantaneous position ($\sim e^{i\omega t}$).

With these substitutions, the z -component of motion is given by

$$m \left(i\omega + \frac{1}{\tau} \right) \dot{\mathbf{z}} = -e\mathbf{E}_z$$

or

$$\dot{\mathbf{z}} = - \frac{e\mathbf{E}_z}{m\left(i\omega + \frac{1}{\tau}\right)} \quad (\text{E-4})$$

It leads to the following expression for the current density,

$$\mathbf{j}_z(t) = -ne\dot{\mathbf{z}} = \frac{ne^2}{m\left(i\omega + \frac{1}{\tau}\right)} \mathbf{E}_z(t)$$

or

$$\mathbf{j}_z(\omega) = \frac{ne^2}{m\left(i\omega + \frac{1}{\tau}\right)} \mathbf{E}_z(\omega) \quad (\text{E-5})$$

(using $\mathbf{j}(t) = \mathbf{j}(\omega)e^{i\omega t}$)

Comparing (E-5) with the statement of Ohm's Law ($\mathbf{j}(\omega) = \sigma\mathbf{E}(\omega)$), we obtain the z -component of the conductivity tensor

$$\begin{aligned} \sigma_{zz} &= \frac{ne^2\tau}{m(1+i\omega\tau)} \\ &= \frac{\sigma_0}{(1+i\omega\tau)} \end{aligned} \quad (\text{E-6})$$

Similarly, by working with the first two equations of the set (E-2) we can calculate the conductivity in the xy -plane. With the electron instantaneous position and the electric field respectively represented as

$$\mathbf{r}_{xy} = \mathbf{x} + i\mathbf{y}$$

and

$$\mathbf{E}_{xy} = \mathbf{E}_x + i\mathbf{E}_y \quad (\text{E-7})$$

the equation of motion in the xy -plane can be written as

$$m\ddot{\mathbf{r}}_{xy} + \frac{m}{\tau}\dot{\mathbf{r}}_{xy} = -e\mathbf{E}_{xy} + i\omega_c\dot{\mathbf{r}}_{xy} \quad (\text{E-8})$$

The above equation gives

$$m\left[i(\omega - \omega_c) + \frac{1}{\tau}\right]\dot{\mathbf{r}}_{xy} = -e\mathbf{E}_{xy} \quad (\text{E-9})$$

using which we obtain the following expression for the current density

$$\mathbf{j}_{xy}(t) = -ne\dot{\mathbf{r}}_{xy} = \frac{ne^2}{m\left[i(\omega - \omega_c) + \frac{1}{\tau}\right]} \mathbf{E}_{xy}(t)$$

$$\text{or } \mathbf{j}_{xy}(\omega) = \frac{\sigma_0}{[1 + i(\omega - \omega_c)\tau]} \mathbf{E}_{xy}(\omega) \quad (\text{E-10})$$

This gives the component of the conductivity tensor in xy -plane in the form

$$\begin{aligned} \sigma^{xy}(\omega) &= \frac{\sigma_0}{1 + i(\omega - \omega_c)\tau} \\ &= \frac{\sigma_0 [1 - i(\omega - \omega_c)\tau]}{1 + (\omega - \omega_c)^2\tau^2} \end{aligned} \quad (\text{E-11})$$

The relation (E-11) indicates a likely resonance effect at $\omega = \omega_c$. This is confirmed by the results of measurement of some important properties such as surface absorption, reflectance and other related optical phenomena. The resonance effect is famous as "Cyclotron Resonance". It may be remarked here that the use of $(e^{-i\omega t})$ in place of $(e^{i\omega t})$ in solution (E-3) is equally valid. It gives resonance for $-\omega = \omega_c$ which refers to the emission process.

The relationship between the current density and the conductivity tensor in three dimensions may be generalized as

$$\begin{bmatrix} \mathbf{j}_x \\ \mathbf{j}_y \\ \mathbf{j}_z \end{bmatrix} = \begin{bmatrix} \sigma_{xx} & \sigma_{xy} & \sigma_{xz} \\ \sigma_{yx} & \sigma_{yy} & \sigma_{yz} \\ \sigma_{zx} & \sigma_{zy} & \sigma_{zz} \end{bmatrix} \begin{bmatrix} \mathbf{E}_x \\ \mathbf{E}_y \\ \mathbf{E}_z \end{bmatrix} \quad (\text{E-12})$$

Starting with relations (E-2), one readily establishes the following relation involving the real part of the conductivity tensor:

$$\begin{bmatrix} \mathbf{j}_x \\ \mathbf{j}_y \\ \mathbf{j}_z \end{bmatrix} = \frac{\sigma_0}{1 + (\omega - \omega_c)^2\tau^2} \begin{bmatrix} 1 & (\omega - \omega_c)\tau & 0 \\ (\omega_c - \omega)\tau & 1 & 0 \\ 0 & 0 & \frac{1 + (\omega - \omega_c)^2\tau^2}{1 + \omega^2\tau^2} \end{bmatrix} \begin{bmatrix} \mathbf{E}_x \\ \mathbf{E}_y \\ \mathbf{E}_z \end{bmatrix} \quad (\text{E-13})$$

The above relation also demonstrates Hall effect when $\omega = 0$ (i.e. for static electric fields). Considering the components of current in the xy -plane (with $\mathbf{B} = B\hat{z}$),

$$\begin{bmatrix} \mathbf{j}_x \\ \mathbf{j}_y \end{bmatrix} = \frac{\sigma_0}{1 + (\omega_c\tau)^2} \begin{bmatrix} 1 & -\omega_c\tau \\ \omega_c\tau & 1 \end{bmatrix} \begin{bmatrix} \mathbf{E}_x \\ \mathbf{E}_y \end{bmatrix} \quad (\text{E-14})$$

which gives the magnitudes

$$\begin{aligned} j_y &= \omega_c\tau E_x + E_y = 0 \\ (\text{since } j_y &= 0 \text{ in the Hall geometry}) \end{aligned} \quad (\text{E-15})$$

and

$$j_x = \frac{\sigma_0}{1 + (\omega_c \tau)^2} (E_x - \omega_c \tau E_y) \quad (\text{E-16})$$

Substituting E_x from (E-15) in (E-16),

$$j_x = -\frac{\sigma_0}{\omega_c \tau} E_y$$

$$= -\frac{ne}{B_z} E_y$$

$$\text{or } -\frac{1}{ne} = \frac{E_y}{j_x B_z} \quad (\text{E-17})$$

(E-17) is the same as (6.89), representing the Hall coefficient R_H .

- Absorption,
 e.m. radiation (in supercond.), 486
 gamma rays, 567
 infrared, ionic crystals, 107, 109
 ultraviolet, excitons, 369
- Acceptor,
 impurities in semiconductors, 253
 ionization energies, 253
 level, 252
- Acoustic attenuation (in supercond.), 497
- Acoustical branch,
 lattice vibrations, 106–107
 longitudinal, 113
 transverse, 113
- Activated luminescence, 561
- Activation energy, point defects, 361
- Adiabatic,
 approximation, 98
 demagnetization, 410
- Alkali metals,
 band structure, 198
 calculation, 204
 cohesive energy, 45, 207
 crystal structure, 20
 Fermi surface, Harrison construction, 217, 218
 transparency in U.V. region, 318
- Anharmonic effects,
 in solid helium, 99
 potential, 131
 thermal expansion, 132
- Anisotropy energy,
 Bloch-wall, 442, 444
 in ferromagnets, 445
- Anomalous skin effect, 226
- Antiferroelectricity, 347
- Antiferromagnetic,
 magnons, 459
 solids, 447
- Antiferromagnetism, 430, 447
- Atomic,
 cohesion, 32
 form factor, 77
- Atomic force microscopy (AFM), 543, 545
- Axes, crystal
 improper, 10
 rotoinversion, 10
 rotoreflection, 10
 screw, 10
- Augmented plane wave (APW) method, calculation of
 band structure, 207–208
- Azbel–Kaner geometry, cyclotron resonance in metals,
 229
- Band gap, 183, 192
- Band structure,
 calculation methods, 207–208
 GaAs, 242
 Ge, Si, 242–244
 insulators, semiconductors and metals, 197, 240
 of diamond, 199
- Basis, crystal structure, 1
- Bitter powder pattern, 441
- Bloch,
 equations, 421
 theorem, 185
 wall, 444
 wavefunction, 185
- Bloch–Grüneisen T^5 -law, 172
- Bloch $T^{3/2}$ -law, 458
- Body-centred cubic lattice, 6
 reciprocal of, 74
- Boltzmann distribution, 122
- Boltzmann transport equation, 168
- Bonds,
 covalent, 34
 hydrogen, 37
 ionic, 35
 metallic, 34–35
 primary, secondary, mixed, 34–36
 van der Waals, 37
- Bosons, 493–494
- Boundary condition,
 free atom, 206
 periodic, 101–103
- Bragg law, 66

- Bravais lattice, 11
 two-dimensional, 12
 three-dimensional, 13
- Brillouin function, 402
- Brillouin zone, 65–66
- Buckyball (*see* carbon clusters), 524
- Bulk modulus, 54–55
- Burgers vector, 375
- Carbon clusters, 524
- C₆₀, 526
 fullerenes, 526
 fullerite, 526
- Carbon nanotubes, 526
 armchair, 527–528
 chiral, 527–528
 zigzag, 527–528
- Carrier density, in semiconductors
 extrinsic, 259
 intrinsic, 247
- Cathodoluminescence, 560
- Cation,
 mobility, 360
 vacancy, 358
- Cavity, electric field, 296–297
- Cell, primitive, 3
 unit, 1
 Wigner–Seitz, 6–7
- Cellular method, 204–206
- Centred Bravais lattices, 12, 14
- Cesium chloride, crystal str., 20
- Charge neutrality, 355, 358
- Chemical potential, 155
- Chemiluminescence, 561
- Clausius–Mossotti relation, 299, 335
- Close-packed structure, 22
 face-centred cubic, 23
 hexagonal close-packed, 23–24
- Closure domains, 446
- Coercive force, 441–442
- Coherence length, 494, 500
- Cohesive energy, 39–43
- Collisions,
 Drude model, 146
 electron–phonon, 172, 488
 phonon–phonon, 134–136
- Colossal magnetoresistance (CMR) materials, 462
- Colour centres,
 production, 362
 properties, 362–365
 types, 363–365
- Compressibility, 54–55
- Conduction band, 199
- Conduction electron,
 diamagnetism, 409–410
 paramagnetism, 406, 410
- Conductivity,
 electrical, 146–147
 impurity, 253, 361
 ionic, 339
 metallic, 172
 thermal (phonon), 136–140
- Conductor, ideal, 472–474
- Cooper pair, 490
 coherence, 493
 concentration, 493
 size, 493
- Coordination number, 20
- Covalent bond, 34
- Critical temperature (*see* Transition temperature)
- Crystal classes, 13
- Crystal oscillation method, diffraction pattern, 84
- Curie,
 constant, 393
 law, 393
 temperature, 432
 –Weiss law, 330
- Cyclotron resonance, 227–230
 in metals, 229
 in semiconductors, 227–228
- de Haas–van Alphen (dHvA) effect, 232–236
- Debye
 characteristic temperature, 128
 continuum model, 127
 cut-off frequency, 127, 572
 equations, 307
 heat capacity, 128–130
 –Scherer camera, 85
 T³–law, 129
 unit, 293
 –Waller factor, 573
- Defect,
 point, 355
 scattering (of electrons), 174
- Degenerate,
 electron gas, 166
 semiconductors, 262
- Demagnetization, adiabatic (*see* Adiabatic)
- Density functional model, 522
- Density of states, 522
 electrons, 160–161
 phonons, 123
- Depolarization, field, 296
- Diamagnetism,
 Landau, 409–410
 Larmor, 388, 410

- Diamond,
 bonding, 28
 crystal structure, 27
 energy gap, 199
 packing fraction, 26
- Dielectric
 constant, 294
 of semiconductors, 255
 losses, 308
- Diffraction,
 electron, 92
 neutron, 92
 X-ray, 91
- Diffusion,
 constant, 360
 defect, 360
 impurity, 360
 Einstein equation, 360
- Digital paper, 546
- Diode,
 laser injection, 269, 276–279
 light emitting, 276
 tunnel, 273–276
 Zener, 274
- Dipole-dipole interaction,
 electric, 350
 magnetic, 432–436
- Dipole moment,
 electric, 293
 magnetic, 389
- Direct, band gap, semiconductors, 246, 248
- Dislocations, 371
 and grain boundaries, 379
 and slip, 374
 and strength of alloys, 382
 and twinning, 375
 and work hardening, 383
 edge, 375
 elastic energy, 377
 Frank–Read source, 374
 screw, 377
- Dispersion,
 magnon, 456, 459
 phonon, 103, 106
- Domains,
 ferroelectric, 345
 ferromagnetic, 440
- Donor,
 impurities, 253
 ionization energies, 253
 level, 252
- Drift velocity, electrons, 147
- Drude model, 146–148
- Dulong and Petit law, 121
- Easy directions, of magnetization, 442
- Edge dislocations (*see* Dislocations)
- Effective mass,
 electron, 203, 214, 216
 hole, 214, 228
- Einstein,
 characteristic temperature, 124
 diffusion equation, 360
 model of heat capacity, 123–124
- Elastic, constants, 51–52
 energy density, 52
 scattering, 68
 strain, 48
 stress, 48
 waves, 55–59
- Electrets, 331
- Electric,
 field cavity, 296–297
 susceptibility, 295
- Electrical conductivity (*see* Conductivity)
- Electroluminescence, 560
- Electron,
 affinity, 43
 density, 36
 diffraction, 92
 –electron interaction, 490
 heat capacity, 163–167
 –phonon interaction, 324–325, 489
 –phonon–electron interaction, 493
 scattering from defects, 174–175
 impurities, 174–175
 ions, 146
- Electronic g-factor, 395
- Electronic polarizability (*see* Polarizability)
- Electrostriction, 349
- Energy,
 bands, 187
 band structure
 of diamond, 199
 of semiconductors, 240–241
- Energy gap, in superconductors, 483, 484
- Entropy,
 defects, 354, 357
 superconductors, 481–482
- Exhaustion range, of carriers in semicond., 261
- Exchange,
 integral, 438
 interaction, 436, 438
- Excitons,
 Frenkel, 365–366
 Mott–Wannier, 366, 369
- Expansion, thermal, 132
- Extended zone scheme, 193
- Extremal orbit, 234–235

- Ewald,
construction, 82
sphere, 82
- F-centres, 363
- Fabrication, 541
bottom-up, 529–530
top-down, 529–530
- Face-centred cubic,
close-packed structure, 24
lattice, 6
reciprocal of, 74
- Fermi,
energy, 156
level, 155
of free electrons, 218
surface, 163
temperature, 157
velocity, 163
wavevector, 163
- Fermi–Dirac distribution, 155
- Ferrimagnetism, 450
- Ferrites, 450
- Ferroelectricity, 329
- Ferromagnetic,
domains, 440
magnons, 454
resonance, 453
- Ferromagnetism, 430
anisotropy energy, 442
Curie temperature, 432
Curie–Weiss law, 432
Heisenberg approach, 436
hysteresis, 431, 441–442
mean field approach, 431
- Fibre optic communication, 276
- Fick's law, 360
- First-order transition (*see* Phase transition)
- Fluorescence, 560
- Flux quantization, in supercond., 499
- Fluxoid, 500
- Fourier series, expansion, 65
- Frank–Read source, dislocations (*see* Dislocations)
- Free electron,
density of states, 160–161
Sommerfeld model, 157
theory of metals, 145–179
- Free energy,
Gibbs (of supercond.), 479, 482
Helmholtz (of defects), 354
- Frenkel,
defect, 355
exciton, 366
- Fullerenes, 514
- Gallium arsenide, band structure, 244
- Gap,
direct, 244, 246
indirect, 244, 246
- Garnets, iron, 453
- Germanium, band structure (*see* Silicon)
- Gibbs free energy (*see* Free energy)
- Ginzburg–Landau theory, of superconductivity, 498–500
- Glide reflection, 10
- Grain boundary (*see* Dislocations)
- Group velocity,
electrons, 215
phonons, 104
- Growth, spiral, 382
- Grüneisen
–Bloch law, 172
constant (parameter), 134
- Gyromagnetic ratio (magnetogyric), 415
- Hall coefficient,
metals, 153, 172–174
semiconductors, 523
- Hall effect,
classical, 172–174, 266
fractional quantum (*see* Quantum Hall effect)
integral quantum (*see* Quantum Hall effect)
- Hard direction of magnetization, 442
- Hard superconductors, 479
- Heat capacity,
electron, 163–167
lattice (phonon), 120–123, 125–126
- Heisenberg model, 438
- Heitler–London approximation, 437, 439
- Helium, solid, 43, 98
- Helmholtz free energy (*see* Free energy)
- Heterojunction laser, 276
- Heterostructures, 277
- Hexagonal close-packed structure, 23–24
- Hexagonal lattice, 13
reciprocal of, 75–76
- High temperature superconductors, 511
- Hole,
concept, 211
mass: heavy, light, 228
mobility, 266
orbit, 230
- Hund's rules, 396
- Hybrid operations, symmetry, 7, 10
- Hybridization, sp^3 , 37–38, 199
- Hydrogen bonds, 37
- Hysteresis, 330, 347, 431, 441–442

- Ice structure, 38–39
 Icosahedral symmetry, 525
 Icosahedron, 29
 Ideal conductor, 472–474
 Impurities,
 acceptors–donors, 257
 concentration, 247, 259
 doped in semiconductors, 257
 ionization, 257
 resistivity due to, 172
 Indices, Miller, 15
 Indirect gap
 semiconductors, 242, 244
 transitions, 246
 Indium antimonide,
 carrier mobility, 266
 gap energy, 248
 Inelastic scattering, of neutrons by phonons, 115–116
 Injection laser, 276
 Interaction
 dipole-dipole
 electric (*see* Dipole-dipole interaction)
 magnetic (*see* Dipole-dipole interaction)
 electron-electron (*see* Electron)
 electron-phonon (*see* Electron)
 electron-phonon-electron (*see* Electron)
 exchange, 432
 phonon-phonon, 134–136
 Interatomic force, 32–33
 Interstitial atom, 355
 Intrinsic carrier
 density, 247
 Inversion symmetry, 8
 Ionic,
 bonds, 35
 conductivity (*see* Conductivity)
 polarizability (*see* Polarizability)
 radii, 45
 Ionic crystals,
 infrared absorption, 108
 lattice energy, 40–41
 Iron group, 396, 404
 Isentropic demagnetization, 410
 Isotope effect,
 on T_c of superconductors, 488–489
 on thermal conductivity, 141
- Jellium model, 522
 Josephson effect, 504
 Josephson junction, 504
 Jump frequency, 361
 Junction,
 laser, 276
 p-n, 269
 rectifier, 273
 voltage regulator, 274
- k*-space, 66
 Kelvin relation, 179
 Knight shift, 419
 Kramers–Kronig relations, 307, 311
 Kronig–Penney model, 187–189
- LA modes, 113
 Landau,
 levels, 223, 285–286
 tubes, 223–224, 233
 Landau diamagnetism, 409–410
 Lande' splitting factor, 395
 Langevin function, 392
 Langevin's theory,
 of diamagnetism, 388–391
 of paramagnetism, 391–394
 Larmor diamagnetism (*see* Diamagnetism)
 Larmor precession frequency, 390
 Laser,
 buried heterostructure, 278
 double heterojunction, 276
 injection, 276
- Lattice,
 Bravais, 12–13
 defects, 355–356
 direct, 63
 energy (ionic crystals), 42
 reciprocal, 63
 types, 13
 vibrations, 98
- Laue,
 method, 84
 photograph, 64
 Law of mass action, 252
 LCAO method, 200
 Lennard–Jones potential, 43
 Lenz's law, 475
 Line imperfections, 355, 371–378
 Line with, magnetic resonance, 421
 Lithography, 520, 541
 photolithography, 541
 LO modes, 113, 320
 Local electric field, 296
 London–London equation, 475, 445–476, 499
 London penetration depth, 476, 501
 Lorentz field, 296
 Lorentz model, 153–155
 Lorenz number, 152
 Loss factor, dielectrics, 309
 Low angle grain boundaries (*see* Dislocations)
 Luminescence,
 activated, 561
 –cathodo, 560
 –chemi, 561
 decay mechanisms, 564
 –electro, 560

- photo, 560
- thermo, 560
- Lyddane–Sachs Teller (LST) relation, 323
- Macroscopic electric field, 292
- Madelung constant, 40
- Magnetic,
 - dipole–dipole interaction, 332–335
 - dipole moment, 388
 - domains, 440
 - flux, quantum, 500
 - ordering, 430–431
 - resonance (NMR, EPR), 414–415, 418
 - susceptibility, 388
- Magnetite, 450–451
- Magnetization,
 - definition, 387
 - saturation, 440
- Magnetoconductivity, 575–578
- Magnetocrystalline energy, 442
- Magnetogyric ratio (*see* Gyromagnetic ratio)
- Magneton,
 - Bohr, 394
 - nuclear, 409
 - numbers, 403
- Magnetoresistance, 155, 265, 266
- Magnons,
 - antiferromagnetic, 459
 - dispersion relations, 456, 459
 - ferromagnetic, 454
- Manganites, 463
- Matthiessen's rule, 174
- Maxwell–Boltzmann distribution, 145, 146, 155, 156
- Maxwell equations, 292
- Mean field approximation, 431
- Mean molecular field, 431
- Mean free path,
 - electron, 147
 - phonon, 137
- Meissner–Ochsenfeld effect, 471
- Mercury, superconductivity, 468
- Metal–insulator systems, 463
- Metal organic chemical vapour deposition (MOCVD), 278
- Metallic bond, 34–35
- Metals,
 - cohesive energy, 45, 207
 - crystal structure, 20–21, 23–24
 - electrical conductivity, 146–147, 172
 - Fermi surface, 237
 - free electron theory, 145–179
 - thermal conductivity, 150–153
- Metastable state, 565
- Miller indices, 15
- Mirror plane, symmetry, 8
- Mobility,
 - electrons, 266
 - holes, 266
 - ions, 361
- Molecular beam epitaxy (MBE), 278
- Molecular crystals, 369
- Monoclinic symmetry, 13
- Moore's law, 547
- Mössbauer effect, 567
- Mött–Wannier excitons, 366, 369
- NaCl (*see* Rock salt)
- Nanoparticles, 521
- metal nanoclusters, 521
- semiconductors, 523
- Nearly free electron model, 190
- Neél temperature, 447
- Neutron diffraction, 91
- Neutron inelastic scattering, 115–116
- Noble gas solids, 43–44
- Non-radiative,
 - emission, 563, 564
 - transition, 564
- Normal modes, 98, 112
- Normal processes, 134
- n*-type semiconductors, 253
- Nuclear magnetic resonance, 418
- Nuclear magneton, 409
- Oblique lattice, 12
- Ohm's law, 147
- Onsager's quantization, 226
 - area of Fermi surface, 225
- Open orbits, 230–231
- Optical,
 - branch, 106
 - soft modes, 339
- Optical phenomena, 309
- Orbach process, spin-lattice relaxation, 420
- Orbits,
 - electrons, 230
 - extremal, 234
 - holes, 231
 - open, 230–231
- Order parameter, 342, 343
- Orientational polarizability (*see* Polarizability)
- Orthorhombic symmetry, 13
- OPW method, band struct. calc., 208
- Oscillation method, crystal (diffraction), 84
- Oscillations of magnetic moment (*see* dHvA effect)
- Overlap integral, 201
- Overlapping of bands, 198

- Paramagnetic resonance, electron, 415
 Paramagnetism, 387
 conduction electrons (Pauli), 409, 410
 Curie–Weiss (Langevin), 391, 410
 nuclear, 409
 van Vleck, 404, 410
 Peltier effect, 178
 Penetration depth, superconductors, 476, 501
 Periodic boundary conditions, 101–103
 Periodic potential, 64
 Periodic zone scheme, 193–194
 Permeability, 309
 Permittivity, 294
 Perovskite structure, 335
 Persistent current, 470
 Phase sensitive detection, 235
 Phase transition,
 first-order, 344–345
 second order, 342–343
 Phase velocity,
 electrons, 214–215
 phonons, 104
 Phonon scattering,
 by defects, 141
 by electrons, 174
 by phonons (N- and U-processes), 135–136
 Phonon-assisted transitions, 246–247
 Phonons,
 dispersion relations, 101, 105
 heat capacity (*see* Heat capacity)
 occupancy, 114
 thermal conductivity, 136–141
 Phosphorescence, 560
 Photoconductivity, 556
 Photonics, 278
 Photonic crystals, 535–538
 Piezoelectric crystals, 329, 351
 Planck distribution function, 123
 Plasma,
 definition, 311
 oscillations, 312
 Plasmons, 315
 Point defects, 355–371
 Point groups, Schönflies symbols, 17–19
 Polariton, 321
 Polarizability,
 electronic, 301
 ionic, 304
 orientational, 305
 Polarization catastrophe, 335
 Polaron, 324, 356, 371
 Polyhedron, atomic, 6, 204
 Porous silicon, 538–540
 Potassium dihydrogen sulphate, phase transition, 331
 Powder method, X-ray diffraction, 85
 Primitive cell, 3–7
 Printing:
 projection, 542
 shadow, 542
 Pseudopotential method, band theory, 208
 p-type semiconductors, 256
 Pyroelectric crystals, 329

 Quantization,
 electron orbits in magnetic field, 224
 flux in supercond., 499
 lattice vibrations, 113
 spin waves, 453
 Quantum Hall effect (QHE),
 fractional, 288
 integral, 282
 Quantum interference, 508
 Quantum solid, 43, 99
 Quantum structures, 529
 quantum dot, 530–533
 quantum dot laser, 532–534
 quantum well, 530–533
 quantum wire, 530–533
 Quantum well structure, 278
 Quartz,
 crystal, 349
 piezoelectricity, 349
 Quasicrystals, 29
 Quenching, of orbital angular momentum, 404

 Radiative,
 emission, 564
 transition, 564
 Raman spin-lattice relaxation, 420
 Rare earth ions, 388, 403
 Reciprocal lattice,
 of BCC, 74
 of FCC, 74
 of hexagonal, 75–76
 of SC, 73
 vectors, 65
 Reciprocal space, 63
 Rectangular lattice, 12
 Reduced zone scheme, 193
 Reflection,
 specular, 67
 symmetry, 8
 Reflectivity, 319
 Refractive index, 310
 Relaxation processes,
 direct, 420
 Orbach, 420
 Raman, 420
 spin-lattice, 420

- Relaxation time,
approximation, 169
spin-lattice, 420
spin-spin, 421
- Remanence, 441
- Reststrahlen band, reflection, 108–109
- Rhombic symmetry, 12
- Rochelle salt, phase transition, 332
- Rock salt (NaCl),
cohesive energy, 42–43
crystal structure, 21–22
- Rotating crystal method, diffraction, 84
- Rotation axis, 8–11
- Rotoinversion operation, 10
- Rotoreflection operation, 10
- Russel-Saunders coupling, 395
- Saturation (spontaneous)
magnetization, 430, 440
polarization, 329, 331, 335
- Saturation range (*see* Exhaustion range)
- Scanning probe microscopy (SPM), 543
- Scanning tunnelling microscopy (STM), 543–544
- Scattering,
defect-phonon, 139–140
elastic, 68
electron-phonon, 174
inelastic, 115–116
neutron-lattice, 115–116
phonon-phonon, 134–136
- Schönflies symbols, 17–19
- Schottky defect, 355
- Screening currents, 473
- Screw axis, 10
- Screw dislocation (*see* Dislocations)
- Second-order transition, 342
- Seebach potential, 177
- Seignette salt (*see* Rochelle salt)
- Semiconductor,
crystals, 247
degenerate, 262
extrinsic, 253
intrinsic, 241, 247
- Semimetals, 198
- Shear
modulus, 372
strain, 372
stress, 372
- Shubnikov–de Haas effect, 234
- Silicon and germanium,
constant energy surfaces, 244
crystal structure, 27, 253
energy bands, 243
intrinsic band gap, 248
- Silsbee effect, 504
- Silver halides,
excitons, 368–369
point defects, 358
- Simple cubic crystal, 19
reciprocal, 73–74
- Size effect, on thermal conductivity, 139–140
- Slip (*see* Dislocations)
- Sodium,
cohesive energy, 44, 207
crystal structure, 20–21
electron density, 154
missing diffraction lines, 78
- Sodium chloride (*see* Rock salt)
- Soft modes, 339
- Sommerfeld model of metals, 167
- Space
groups, 16–17
lattices, 13
- sp^3 hybridization, 37–38, 199
- Spin Hamiltonian, 438
- Spinel structure, 452
- Spin-lattice relaxation processes (*see* Relaxation processes)
- Spin-orbit coupling (*see* Russel-Saunders coupling)
- Spin-spin relaxation, 421
- Spin waves, 453
- Spiral growth, silicon carbide, 382
- Square lattice, 12
- SQUID, 510
- Stacking fault, 374
- Strain components, 48
- Strength of alloys (*see* Dislocations)
- Stress components, 48
- Structure factor, 77–80
- Substrate, 278
- Superconductors,
acoustic attenuation, 497
alloys, 468–469
BCS theory, 469, 490–496
coherence length, 493, 500
critical current density, 504
critical field, 478
critical temperature, 468–469, 508–514
diamagnetism, 477
elements, 468
gap, gapless, 477–480
Ginzburg–Landau theory, 498–501
ground state, 491
hard, 479
heat capacity, 484–485, 497
high T_c , 511–515
isotope effect, 488
- London–London equation (*see* London–London equation)
- magnetization, 478
- Meissner–Ochsenfeld effect, 471–473

- penetration depth, 476, 501
 thermodynamic properties, 479
 type I and type II, 478
 vortex state, 479
- Susceptibility, electric, 295
 diamagnetic, 391, 410
 paramagnetic, 394, 410
- Symmetry operations, 7–11
- T^3 -law, Debye, 129
 TA modes, 113
 Tetragonal symmetry, 13–14
 Thermal
 conductivity,
 via electrons, 150–153
 via phonons, 146–149
 excitation of magnons, 456–458
 expansion, 132–134
 ionization,
 acceptors, 257
 donors, 257
 resistance, 134–136
- Thermoelectric effects,
 in metals, 176–179
 in semiconductors, 278–282
- Thermoelectric power, 176–177
- Thermoluminescence, 560
- Thomson effect, 177
- Three-dimensional lattices, 13
- Tight-binding approximation, 199, 203
- TO modes, 113, 320
- Transition, phase
 first-order, 344
 second-order, 342
- Transition temperature,
 antiferromagnetic, 447
 ferrimagnetic, 451
 ferroelectric, 330
 ferromagnetic, 433
 superconducting, 468–469, 513–514
- Translational symmetry, 3, 7
- Transport equation, Boltzmann, 168
- Traps, luminescence, 561
- Triclinic symmetry, 13
- Trigonal symmetry, 13
- Triple-axis spectrometer, 115
- Tunnel diode, 273
- Tunnelling,
 single particle (normal), 273, 487
 two particle (Josephson), 504
- Two-dimensional lattices, 12
- Twinning (*see* Dislocations)
- Ultraviolet radiation,
 absorption in alkali halides, 369
 transmission through alkali metals, 318
- Umklapp processes, phonon-phonon scattering, 135–136
- Unit cell, 1, 3
- Upper critical field, type II superconductors, 479, 502
- Vacancies, 355
(see also Point defects)
- Valence band, 199
- van der Waals,
 bonds, 37
 crystals, 37
 interaction, 37, 43
- van Hove singularities, 126
- van Vleck paramagnetism, 404
- Vibrations,
 acoustic branch, 106
 balls and springs model, 98–100
 lattice, 98
 optical branch, 106
- von Laue, condition, 83
 diffraction pattern, 64
 interpretation of X-ray diffraction, 68–70
- Vortex state, superconductors (*see* Superconductors)
- Wall, Bloch, 444
- Wave equation, electron in a periodic potential, 194
- Wavevectors,
 electrons, 158
 phonons, 101, 116
- Weiss hypothesis, 431, 440
- Whiskers, 381
- Wiedemann–Franz law, 152
- Wigner–Seitz approximation, 204–206
- Wigner–Seitz cell, 6–7
- Work hardening (*see* Dislocations)
- X-ray diffraction
 Bragg law, 66–67
 experimental methods, 83–87
 von Laue interpretation, 68–70
- Young's modulus, 99
- Yttrium iron garnet, 453
- Zener diode, 274
- Zeolites, 534–535
- Zero point,
 energy, 114
 motion, 36, 114
- Zinc sulphide (Zincblende) structure, 28
- Zone, Brillouin, 65–66